A First Principles Study on The Effect of Hydrogen on The Electrical Properties of BCC Fe

Muhammad Ahmad

A Thesis

In the Department of

Mechanical, Industrial and Aerospace Engineering

Presented in Partial Fulfillment of the Requirements

For the Degree of

Master of Applied Science (Mechanical Engineering)

at Concordia University

Montréal, Québec, Canada

May 2024

© Muhammad Ahmad, 2024

CONCORDIA UNIVERSITY

School of Graduate Studies

This is to certify that the thesis

prepared by: Muhammad Ahmad

Entitled: A First Principles Study on The Effect of Hydrogen on The Electrical Properties of BCC Fe

and submitted in partial fulfillment of the requirements for the degree of

Master of Applied Science (Mechanical Engineering)

complies with the regulations of the university and meets the accepted standards with respect to originality and quality.

Date of defence: April 30, 2024.

Signed by the final Examining Committee:

Dr. Martin Pugh Chair

Dr. Martin Pugh Examiner

Dr. Deniz Meneksedag Erol Examiner

Dr. Mamoun Medraj Supervisor

Approved by *Dr. Martin Pugh*

Chair of Department

2024 *Dr. Mourad Debbabi*

Dean of Faculty

Abstract

A First Principles Study on The Effect of Hydrogen on The Electrical Properties of BCC Fe

Muhammad Ahmad

Iron (Fe) and iron-carbon (Fe-C) materials, used in various critical industrial applications, are susceptible to Hydrogen Embrittlement (HE) – a phenomenon leading to increased crack growth rate, reduced ductility, and potentially leading to catastrophic material failure. The intricate mechanisms underpinning HE demand comprehensive scrutiny. A pivotal aspect often overlooked is how hydrogen assimilation in these materials induces alterations in specific physical attributes, notably electrical resistivity. Addressing this gap, the study employs Density Functional Theory (DFT) and the MD-Landauer method to delve into the influence of hydrogen on the electrical characteristics of Fe and Fe-C systems. The study shows that the presence of interstitial hydrogen increases the resistivity of Fe and Fe-C systems. Hydrogen is seen to reduce the likelihood of electron transmission in the system by disrupting the electron density distribution. This introduces a noteworthy increase in resistivity with hydrogen incorporation. Moreover, the presence of defects, like vacancies and grain boundaries, is shown to increase the resistivity of these systems. Adding hydrogen along with these defects further increases the resistivity. Studying the effects of hydrogen on the physical properties of metals may pave the way for non-destructive detection of hydrogen presence in metals. Such understanding is crucial for enhancing quality control, ensuring material longevity, and preventing potential failures during manufacturing processes or in-service.

Acknowledgments

This thesis is dedicated to my parents, Asghar and Mamoona, who have always believed in me and supported me. And to my sisters - Farah, Amna, Asma, and Sidra - who have taught me how to be.

First and foremost, I would like to express my deepest gratitude to my supervisor, Professor Mamoun Medraj, for his invaluable guidance, encouragement, and support throughout the course of this research. His expertise and insights were instrumental in shaping this work, and his patience and dedication to my growth as a researcher were unwavering.

I am truly fortunate to have been a part of the Thermodynamics of Materials Research Group. Collaborating with such a talented team has been pivotal in my academic journey. A special mention goes to Dr. Rajwinder Singh, whose collaborative spirit, and expert insights have been invaluable to my research endeavors.

My sincere thanks to Safran Landing Systems for providing the financial support that made this research possible. Their commitment to fostering academic research is deeply appreciated.

I must also express my gratitude to my friends who have supported me in countless ways during this journey. Their belief in me, even during times of doubt, has been a source of strength and inspiration.

Table of Contents

List of Figures vii

List of Tables xii

Introduction 1

1.1 Hydrogen Embrittlement 2

1.2 Problem Statement 3

1.3 Thesis Layout 3

Literature Review 5

1.4 Hydrogen Embrittlement and First Principles in the Literature 5

1.5 Experimental Studies on Electrical Resistivity of Steel in the Presence of Hydrogen 8

1.6 Resistivity: Classical and Quantum Mechanical Approach 10

1.7 Density Functional Theory 14

1.8 Developments in Density Functional Theory for Electrical Resistivity Calculation 16

1.8.1 Non-Equilibrium Green's Function (NEGF) 17

1.8.2 MD-Landauer Method 17

1.8.3 Phonon-limited Mobility 17

1.8.4 Comparison between MD-Landauer, NEGF, and Phonon-Limited Mobility Method 17

1.9 Investigations on the Electronic Structure of Iron and Iron-Carbon Systems 20

1.10 Objectives 24

Methodology 26

Results and Discussion 42

1.11 Electronic Transmission and Hydrogen 42

1.11.1 General Trends in Electron Transmission in Fe with Hydrogen 42

1.11.2 Electronic Structure Alterations Caused by Hydrogen 44

1.11.3 Resistivity Analysis in the Fe and Fe-C systems With and Without Hydrogen 49

1.11.4 Resistivity Analysis by Crystallographic directions 57

1.12 The Impact of Vacancies and Vacancy-Hydrogen Complexes on Fe Resistivity 62

1.13 Effect of Grain Boundaries on Fe Resistivity in the Presence of Hydrogen 67

Conclusion, Original Contributions, and Future Work 72

References 76

Appendix 86

List of Figures

Figure 1 Hydrogen Embrittlement Process Schematic [80] 5

Figure 2 Eddy current signal vs embrittlement index [16] 8

Figure 3 Increase in impedance with hydrogen concentration [17] 9

Figure 4 Fermi surface of α-Fe (Created with QuantumATK analyzer) 12

Figure 5 Electrical resistivity of FeNiX systems (X=S,Si,O,C,H) [64] 23

Figure 6 Research methodology used in this study 26

Figure 7 Fe (left) and Fe-C (right) unit cells 27

Figure 8 Two probe configuration 27

Figure 9 Models with different MD-Region lengths for resistance measurement: (a) 20 Å, (b) 14 Å, (c) 3 Å 28

Figure 10 Variation in resistance with length of the MD region in pure Fe system for resistivity calculation – Direction [001] 30

Figure 11 Convergence of resistivity with increasing system size (MD-region length) – Direction [001] 31

Figure 12 Convergence of resistivity with increasing system size (MD-region length) - Direction [111] 32

Figure 13 Convergence of resistivity with increasing system size (MD-region length) - Direction [110] 32

Figure 14 Convergence of resistivity with increasing system size (MD-region length) - Grain boundary model 33

Figure 15 Convergence of resistivity with increasing number of k-points used in DFT calculation. 34

Figure 16 Fe-C model with 6 atomic % H 35
Figure 17 VH2 and VH3 configurations [58] 38
Figure 18 Fe-model with a vacancy 39
Figure 19 VH2 (left) and VH3 (right) complex 39
Figure 20 Fe model with the Σ5 [100]/[100] twist grain boundary located at the center. 40
Figure 21 Fe model with H located at the Σ5 [100]/[100] twist grain boundary 40
Figure 22 Fe model with the Σ5 [100]/[100] twist grain boundary along with dispersed interstitial H atoms 41
Figure 23 Fe model with A Σ5 [001]/[210] symmetric tilt grain boundary 41
Figure 24 Transmission spectrum of Fe-C system: (a) 0% H, (b) 6 atomic % H 43
Figure 26 Electron density of Fe system (with H) 44
Figure 25 Electron density of Fe system (without H) – Vertical dashed lines represent electrodes 44
Figure 27 Electron localization function of Fe system: (a) without H (b) with H 45
Figure 29 Electron localization surface map at the same plane from a model without H (a) and with H (b) 46
Figure 28 Electron localization heatmap at the same plane from a model without H (a) and with H (b) 46
Figure 30 Elementary charge distribution in Fe system (without H) 47
Figure 31 Elementary charge distribution in Fe system (with H – represented by big atoms for visual reference) 48
Figure 32 Resistance plots for Fe system at 0-6 atomic % H concentration 49
Figure 33 Resistance plots for Fe-C System at 0-6 atomic % H concentration 50

Figure 34 Variation in resistivity with hydrogen concentration in Fe system 50
Figure 35 Variation in resistivity with hydrogen concentration in Fe-C system 51
Figure 36 DOS in BCC Fe and Fe-H system [49] 52
Figure 37 DOS at and around fermi level in Fe and Fe-C-H model 52
Figure 38 DOS of an individual Fe atom in a pure Fe model 53
Figure 39 DOS of an individual Fe atom in proximity to a hydrogen atom in the Fe-H model ... 54
Figure 40 Different arrangements of C atoms in the Fe system to investigate a change in transmission due to the position of C atoms: (a) 1 random C atom – view in AB plane, (b) 2 consecutive C atoms- Isometric view in direction C, (c) 2 random C atoms – view in AB plane. 55
Figure 41 Transmission of Fe system with different configurations of C and H 56
Figure 42 Comparison of resistivity of Fe And Fe-C systems with varying hydrogen concentration 57
Figure 43 Resistance Plots for Fe-C system at 0-6 atomic % H concentration - Transmission Direction [111] 58
Figure 44 Variation in resistivity with H-concentration in Fe-C system - Direction [111] 58
Figure 45 Resistance plots for Fe-C system at 0-6 atomic% H concentration - Transmission Direction [110] 59
Figure 46 Variation in resistivity with H-concentration in Fe-C system - Direction [110] 59
Figure 47 Variation in resistivity with H-concentration in all three crystallographic directions . 61
Figure 48 BCC Unit Cell (a), labeled directions (represented by an arrow) (b), and perspective view of the crystal when observed from directions: (d) [001] (e) [111] (f) [110] 62

Figure 49 Charge distribution in Fe model with VH2 complex (H atoms are represented by bigger size for visual reference) 63
Figure 50 Electron density in the Fe model with VH2 complex 63
Figure 51 ELF in the Fe Model with VH2 complex 64
Figure 52 Electron localization heat map (a) and surface map (b) of the plane containing VH2 complex in Fe model 65
Figure 53 Electron localization heat map (a) and surface map (b) of the plane containing VH3 complex in Fe model 65
Figure 54 Electron localization heat map (a) and surface map (b) of the plane containing a vacancy in Fe model 66
Figure 55 Resistance calculation at different MD-region lengths for resistivity calculation of VH configurations 66
Figure 56 Resistivity of Fe-Model with different VH configurations 67
Figure 57 Electron localization heat map (a) and surface map (b) of the plane containing a grain boundary in Fe model 67
Figure 58 Electron localization heat map (a) and surface map (b) of the plane with H- atoms concentrated at the grain boundary in Fe model 68
Figure 60 ELF for model with grain boundary without H-atoms (a) and with H-atoms located at the grain boundary (b) 69
Figure 59 ELF for model with grain boundary and interstitial H 69
Figure 61 Resistance calculation at different lengths of MD-region for resistivity calculation in three cases of Σ5 [100]/[100] twist grain boundary 70
Figure 62 Resistivity for three grain boundary cases (Σ5 [100]/[100] twist grain boundary) 71

Figure 63 Resistivity for three grain boundary cases (Σ5 [001]/[210] symmetric tilt grain boundary) 71

List of Tables

Table 1 Resistivity of Fe and Fe-C system without hydrogen 34

Table 2 Transmission in Fe-C system 55

Table 3 Transmission in Fe-H system 56

Introduction

Fe and Fe-C systems are crucial materials in various applications, such as structural materials, automotive, and aerospace industries [1]. These materials exhibit exceptional mechanical, thermal, and electrical properties that make them suitable for numerous applications [2]. Hydrogen can be absorbed into these systems during any of the three main stages: production, processing, and service [3]. This absorbed hydrogen can cause HE, which is of significant concern in these materials, as it can promote crack growth and reduce ductility, posing a risk of catastrophic material failure [4], [5].

While much attention has been given to the impact of hydrogen on the mechanical properties of Fe and Fe-C systems, its effects on their physical attributes, especially electrical resistivity, remain relatively under-investigated. A better understanding of the effects of hydrogen on the physical properties of steel, particularly electrical resistivity, could contribute to the development of non-destructive testing techniques for detecting the presence of hydrogen. Despite the importance of resistivity in Fe and Fe-C systems, there is a notable lack of fundamental understanding of the change in electrical properties of these materials in the presence of hydrogen, using both experimental and computational techniques.

Thus, this thesis aims to address this gap in the literature by investigating the change in resistivity of Fe and Fe-C systems with varying hydrogen concentrations. The study will employ computational methods, specifically DFT [6], [7], to analyze the nuanced resistivity behaviors of Fe and Fe-C systems across various conditions. Initially, the focus is on the inherent resistivity of these systems without the interference of hydrogen. Subsequently, the research probes into how resistivity shifts at different hydrogen concentrations and emphasizes the electron transport across

three specific crystallographic orientations. The narrative then transitions to the resistivity alterations caused by vacancies in the Fe system, and how this dynamic process changes when these vacancies interact with hydrogen. Finally, the research dissects the role of grain boundaries on the resistivity of Fe, studying scenarios both with and without the presence of hydrogen. The findings of this research will provide valuable insights into the relationship between resistivity and hydrogen concentration and could inform the development of non-destructive testing methods for detecting hydrogen-induced changes in physical properties to avoid failure of materials due to HE while manufacturing or in service.

1.1 Hydrogen Embrittlement

HE is a complex phenomenon that affects the mechanical behavior of steel, causing premature failure and reduced ductility. This degradation process occurs when hydrogen atoms diffuse into the steel and interact with internal defects such as vacancies, dislocations, and grain boundaries [4], [5]. Several factors contribute to the susceptibility of steel to HE, including microstructure, grain boundary characteristics, and composition [4], [9], [10]. The presence of hydrogen within the material can lead to a significant decrease in its fracture toughness, promoting crack initiation and propagation [8], [9].

While there is an abundance of research exploring the effect of hydrogen on mechanical properties, its impact on physical properties, such as electrical resistivity, of Fe and Fe-C systems is comparatively less charted. Exploring these physical properties is essential since variations in electrical resistivity can indicate the presence of hydrogen, a key agent in the deterioration of material integrity. Understanding the changes in electrical resistivity due to hydrogen ingress could pave the way for the development of non-destructive testing methods to detect the possibility of HE. In this context, establishing a relationship between hydrogen concentration and the consequent

change in electrical resistivity becomes an essential aspect to investigate. The presence of hydrogen affects the electronic structure of Fe and Fe-C systems [10]. A better understanding of these alterations in electronic structure is crucial for developing advanced models that can predict the effects of hydrogen on the electrical properties of steel.

1.2 Problem Statement

This research aims to address the knowledge gap in several areas related to the effect of hydrogen on the electrical resistivity of Fe and Fe-C systems. Firstly, it investigates how resistivity changes with varying hydrogen concentration across three crystallographic directions. Additionally, the impacts of vacancies and their complexes with hydrogen on resistivity are explored. Lastly, the research evaluates the effect of grain boundaries on resistivity both in the presence and absence of hydrogen. Understanding these facets may offer insights into early-stage detection and prevention of hydrogen-related issues, thereby preventing premature damage in high strength metals used in essential applications such as landing gear of airplanes.

1.3 Thesis Layout

This thesis is structured to provide a comprehensive understanding of the resistivity changes in Fe and Fe-C systems, particularly in the presence of hydrogen. Following the introduction, the study delves into methodologies like DFT, various approaches to resistivity calculation, and a comparison between different methods. The core of the thesis (Section: Results and Discussion) consists of three distinct studies, each investigating how hydrogen influences resistivity in Fe and Fe-C systems. These studies encompass electron transport across various crystallographic directions, the impact of vacancies, and the role of grain boundaries on resistivity. The models and methods used in these studies are detailed in methodology section. A thorough discussion

synthesizes the findings, leading to a conclusion that encapsulates the essential insights and implications of the research.

Literature Review

This chapter explores literature relevant to the understanding of HE in Fe and Fe-C systems. The importance of the physical properties of material, particularly electrical resistivity in Fe and Fe-C systems, is underscored by their potential to indicate the presence of hydrogen. Delving into this aspect, this chapter begins with a discussion of HE and the experimental studies on electrical resistivity in the presence of hydrogen. Various approaches to understand resistivity, including classical and quantum mechanical, are then considered, with a focus on DFT and related computational techniques such as Non-Equilibrium Green's Function (NEGF) [11], MD-Landauer Method [12], and Phonon-limited Mobility [13]. A comparative analysis of these techniques and an overview of studies using DFT to investigate the effects of hydrogen on Fe culminate in the clear articulation of the thesis objectives.

1.4 Hydrogen Embrittlement and First Principles in the Literature

Hydrogen Embrittlement (HE) is a significant issue in materials science, particularly for structural materials such as high-strength steel [14]. It poses a threat to the safety and durability of steel components throughout the stages of production, processing, and service by making the material

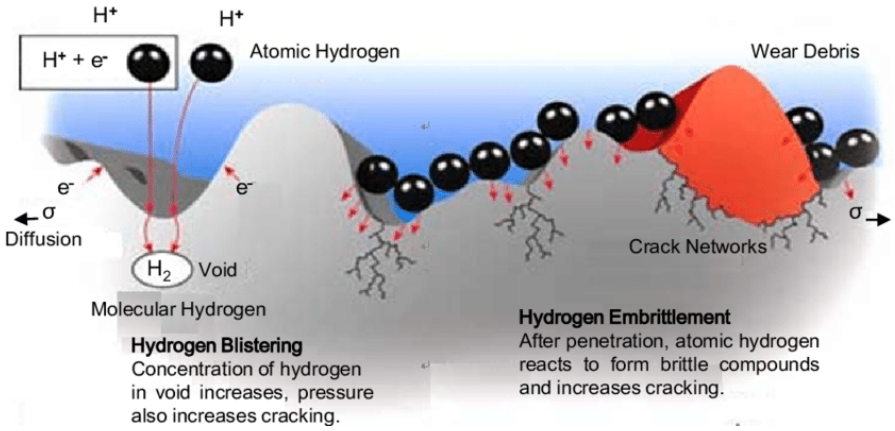

Figure 1 Hydrogen Embrittlement Process Schematic [80]

brittle and prone to catastrophic failure [3], [15]. A schematic of the HE process is shown in Figure 1.

HE has been thoroughly investigated in the literature using various experimental and simulation techniques [15], [16], [17]. The impact of hydrogen on the mechanical properties of metals has been explored using first principle calculations, focusing on four primary HE mechanisms: hydrogen-enhanced localized plasticity (HELP), hydrogen-enhanced de-cohesion (HEDE), adsorption-induced dislocation emission (AIDE), and hydrogen-enhanced strain-induced vacancies (HESIV) [15]. One such study utilized first-principles, quantum-mechanical (DFT) data to construct a kinetic Monte Carlo model to analyze dislocation velocity in α-Fe under different conditions [18]. This investigation delineated the interaction between hydrogen concentration and dislocation velocity, providing significant insights into how varying levels of hydrogen, stress, and temperature intersect to influence the HELP mechanism, offering a nuanced, physics-based representation of plasticity and paving the way for more advanced discrete dislocation dynamics simulations [18]. A pivotal study utilizing DFT conducted extensive first-principles calculations to scrutinize the fundamental interaction between hydrogen and dislocations and vacancies within steel [19]. Through these calculations, the study determined the precise binding energies, configurations, and thermodynamic stability of hydrogen near these microstructural defects. This in-depth analysis provided a profound understanding of how hydrogen influences the nucleation of dislocations and their subsequent motion, advancing the understanding of HEDE [19]. Another study utilizing both DFT and MD simulations has elucidated crucial insights into HE mechanisms in FCC metals, specifically concentrating on AIDE and HESIV mechanisms [20]. The research applied DFT to quantify the intricate interactions between hydrogen and lattice defects, thus providing atomic-level insights into the mechanisms of crack propagation in metals like Aluminum

and Nickel, and how they differ across various grain boundaries [20]. The research unveiled that AIDE is the predominant mechanism influencing crack propagation along the Twin Boundary (TB) in Aluminum and Nickel, with TB exhibiting superior resistance to HE compared to High Angle Grain Boundary (HAGB), where the HEDE mechanism is more prevalent. Moreover, the study underscored the importance of the HESIV mechanism, particularly in Aluminum, where it altered crack propagation paths by pinning gliding dislocations, fostering a preference for brittle-like fracture modes when the pinning force is substantial [20].

Stefano et al. [21] utilized first-principles calculations based on DFT to analyze how hydrogen atoms interact with grain boundaries in nickel. The investigation revealed distinct behaviors in hydrogen trapping and migration across different grain boundaries, shedding light on the effect of grain boundaries on hydrogen diffusion, which may have broader applicability to other metals and contribute to understanding HE mechanisms. Kumar et al. [22] carried out a first-principles study that investigated the effects of interstitial hydrogen atoms on the plastic deformation of various metals, including the impact on ideal shear strength. The findings revealed that hydrogen generally decreases the ideal shear strength across all metals examined. The study explores the effects of hydrogen on the electronic structure of metals with a detailed analysis of how hydrogen influences charge redistribution and electron localization within its vicinity. These alterations in electronic characteristics are then connected to observable changes in the mechanical properties of the system.

Drawing upon these investigations into the behavior of hydrogen within metals, it becomes apparent that there is still a significant gap in the research. While the impact of hydrogen on the electronic structure of metals and its subsequent influence on mechanical characteristics has garnered substantial attention, a comparable exploration of its effects on the physical properties,

especially electrical resistivity, of steel remains conspicuously absent. In light of the notable gaps in the understanding of the impact of hydrogen on the resistivity of steel, it is paramount to delve into experimental studies that investigate these crucial aspects.

1.5 Experimental Studies on Electrical Resistivity of Steel in the Presence of Hydrogen

The experimental studies in the literature report mixed findings regarding the change in electrical properties of steel in the presence of hydrogen. Zhou et al. [16] and Koenig et al. [17] observed changes in the electrical properties of steel in the presence of hydrogen. Zhou et al. [16] detailed a study of 2.25Cr-1Mo-0.25V ferritic steel, where a non-contact eddy current method revealed that the electrical properties of the material changed with hydrogen charging time. As shown in Figure 2, the eddy current signal intensifies as the embrittlement index (attributed to hydrogen-induced plasticity loss) rises. The exact mechanisms behind these changes are not clear and have been suggested for future investigation. Koenig et al. [17] elaborated on the development of a non-contact low-frequency impedance sensor designed for detecting hydrogen content in pipeline steel, specifically within a range of 0 to 30 ppm. As shown in Figure 3, this investigation highlights that resistivity, measured through impedance, changes with hydrogen concentration, enabling real-

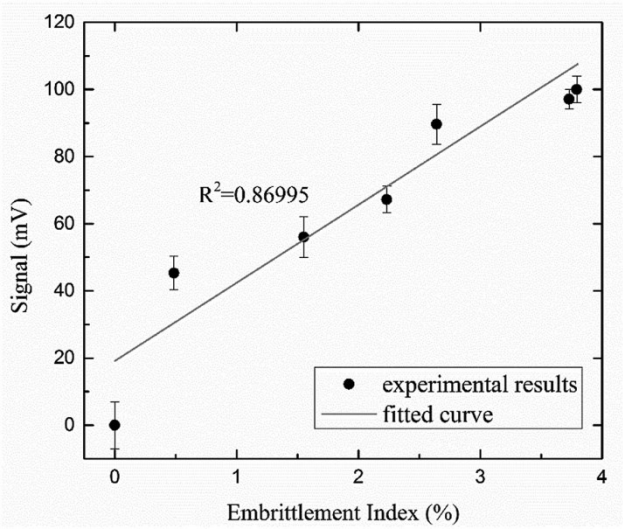

Figure 2 Eddy current signal vs embrittlement index [16]

time, nondestructive monitoring of hydrogen levels in steel weldments. Bellemare et al. [23] explored the effectiveness of electromagnetic non-destructive testing (NDT) for identifying HE in chromium-plated 4340 steel. The study focused on highly embrittled, notched bar samples, revealing a maximum hydrogen concentration of 1400 ppm atomic, predominantly in the Cr coating, out of which 430 atomic ppm was absorbed by the steel substrate. To evaluate hydrogen content and its correlation with material properties, the samples underwent successive baking at 190°C for 23 hours to desorb hydrogen and create varying hydrogen concentrations. This methodology aimed to isolate the effects of hydrogen concentration on the electric and magnetic properties of the materials. Despite these efforts, the electromagnetic NDT employed, specifically impedance measurements using eddy currents, failed to establish a significant correlation between the impedance of samples and their hydrogen concentration, even with variations in conductivity induced by high-temperature baking [23]. These variations were not indicative of hydrogen content but were more likely attributed to microstructural changes in the materials [23].

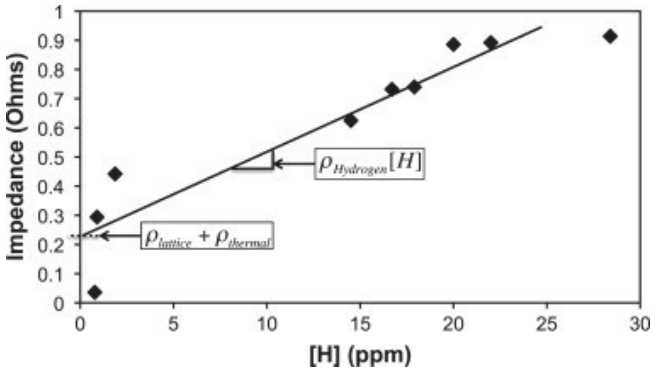

Figure 3 Increase in impedance with hydrogen concentration [17]

The experimental studies on the electrical resistivity of Fe or steel in the presence of hydrogen present a complex and often contradictory landscape, as delineated in the preceding discussion. These disparities in findings underline the challenges faced in understanding the precise interactions between hydrogen and the host material, and how these interactions influence the

electrical properties. While experimental methods provide valuable insights, they can sometimes be limited in unraveling the subatomic intricacies of hydrogen-metal interactions. As a result, turning to computational simulations may offer a more nuanced and detailed perspective. Simulations at the quantum mechanical level allow for a close examination of how hydrogen interacts with Fe at the atomic scale, thus offering the potential to resolve some of the contradictions observed in experimental data. Embracing this approach necessitates a comprehensive understanding of the physics underlying resistivity, including the fundamental concepts and mechanisms through which it arises in the material. In the following section, both classical and quantum mechanical approaches to understanding resistivity will be explored, laying the groundwork for a more in-depth computational analysis of the metal systems containing hydrogen. This transition to a computational paradigm represents a promising path toward a more coherent and unified understanding of the phenomenon at hand.

1.6 Resistivity: Classical and Quantum Mechanical Approach

Resistivity, a fundamental property of materials, is the measure of resistance to the flow of electric current in a material. In classical physics, resistivity can be understood using the Drude model [24], which describes the behavior of charge carriers (such as electrons) in a material. According to the Drude model describing electrical conductivity and resistivity, electrons experience a sudden change in their velocity after experiencing a collision. The probability of this collision is $1/\tau$, where τ is the relaxation time or the average time between two consecutive collisions or scattering events. The Drude model can be applied to metals, and the resistance is dependent on the dimensions of the specimen and is given as [25]:

$$R = \rho\, L/A \qquad 1$$

Where ρ is the resistivity, L is the length of the specimen, and A is its cross-sectional area. The electrical conductivity, σ, which is the reciprocal of resistivity, is given by the equation as follows:

$$\sigma = \frac{1}{\rho} = \frac{ne^2\tau}{m} \quad 2$$

where *n* is the electron density, *e* is the electron charge, and *m* is the electron mass. According to this formula, electrical conductivity is directly proportional and resistivity is inversely proportional, to the collision or relaxation time, respectively. If it takes a long time for electrons to experience a collision, there would be less scattering and hence more conductivity, and less resistivity [25].

However, this classical approach has limitations when considering certain materials and conditions, especially at the nanoscale or when quantum mechanical effects become dominant. To address these limitations, it is essential to apply quantum mechanics and understand key concepts such as the k-space (momentum space), Fermi sphere, Fermi surface, and Fermi energy [26]. The k-space is a concept from quantum mechanics that represents the momentum states of electrons in a material [26]. It is an abstract three-dimensional space where each point corresponds to a specific momentum state of an electron. This is because electrons in a crystal have both particle-like and wave-like properties, and their momentum behaves like a wave in k-space. So, in order to fully understand the behavior of electrons in a crystal, it is imperative to look at their momentum properties in addition to their position properties. Understanding the distribution of electron states in k-space helps to visualize and comprehend the behavior of electrons, including their energy and momentum relationships, in a solid [26]. The Fermi surface is an abstract boundary in k-space that defines the allowable energy states for electrons in a solid. This surface is crucial in determining the electrical and thermal properties of a material, with the band theory suggesting how electrons are distributed within a material [26], [27]. The band theory divides electrons in a material into

two groups: those in valence bands, which are tightly bound, and those in conduction bands, which possess higher energy and are free to move. The energy of electrons within each band correlates to their momentum. At absolute zero temperature, electrons cannot occupy energy levels beyond a certain limit, known as the Fermi energy [27], [28]. This can be visualized in k-space (the three-dimensional momentum space comprising of multiple k-points used vastly in DFT calculations since electrons possess a wave-like character and it is easier to do calculations in momentum space as compared to a position space), where the energy of electrons is plotted against the momentum in the x, y, and z directions. This results in a volume known as the Fermi Sphere, the surface of which defines the Fermi energy [29]. A simple free-electron model (which assumes electrons move freely through a metal without interacting with the lattice) would indeed predict a spherical Fermi surface. However, real metals are not free-electron gases. Electrons in real metals interact with the periodic potential of the crystalline lattice. These interactions lead to the formation of electronic bands, and the topology of these bands in momentum space defines the shape of the Fermi surface. To further illustrate this concept, Figure 4 showcases the Fermi surface of Fe, giving a visual representation of the momentum states occupied by electrons up to the Fermi energy. Notably, the

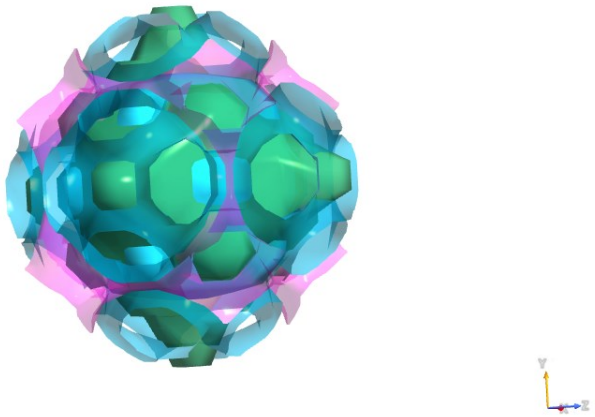

Figure 4 Fermi surface of α-Fe (Created with QuantumATK analyzer)

Fermi surface of metals like Fe often appears bumpy and irregular. This irregularity arises due to the complex interplay of electron wavefunctions with the periodic potential of the lattice. In essence, the 'bumps' or deviations from a smooth sphere reflect the band structure of the crystal and the variations in electron energy at different momentum states. As the electrons interact with the periodic potential of the crystal lattice, they form energy bands. Where these bands cross the Fermi energy, complexities are observed in the Fermi surface shape. The quantum mechanical perspective posits that electrons near the Fermi surface are the ones responsible for carrying current and determining the transport properties of electrons within a material. This is because, at temperatures above absolute zero, these electrons are elevated above the Fermi energy and become free to move [30]. This perspective becomes particularly relevant when considering that, between collisions, an electron can travel an average distance much greater than the interatomic distance [31]. In this context, the Landauer formula [32], a quantum mechanical expression for conductance, is insightful. The formula states:

$$G(L,T) = \frac{2e^2}{h} \int T(E)[f(E) - f(E + eV)]\, dE \qquad 3$$

where G is the conductance, $T(E)$ is the transmission probability, which is a measure of the likelihood that a particle (such as an electron) can pass through a potential barrier, as a function of energy, $f(E)$ and $f(E + eV)$ are Fermi-Dirac distribution functions, which describe the probability that a given energy state is occupied by a particle (electron) at a certain temperature in a system of many particles. V is the applied voltage, and the integral is over all energies [32]. This formula suggests that the conductance depends not only on the transmission probability of the electrons but also on the distribution of the electrons within the material. For a material with a perfect lattice, the transmission would theoretically be 100%, leading to infinite conductivity. However, this is not observed in reality due to lattice imperfections and thermal vibrations, which scatter the

electrons and reduce the transmission [32]. Yet, while pure, undisturbed crystal structures offer theoretical insights, real-world materials are far from perfect. Imperfections in the lattice and the influence of thermal vibrations often modify electron behavior. This complexity necessitates advanced computational approaches to obtain a closer representation of reality, one of which is DFT.

1.7 Density Functional Theory

Density Functional Theory (DFT) is a computational technique widely used in solid-state physics, materials science, and condensed matter physics. It provides a theoretical framework for calculating electronic properties and describing the quantum behavior of materials by solving the Schrödinger equation [33]. In DFT, the electron density, a function accounting for the positions of all electrons in the system, is the cornerstone; it governs the total energy of the system and thereby allows identification of the ground state. Thus, the electron density serves as the foundation for defining electronic structure and additional material properties [34].

This research capitalizes on the powerful capacity of DFT to investigate the impact of hydrogen concentration on the electrical resistivity of Fe and Fe-C systems. By calculating the electronic structure of these systems, DFT can yield valuable insights into the mechanisms that determine their electrical properties [7], [10].

However, it is essential to understand the strengths and limitations of DFT to accurately interpret its results. One of the primary challenges in DFT is the need to approximate the exchange-correlation operator, which accounts for the interactions between electrons due to their Coulomb repulsion [7], [35]. The accuracy of DFT calculations largely depends on the choice of density functional used for this approximation.

The Schrödinger equation is a building block of DFT that explains the behavior of particles, such as electrons, in the system under study. It is given as [34]:

$$\widehat{H}\Psi = E\Psi \qquad 4$$

Where Ψ is the wave function of the system which encodes all the information about the system state, including the probabilities of finding particles at different positions and with different momenta. $\widehat{H}$ is the Hamiltonian operator that performs mathematical operations to calculate how the energy is distributed or behaves according to the wave function of the system [34], [36]. E is the set of specific energy values that result from this calculation for a given state. The total energy of particles in the crystal lattice depends on the kinetic energy of electrons, the external potential generated by nuclei which vary in space and affect the motion of electrons, other external potentials, and interactions between electrons which also involve the quantum mechanical interactions, which is not known exactly and needs to be approximated. All of these are represented by the Hamiltonian operator [33], [37]. Therefore, in DFT, the Hamiltonian operator is divided into two components: the one-body operator, and the exchange-correlational operator. The kinetic energy of the electrons, the external potential generated by the nuclei, and any other external potentials in the system are included in the one-body operator. The exchange-correlation operator considers the interactions between the electrons due to their Coulomb repulsion [37]. The exchange-correlation operator is a key component of DFT because it represents the effects of electron-electron interactions on the electronic structure of the material. It is typically approximated by mathematical functions of the electron density.

One of the most commonly used density functionals in DFT is the Local Density Approximation (LDA), which assumes that the exchange-correlation energy depends only on the local electron

density at each point in the material. Another commonly used density functional is the Generalized Gradient Approximation (GGA), which incorporates information about the gradient of the electron density into the exchange-correlation functional [33], [37]. Both approximations have their strengths and weaknesses, and selecting the appropriate functional is crucial for obtaining accurate results. In the context of DFT implementations, the Density Functional Tight Binding (DFTB) method is an advantageous extension that is used in this study [38]. This method is a simplification of DFT, transforming the intricate processes involved in DFT into a more manageable format, particularly for large atom-based systems [38]. The simplification does not come at the expense of precision. DFTB represents the DFT Hamiltonian in a more straightforward, atomic-orbital-like basis set. This less complex basis set is efficient yet effective for describing the electronic properties of materials [39]. DFTB achieves this by conducting a second-order expansion around the Fermi energy, utilizing parameters usually derived from full-scale DFT calculations, which makes the matrix operations at each lattice site in the model easier to handle. This makes the numerical procedure to calculate transmission coefficient in equation 3 straight-forward [32]. This method bridges the gap between computational demand and accuracy, making DFTB ideal for large systems [39]. In summary, DFTB maintains the valuable insights into electronic properties offered by DFT, while providing computational efficiency.

1.8 Developments in Density Functional Theory for Electrical Resistivity Calculation

DFT has been widely used in the study of electronic transport properties in materials, including the calculation of electrical resistivity. An important application of DFT in this context is the study of defects and impurities in metals, which can significantly affect the electronic structure and hence the electrical conductivity of the material. To calculate electrical resistivity using DFT, the electronic transport properties of the material must be simulated. Various computational

techniques have been established for this purpose, including the Non-Equilibrium Green's Function (NEGF) method, the Molecular Dynamics (MD) - Landauer method, and the Phonon-limited Mobility method.

1.8.1 Non-Equilibrium Green's Function (NEGF)

NEGF, used in conjunction with DFT calculations, estimates the electronic transport properties of materials [40]. It is based on frequency-domain simulations and the wave function of the electrons in the system. By allowing for the application of a voltage, NEGF can be used to examine the impacts of electron scattering and other parameters integral to electronic transport.

1.8.2 MD-Landauer Method

The MD-Landauer method amalgamates molecular dynamics (MD), DFT, and Landauer transport theory to calculate the electrical resistivity/conductivity of a material [12]. As a time-domain simulation technique, it uses a scattering matrix to illustrate the probability of an electron scattering from one region of the material to another. This method is particularly beneficial when studying the electronic properties of nanoscale materials [12], [41].

1.8.3 Phonon-limited Mobility

The Phonon-limited Mobility method, using the Boltzmann Transport Equation, discerns the electrical resistivity of materials by simulating the electron scattering resulting from the phonon vibrations in the crystal lattice. Between scattering events, the mean free path and the scattering rate of electrons due to electron-phonon interactions are calculated [42].

1.8.4 Comparison between MD-Landauer, NEGF, and Phonon-Limited Mobility Method

The MD-Landauer, Phonon-limited Mobility, and NEGF methods differ significantly in how they model electronic transport. Notably, they have been extensively studied for their precision and

efficiency in predicting electronic transport properties for different cases [12]. To explore the effect of defects and impurities on electronic transport, the MD-Landauer method is appropriate as it can capture scattering due to defects directly [43]. Conversely, the Phonon-limited Mobility method primarily studies the impacts of lattice vibrations (phonons) on electronic transport, lacking a direct means to incorporate the effects of impurities and defects. Markussen et al. [12] calculated the resistivities of silicon and gold with the Phonon-limited Mobility and MD-Landauer methods, showing that both methods produce results in close agreement yet reiterating that incorporating additional scattering mechanisms, such as defect scattering or grain-boundary scattering, is more efficient in the MD-Landauer method. Since this study aims to analyze the effects of H and defects on the electrical resistivity of Fe-based systems, MD-Landauer method would be a more appropriate choice.

In simulating electronic transport through a two-probe virtual device, the MD-Landauer method utilizes the Landauer formula to calculate the electronic conductance based on the electron transmission probability [32]. In contrast, the Phonon-limited Mobility method relies on the Boltzmann transport equation (BTE), which requires additional assumptions and approximations to account for the scattering of electrons by phonons, potentially introducing uncertainties [12], [42]. The MD-Landauer method provides a more precise and detailed description of the electronic structure and transport properties of a system as it is based on first-principles DFT calculations of the electronic structure [12]. The Phonon-limited Mobility method, however, uses empirical parameters and approximations to describe electron-phonon interaction/coupling (EPC) [42]. While more computationally intensive, the MD-Landauer method offers a more accurate and realistic representation of electronic transport than the Phonon-limited Mobility method [12]. As reported by Markussen et al. [12], in electron-phonon coupling (EPC) studies, the harmonic

approximation is often employed in both BTE and NEGF methodologies. This simplification treats the phonons—vibrational modes of the crystal lattice—as non-interacting entities, akin to masses on idealized springs. Such an approximation is computationally advantageous but can overlook the anharmonic effects where phonons interact with each other, especially prominent at elevated temperatures. Conversely, MD in the Landauer framework inherently captures these anharmonic interactions. Incorporating realistic interactions such as this can help to better predict the electron transport. Unlike BTE and NEGF, MD does not rely on simplified assumptions and provides a more nuanced representation of phonon behaviors, making it particularly adept at modeling high-temperature phenomena without added computational overhead.

The NEGF method also enables the study of electronic transport through nanostructures. However, compared to the simpler and more straightforward MD-Landauer method, NEGF requires more advanced theoretical and computational techniques [12], [40]. The MD-Landauer method is suitable for large systems, such as bulk materials, especially with impurities. Studying these systems with NEGF may be computationally challenging due to their complexity [12], [40]. The MD-Landauer method also allows more flexible modeling of the contacts between the system and the electrodes. In contrast, the NEGF method typically assumes idealized models of the electrodes, which may not accurately represent the contacts in the system [44], [45]. The NEGF method generally assumes that the system is in thermal equilibrium. For example, Zahid et al. [46] and Ke et al. [47] calculated the resistivity of Cu thin films with surface roughness and coatings using the NEGF method, and all the calculations were performed at zero temperature and then compared to the experimentally available room temperature results. Whereas, the MD-Landauer method more realistically incorporates thermal effects such as phonon scattering. This can be significant when studying the temperature dependence of electronic transport properties in materials containing

interstitial elements [12]. This makes MD-Landauer method a favorable technique to study the effects of interstitial H on the electrical resistivity of Fe-based systems.

1.9 Investigations on the Electronic Structure of Iron and Iron-Carbon Systems

Given the intricate interplay between the atomic and electronic structures and how they dictate the diverse physical properties of materials, such as electrical resistivity, examining the interaction of hydrogen with Fe and Fe-C systems is crucial. These interactions have been the focus of substantial research efforts in recent years due to their paramount importance in numerous engineering applications. A profound comprehension of how the electronic structures of Fe and Fe-C systems are altered in the presence of hydrogen is fundamental. Such understanding not only elucidates their behaviors under diverse conditions but also facilitates more precise predictions of their properties.

Gavriljuk et al. [48] compiled a series of experimental and theoretical first-principle studies examining the interaction between hydrogen and engineering metals. Their compilation covers the effects of hydrogen on the electronic structure of metals, dislocations, defects in the metallic structure, and phase transformations. The studies include research that utilized MD and DFT to study HE mechanisms. Recent studies have employed DFT for an in-depth investigation of the physical properties of materials such as metals, notably to explore changes in the electronic structure in the presence of hydrogen. These investigations have specifically observed alterations in the Density of States (DOS) [14], [49], [50], [51], [52], [53], [54]. An increase in DOS, due to the presence of hydrogen and nitrogen, leads to a rise in the number of free electrons at Fermi levels, enhancing the metallic nature of bonds. On the other hand, the inclusion of carbon reduces DOS, contributing to the covalent component of the interaction [51], [52], [55]. These variations in electronic structures also influence the mobility of grain boundaries and the thermodynamic

stability of Fe-based solid solutions, which can affect material properties [10], [53], [54], [55], [56]. The work of Gavriljuk et al. [50] sheds light on the substantial alterations in the mobility of dislocations and the earlier onset of recrystallization in hydrogenated, cold-worked Fe-based alloys. This is related to the changes in the electronic structure due to the infusion of hydrogen, nitrogen, or carbon, which in turn affects the density of electron states and the mobility and properties of dislocations within the metal lattice. Such changes hint at a possible correlation between the alteration in electronic structures and mechanical properties in metallic materials. In an earlier study, Gavriljuk et al. [56] conducted an experimental and theoretical investigation into the effects of C, N, and H on the electrical, mechanical, and material characteristics of Fe-based solid solutions. Research presented in [55] and [56] has drawn parallels between the effects of different interstitial atoms such as hydrogen. The investigation revealed potential similarities in embrittlement effects under impact loading, suggesting a shared influence of electronic structure alterations. Additionally, the results reported in [51], [53], [54], [57] highlight how interstitial atoms affect dislocation slip, mobility of dislocations, and grain boundaries diffusion. These changes in mechanical properties are intimately linked to variations in electronic structures induced by the presence of hydrogen, suggesting that a link between hydrogen content and the physical properties is possible through the impact of hydrogen on the electronic structure. While the majority of the studies have emphasized the changes in mechanical properties due to hydrogen, the effect on physical and, especially, electrical properties needs more attention. The effect of changes in the electronic structure and free electrons on electrical resistivity of Fe in the presence of impurities has not been studied in literature. The current research presented in this thesis covers this aspect.

In addition to changes in the electronic structure, DFT has been utilized to examine the alteration in the lattice structure of metals in the presence of hydrogen [9], [58], [59], and the diffusion mechanism of hydrogen within them [3]. Further, DFT has been instrumental in developing interatomic potentials for simulating Fe-H systems [60], which are involved in simulating Fe-H systems with MD-Landauer method chosen for this study. Adding to these insights, a study by Tateyama et al. [61] showcased through ab initio supercell calculations that hydrogen stimulates and stabilizes the vacancy-hydrogen complexes where it is associated with vacancies in α-Fe, promoting the creation of distinctive vacancy clusters like line-shaped and tabular vacancy clusters. This finding enriches the understanding of the role of hydrogen in modifying vacancy interactions and ties the behavior of hydrogen to changes in electronic structures while providing fresh insights into HE in Fe-rich materials. Additional research by Mirzaev et al. [58] has revealed specific configurations and distances between hydrogen atoms within vacancies using ab initio modeling. This investigation has shown how electronic structure changes underpin alterations in atomic configuration due to hydrogen interactions. Similarly, the works of Ohsawa et al. [59] and Besenbacher et al. [62] have expanded on the configurations and binding energies of hydrogen atoms within a monovacancy, again emphasizing the fundamental role played by changes in electronic structures. These vacancy clusters and their effects on the electrical resistivity of Fe are a part of this study. Similarly, Bishara et al. [63] provide a comprehensive study on how the atomic structure of grain boundaries in copper influences electrical resistivity. The findings reveal that resistivity significantly increases with the presence of grain boundary, but the study does not mention the effect of impurities. On the other hand, this thesis will analyze the changes in resistivity in the presence of grain boundaries with and without H.

A notable study by Zidane et al. [64] explored the resistivity of Fe-Ni alloys with various light elements, including hydrogen, under core conditions of Earth. As shown in Figure 5, the results indicated increased electrical resistivity with hydrogen concentration, but such observations are primarily relevant to extreme high-pressure environments and 0K temperature. The blue, purple, green and grey open symbols for S, O, C and Si respectively for FeNiX alloy in Figure 5(a) are experimental values from Gomi et al. [65] at 4971 K. The open orange squares represent the values for liquid $Fe_{0.90-x}Si_{0.10}O_x$ calculated by Pozzo et al. [66] at approximately 5600 K. The open pink symbol at zero concentration of X in FeNiX is that measured by Gomi et al. [65] at 4971 K. Given the extreme nature of these conditions, applying the findings directly to scenarios at atmospheric pressure and temperature is fraught with complexities. Furthermore, this study, while insightful, did not account for the phononic contribution to electrical resistivity, indicating potential deviations in actual resistivity values.

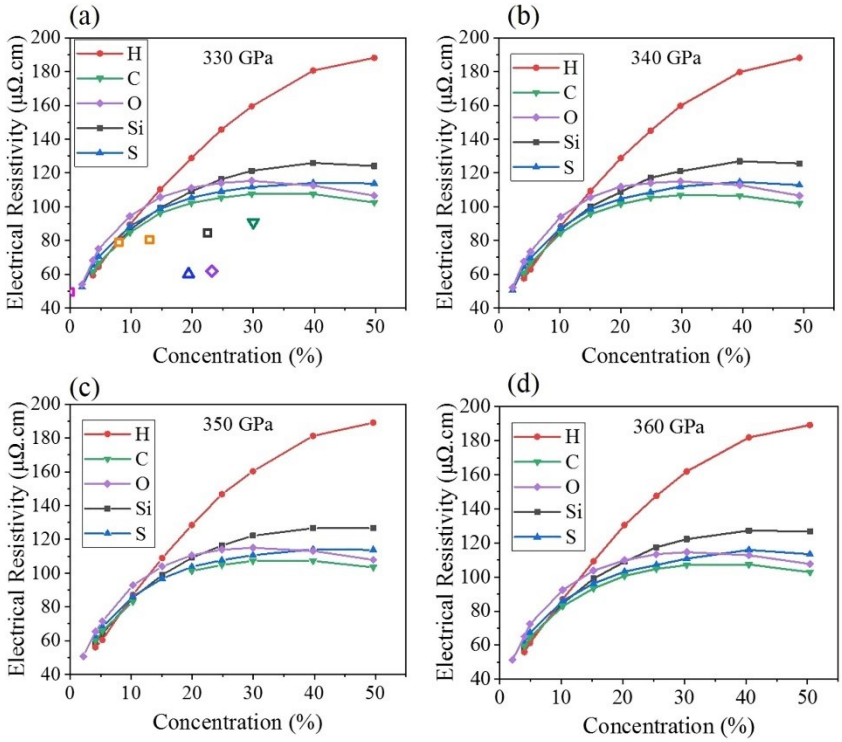

Figure 5 Electrical resistivity of FeNiX systems (X=S,Si,O,C,H) [64].

The various studies mentioned above have extensively explored how the presence of hydrogen affects the electronic structure of Fe-based solid solutions, and how changes in this structure can relate to the mechanical properties of the material. Despite a wealth of research on this topic, a notable gap still exists, specifically around the impact of hydrogen on the physical properties of these solutions, when studied using DFT calculations. There is a crucial need to better understand how changes in electronic structure can reflect alterations in the physical properties of Fe-based solid solutions. This study intends to address this gap by investigating the influence of hydrogen on the electrical resistivity of Fe and Fe-C systems, aiming to offer a clearer understanding of how hydrogen influences these systems. This could lead to the development of new nondestructive techniques for detecting the presence of hydrogen in such systems by monitoring changes in their physical properties.

1.10 Objectives

The primary aim of this research is to investigate the intricate effects of interstitial hydrogen, vacancies (with and without hydrogen), and grain boundaries (with and without hydrogen) on the resistivity of Fe and Fe-C systems. This detailed exploration was steered by the following defined objectives:

- Employ the MD-Landauer Method and DFT simulations to examine the modifications in the electronic structure and electrical resistivity when Fe and Fe-C systems are infused with hydrogen.
- Investigate the influence of vacancies within Fe crystal lattice on resistivity and how the resistivity alters when hydrogen is incorporated into these vacancies.

- Evaluate the impact of grain boundaries on the electronic attributes of Fe, and how the resistivity changes when hydrogen is present at these grain boundaries and interstitially distributed throughout the system.
- Analyze variations in resistivity with electron transport across different crystallographic directions in Fe, particularly [001], [111], and $[1\bar{1}0]$ directions, with varying hydrogen concentrations.
- Discuss the effects of hydrogen and carbon atoms on the resistivity of Fe through the lens of Density of States (DOS), as well as from their contribution to the scattering of electrons (electron transmission).

By accomplishing these objectives, this research aims to offer valuable insights into the complex relationships between interstitial impurities (such as hydrogen), structural defects, and resistivity in Fe and Fe-C systems. The outcomes of this investigation might open avenues for developing non-destructive techniques for assessing physical changes in Fe and its alloys due to hydrogen incorporation.

Methodology

In the realm of materials science, understanding the electrical and thermal attributes of materials hinges on an in-depth analysis of their electronic structure and their interactions with phonons. The intricate phenomenon of electron scattering requires sophisticated modeling to derive accurate insights into these properties. An overview of the research methodology adopted in this study is presented in Figure 6. The ensuing methodology elucidates the detailed approach adopted in this study, employing DFT and a two-probe computational device configuration [12]. This approach not only aligns with previous research examining the electrical resistivity of materials such as Copper and semiconductors such as Silicon but also incorporates advanced computational techniques to achieve precision in results [12].

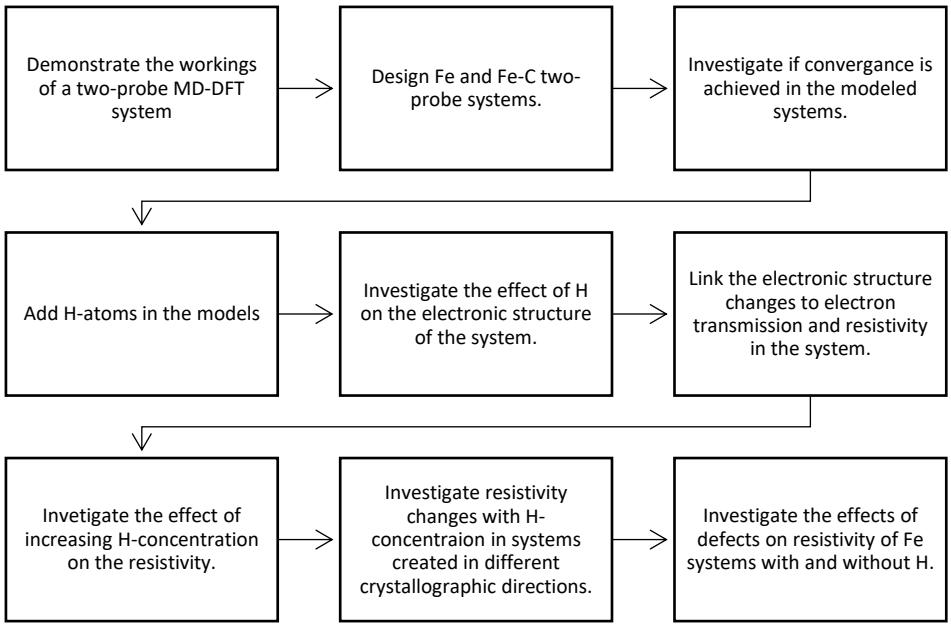

Figure 6 Research methodology used in this study

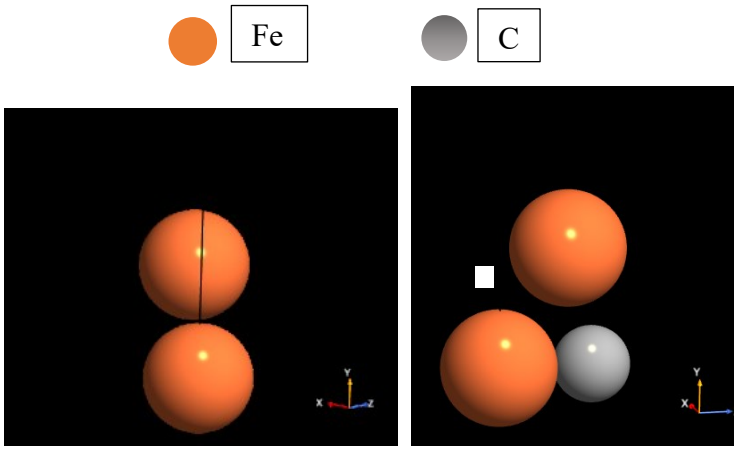

Figure 7 Fe (left) and Fe-C (right) unit cells

The two-probe device configuration, created using a BCC Fe unit cell as shown in Figure 7, has three distinct regions: a central region and two electrodes, as shown in Figure 8. The left and right electrodes are periodic and are attached to the central region which is non-periodic and finite along the transport direction of electrons. There are electrode extensions on either side of the central region which are exact replicas of both electrodes and they are not allowed to undergo change during any part of the simulation. These electrode extensions are crucial for maintaining numerical stability as they ensure a seamless and coherent transition between the central region and the electrodes, preventing any abrupt changes or discontinuities that could lead to inaccuracies in the

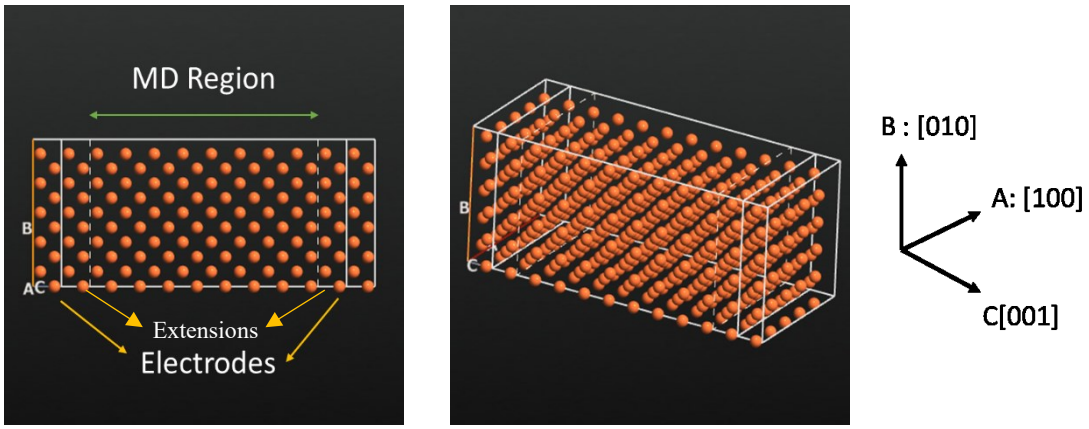

Figure 8 Two probe configuration

calculations. The central region is what defines the properties and functionality of the system since scattering occurs in this region. It has the MD region where atoms are allowed to vibrate. The charge carriers/electrons traveling from the left to the right electrode are scattered in the MD region because of physical and/or chemical changes such as the presence of grain boundaries, impurities, and other defects. An electron flux from the left electrode is transmitted with a certain probability to the right electrode after passing through the MD region. Calculations in the MD region are performed while atoms are allowed to move for some nanoseconds after being given random initial velocities based on Maxwell-Boltzmann distribution [67]. Only the atoms in the MD region are allowed to move. All the MD-Landauer calculations in this study are executed at a temperature of 300K, since this study is focused on resistivity calculation at the room temperature. The Langevin thermostat [66] is deployed with varying time steps: 1 fs for systems without hydrogen atoms and 0.05 fs for those with hydrogen atoms. This variation is essential as hydrogen, due to its lighter mass, can escape the system when larger time steps are utilized. A thermostat is essential for the modulation of system temperature, ensuring that the average temperature remains within the specified range.

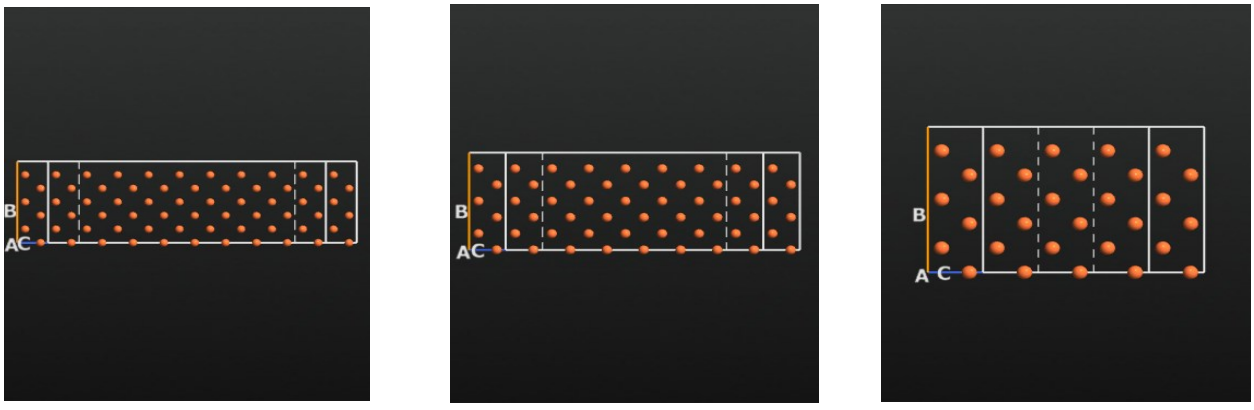

(a) (b) (c)

Figure 9 Models with different MD-Region lengths for resistance measurement: (a) 20 Å, (b) 14 Å, (c) 3 Å

All the two-probe models/systems in this study are generated using QuantumATK builder tool [41]. Following is the step by step process of calculating the resistivity of a particular model:

1. The length of the MD-region is varied, as shown in Figure 9, up to an optimal length decided based on convergence test described later in this section. Resistance values are noted against each length. Resistance is calculated as a reciprocal of conductance. Conductance is calculated with the Landauer formula [10], as per equation (5).

$$G(L,T) = \frac{2e^2}{h} \int < \mathcal{T}_L[E;\, x(T), L)] > [-\frac{\partial n_F(E,\epsilon_F,T)}{\partial E}]\, dE \qquad 5$$

Where $\mathcal{T}_L$ is the transmission coefficient at different lengths of the MD-region denoted by L, E is energy in eV, n_F(E, ϵF, T) is the Fermi-Dirac distribution function, and ϵ_F represents the Fermi level. <…> in equation (5) denotes the average of several calculations. In this study, to ascertain the reliability of the findings, 10 MD calculations are performed, at a fixed temperature (T) and a set of different lengths (L), and the average transmission coefficient is calculated at each length. The transmission coefficient is calculated using equation (6) [12].

$$\mathcal{T}\,[\mathrm{E};\, \mathrm{x(T)},\, \mathrm{L})] = \mathrm{Tr}\,\{\mathrm{G^r}\,[\mathrm{E};\, \mathrm{x(T)},\, \mathrm{L}]\Gamma_{\mathrm{L}}(\mathrm{E})\mathrm{G^a}\,[\mathrm{E};\, \mathrm{x(T)},\, \mathrm{L}]\Gamma_{\mathrm{R}}(\mathrm{E})\} \qquad 6$$

Where Tr is the trace operation which integrates over all the contributions from different energy states of the system, providing a total measure of transmission through the system. G^r (E; x(T), L) and G^a (E; x(T), L) are retarded and advanced Green's function respectively, Γ_L(E) and Γ_R(E) represent coupling with electrodes, L is the length of the MD region, x(T) represents displacement coordinates of the atoms [67]. The Green's function and transmission coefficient are a function of energy E, displacement of atoms x, and length of the MD region L. Since atoms are given random velocities and displacement according to Maxwell-Boltzmann distribution, many MD calculations are performed, and the results are averaged out to eliminate the randomness in the data.

2. Resistance values are plotted against the corresponding lengths they are calculated at.
3. A linear curve fitting is performed for data in step 2, and the slope of the curve is calculated.
4. The resistivity is calculated from the slope resulting from the linear fit as shown in equation 7 and 8.

$$\frac{1}{\mathrm{G(L,T)}} = \mathrm{R(L,T)} \equiv R_c + \rho_{1D}(T)L \quad (7)$$

$$\rho_{Bulk} = \rho_{1D}(T).A \quad (8)$$

Where A is the cross-section area. All these steps are accomplished using QuantumATK software package (version 2022.03, platform: Windows) using the electron transport calculation functionality involving the Tight Binding Engine and Non-equilibrium Green's Function Package. The results are postprocessed using Python scripts. By following the above four-step process, the resistivity of the system is calculated. Figure 10 shows the resistance calculated at different MD-region lengths of pure Fe system. The resistivity of Fe-C system, and any other resistivity calculation in this study, is calculated by following the same procedure. An in-depth overview of these steps and the importance of including resistance at L=0 is included in the appendix. Since, the resistivity is calculated by plotting resistance with an increasing MD-region length up to a certain point, X, an optimal range (0 to X Å) for MD-region length of the model has to be determined.

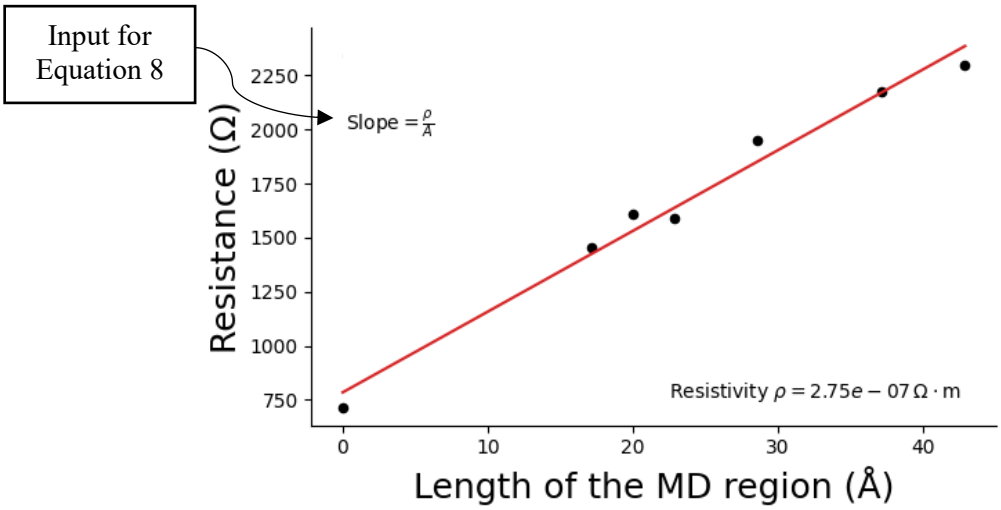

Figure 10 Variation in resistance with length of the MD region in pure Fe system for resistivity calculation – Direction [001]

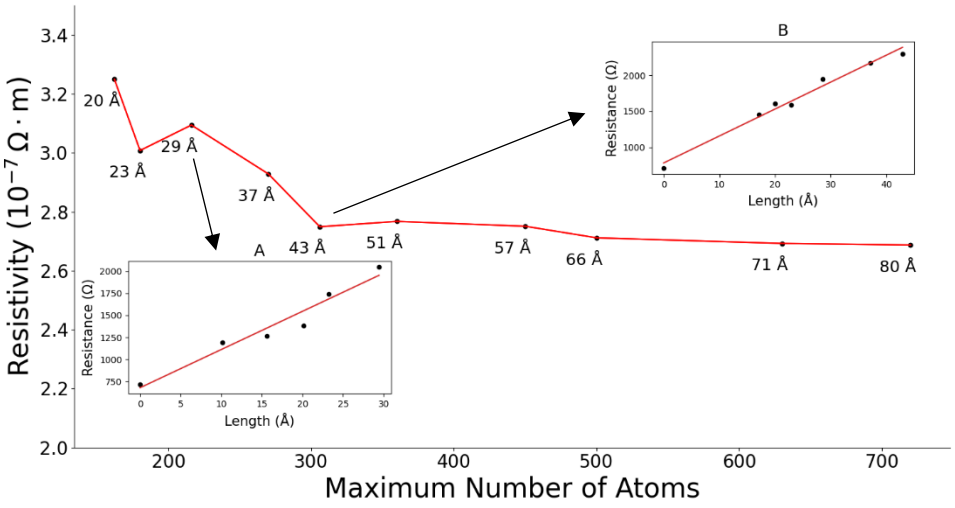

Figure 11 Convergence of resistivity with increasing system size (MD-region length) – Direction [001]

As shown in Figure 11, resistivity is calculated, for the range 0 to X Å, with increasing values of X (29 Å, 37 Å, 43 Å, 51 Å etc.) representing the upper limit of the MD-region length. For each range (0 to X Å), resistance is calculated for a set of different MD-region lengths up till X Å. The slope of the resistance vs. length curve is calculated, providing the resistivity value, as shown by inset A and B in the figure. Figure 11 shows the convergence of resistivity with an increasing value of X for Fe-system with transmission direction [001]. The numbers beneath each resistivity value represent the value of X in the 0 to X range. The x-axis shows the number of atoms in the MD-region (corresponding to X Å). Inset B, which corresponds to the range 0 to X with X= 43 Å and 360 atoms, is chosen for all the models with [001] transmission direction in this study because the resistivity is converged for this range and beyond. This procedure ensures a balance between accuracy and the computational cost of the simulations. Since this study focuses on resistivity calculations with multiple transmission directions and models with defects (vacancies and grain boundary), similar procedures are carried out to make sure that all the models are well converged. In case of crystallographic directions [111] and [$1\bar{1}0$], X=89 Å (458 atoms) and X= 69 Å (458

atoms) respectively are chosen as the upper limit of length in the MD-region of the model. Figure 12 and Figure 13 show the convergence plots for crystallographic directions [111] and [$1\bar{1}0$] respectively. In case of vacancies, same model is used as the one used in the case of examining the crystallographic direction [001] (since it only involves removing a few Fe atoms), therefore the same convergence results apply to this case as shown in Figure 11. For studying the resistivity with grain boundaries, a model with X= 69 Å (330 atoms) was selected based on the convergence results shown in Figure 14.

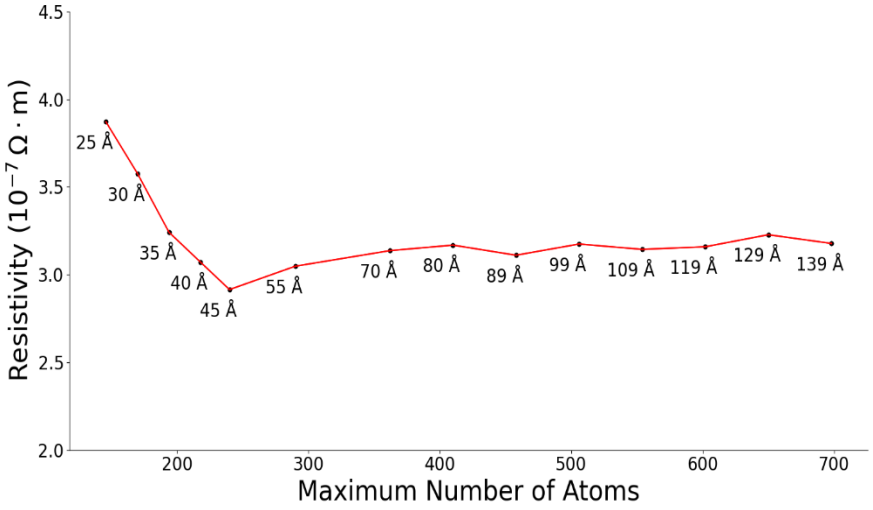

Figure 12 Convergence of resistivity with increasing system size (MD-region length) - Direction [111]

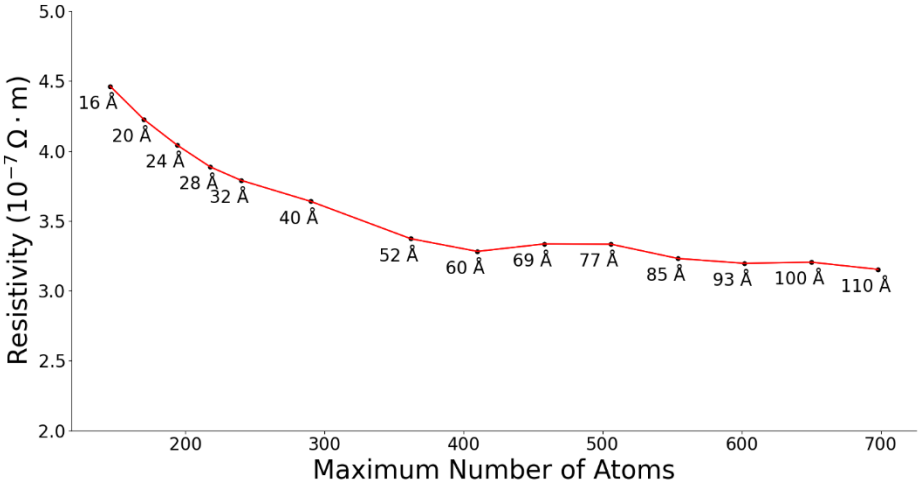

Figure 13 Convergence of resistivity with increasing system size (MD-region length) - Direction [$1\bar{1}0$]

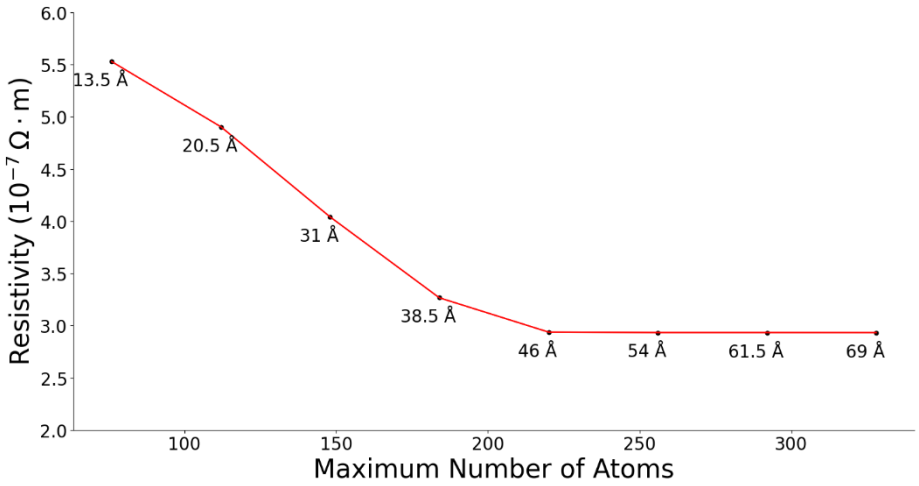

Figure 14 Convergence of resistivity with increasing system size (MD-region length) - Grain boundary model

Besides the size of the model, it is important to converge the k-point mesh in the model since a finer mesh leads to more accurate results. At the same time, the increase in the number of k-points also increases the computational resources required. Therefore, resistivity is calculated with different number of k-points in the model and the point where resistivity values start to converge is chosen to be used in the rest of the calculations. The resistivity value is calculated with different total number of k-points in the model (including transverse and transport directions). As shown in Figure 15, convergence is achieved at 20,000 k-points which was chosen for further simulations. This number was found to be consistent for all the models studied in this research.

Once the models are converged, a test case is set up to ensure that the resistivity values being obtained are accurate. For this, the resistivity of pure Fe and Fe-C is calculated by using the model with transmission direction [001] without H. The obtained values are then compared to the experimental values present in the literature.

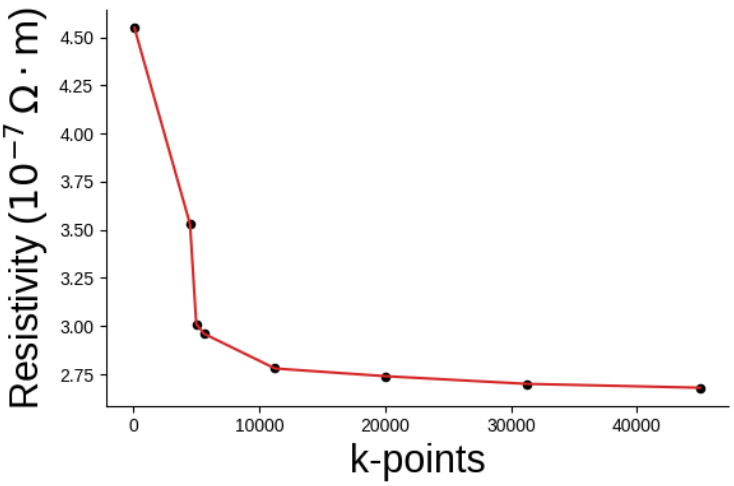

Figure 15 Convergence of resistivity with increasing number of k-points used in DFT calculation.

The resistivities obtained are given in Table 1, which shows that the calculated values in this work are close to those reported experimentally in the literature [68], [69], [70]. The Fe-C system is compared with 4340 steel and 1018 steel, using [69] and [70] respectively, just because the model represents a steel-like system. That is not to state that it is exactly like 4340 and 1018 steel which have grain boundaries, other alloying elements, defects, different phases, and phase distributions. Rather it is to verify if the values obtained are in the same order of magnitude and that the models are working appropriately.

Table 1 Resistivity of Fe and Fe-C system without hydrogen

System	Simulated Resistivity (10^{-7}) (Ω.m)	Literature (Experimental) (10^{-7}) (Ω.m)
Fe	2.75	1.00 [68]
Fe-C	3.52	2.48 [69], 1.59 [70]

The carbon concentration in this study is kept at 2 atoms per model to keep the models consistent throughout, which corresponds to 0.1 to 0.15 weight % among all models. According to Fukuda et al. [71], C atoms prefer octahedral sites and H atoms tetrahedral sites due to their atomic sizes and interactions within the steel matrix, optimizing lattice stability and electronic configurations. Therefore, C atoms are added on random octahedral sites and H atoms are added on random tetrahedral sites in the MD region of the model, utilizing QuantumATK Builder tool, and the resistivity of the Fe and Fe-C system is calculated for varying concentrations of H (0 to 6 atomic %) in these systems. Existing literature, corroborated by Fe-H phase diagrams, posits that hydrogen solubility in alpha Fe is very low (the order of magnitude is 10^{-8} H atoms per Fe atom which is 0.000001 atomic% H) at room temperature [48], [57], [72]. For this study, the chosen hydrogen atomic percentage is notably higher (0 to 6 atomic %) than this small value due to the size limitations inherent to DFT models; the minute percentages (a few parts per million) of H mentioned in the stated studies are not feasible in this context. Therefore, the selected range serves to illustrate potential trends in the change in resistivity at different H-concentrations. Figure 16 shows the Fe-C model with 6 atomic% H. Since H and C atoms are added on random basis, the potential effects of change in their position in the model are discussed in results and discussion

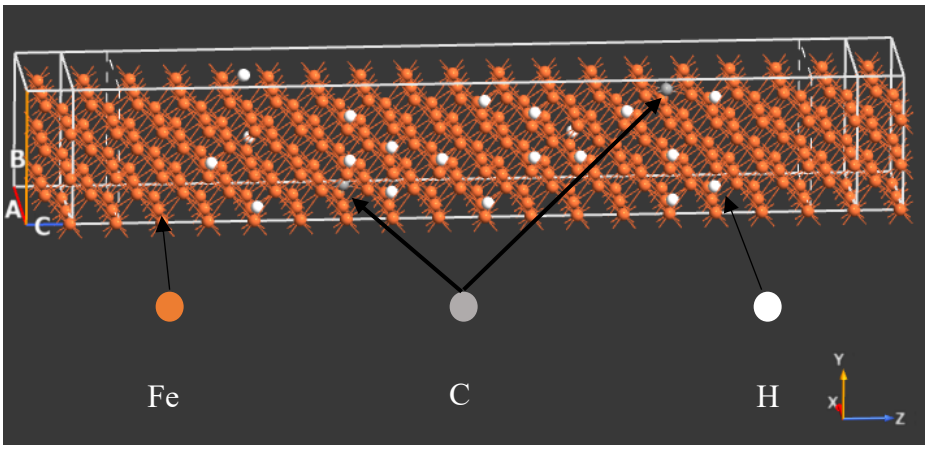

Figure 16 Fe-C model with 6 atomic % H

section. Moreover, H is uniformly distributed in the models as shown in the figure. In bulk steel, H tends to be localized. However, given the small size of models in this study, they can represent localized regions in bulk steel where H tends to concentrate.

For crystallographic direction [001] the resistivity of both Fe and Fe-C systems is calculated at different hydrogen concentrations to study the difference between them. For the other two directions, [111] and $[1\bar{1}0]$, the resistivity only for the Fe-C system was studied. The key objective here was to investigate how the resistivity of the Fe-C system responds to varied H-concentrations in these specific crystallographic directions, as the difference between the Fe and Fe-C systems had already been determined in the [001] direction.

The focus of this study was also expanded beyond perfect crystal models with interstitially located hydrogen atoms to explore the impact of hydrogen on the resistivity of the models with defects. Specifically, models with vacancies were considered to simulate the imperfect real-world lattice structures. A single vacancy is created in the [001] Fe model. The decision to create a single vacancy warrants clarification through an understanding of the Arrhenius law for the number of vacancies in a material [27], [73]. It describes the temperature dependence of the number of vacancies (empty atomic sites) in a crystalline solid. The law is expressed by the equation 9 [27]:

$$N_v = N\, exp\,(-\frac{Q}{kT}) \tag{9}$$

Where N_v is the number of vacancies at a given temperature, N is the total number of atoms in the material/model, Q is the activation energy for vacancy formation (usually in joules or electron volts), k is the Boltzmann constant (1.38×10^{-23} J/K), and T is the temperature in Kelvin. For a range of Q within 1.3-1.7 eV for alpha Fe [74] and at room temperature, the number of vacancies in a model of N=360 is of the order 10^{-20} or smaller. Similarly, the model size (number of Fe

atoms) required to create one vacancy would be of the order 10^{30} or more which is not feasible in DFT due to limitations in computational resources. To navigate around this constraint, a model with one vacancy and 360 atoms was deliberately created, even though it technically represents a higher-than-average vacancy concentration. The aim was to understand the general trend of resistivity changes when vacancies are present in the system.

Since this study also explores the changes in resistivity in the presence of both H and defects, previous literature was consulted regarding possible vacancy-hydrogen configurations that could be modeled. A key takeaway from the work of Gavriljuk et al. [48] is that H displays a significant affinity towards vacancies, a conclusion substantiated by numerous studies that have leveraged first-principle calculations to investigate hydrogen-vacancy interactions [58], [59], [61]. An especially notable study [61] posits that when H is in the vicinity of a vacancy to form a VH (vacancy-hydrogen) complex, an electron flow occurs from the nearby Fe atoms to the hydrogen atoms due to hybridization between them. This leads to the hydrogen atoms acquiring a negative charge and, in turn, triggering a repulsive force among themselves [61]. As the number of hydrogen atoms in the VH complex increases, so does the strength of this repulsive force, making larger complexes, such as VH4, VH5, and VH6, unviable under ambient temperature and pressure conditions. According to the authors, VH2 complexes (a vacancy coupled with two Hydrogen atoms) are the prevailing hydrogen-vacancy complexes under ambient conditions, and the stability of VH2 complexes can be attributed to a delicate balance between the forces of hybridization and repulsion [61]. These findings have been supported in literature by multiple studies [58], [59], [62], which, through first-principles, observed a decline in the binding energy of VH complexes as the number of hydrogen atoms grows beyond two. Similarly, Besenbacher et al. [62] validated these results through experimental investigations. Importantly, Mirzaev et al. [58], compared the

binding energies of VH complexes calculated through first-principles and experimental techniques, thereby reinforcing the credibility of these findings. This consolidation of previous research thus provides a strong scientific basis for examining the impact of a VH2 complex (a vacancy coupled with two Hydrogen atoms) on the resistivity of an Fe-based system in this study since it is the vacancy-hydrogen configuration that is most likely to occur. Moreover, the VH3 complex (a vacancy combined with three Hydrogen atoms) will be explored as an additional aspect. The aforementioned studies describe the VH2 complex as a line-shaped cluster assembled around the vacancy, as shown in Figure 17. With this in mind, as depicted in Figure 18 and Figure 19, three different configurations were considered: an Fe model with a single vacancy, an Fe model hosting a VH2 complex, and an Fe model with a VH3 complex.

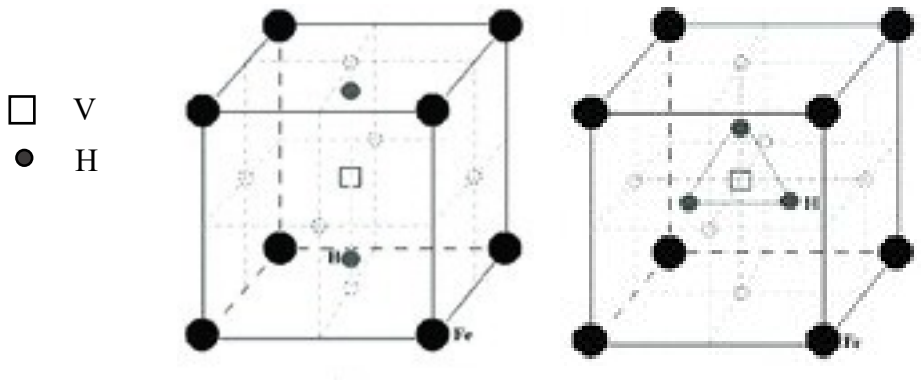

Figure 17 VH2 and VH3 configurations [58]

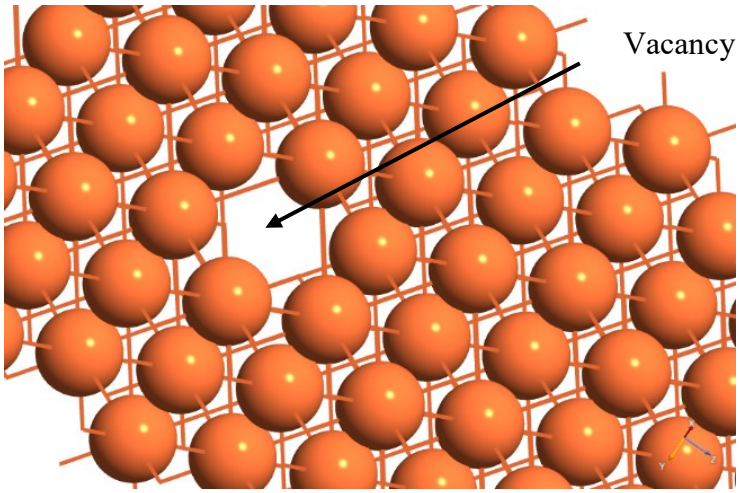

Figure 18 Fe-model with a vacancy

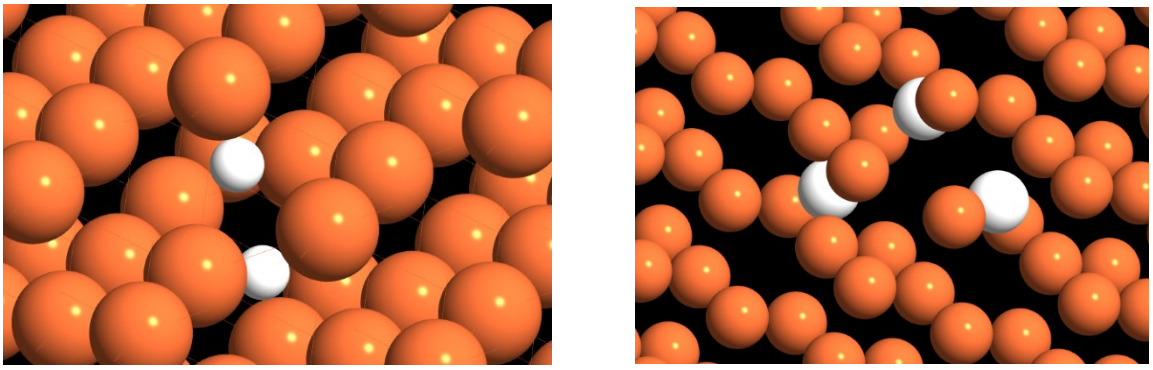

Figure 19 VH2 (left) and VH3 (right) complex

As part of the ongoing analysis of the effects of defects on the resistivity of Fe, the study was extended to incorporate the influence of grain boundaries. The focus here is on the Σ5 [100]/[$\bar{1}$00] Twist grain boundary, across the following three distinct scenarios. A pure Fe model with the grain boundary located at the center is created as illustrated in Figure 20. In a second scenario, a concentration of 4.4 atomic % hydrogen atoms is incorporated at the grain boundary within the same Fe model from the previous scenario, as shown in Figure 21. Finally, Figure 22 portrays the third scenario where a 4.4 atomic % concentration of hydrogen atoms is dispersed randomly at interstitial sites throughout the model, while maintaining the central grain boundary.

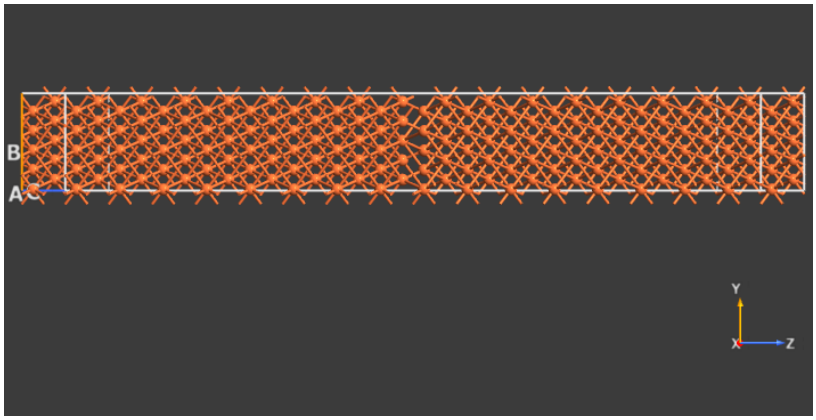

Figure 20 Fe model with the Σ5 [100]/[$\bar{1}$00] twist grain boundary located at the center.

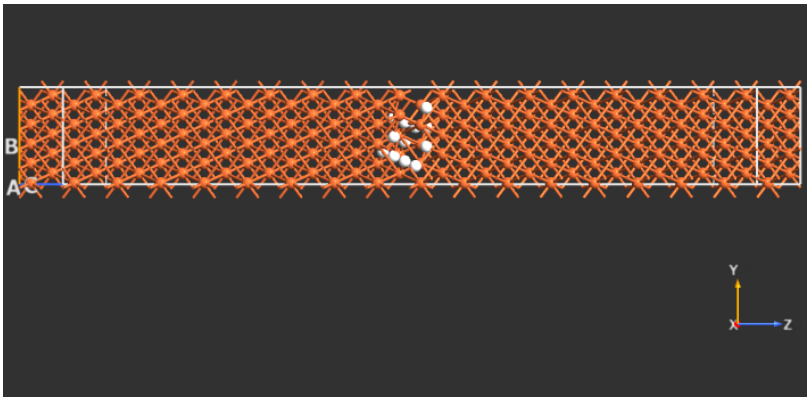

Figure 21 Fe model with H located at the Σ5 [100]/[$\bar{1}$00] twist grain boundary

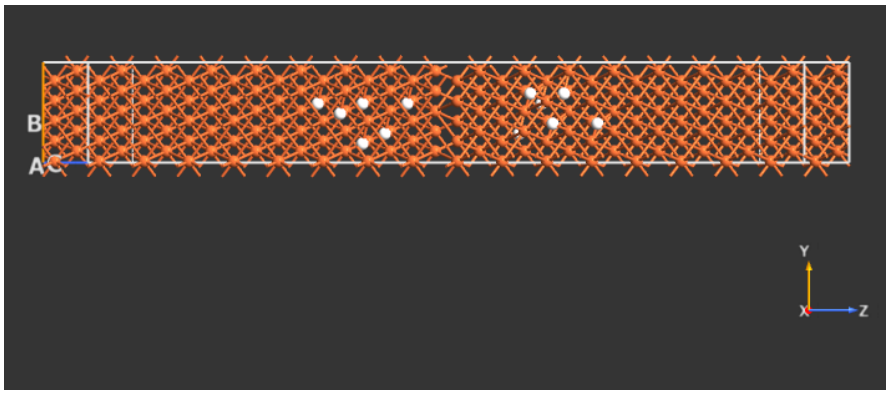

Figure 22 Fe model with the Σ5 [100]/[$\bar{1}$00] twist grain boundary along with dispersed interstitial H atoms

A model incorporating a Σ5 [001]/[$\bar{2}\bar{1}$0] symmetric tilt grain boundary was also developed, as depicted in Figure 23, for all three cases with 4.6 atomic % concentration of H, with an intention to discern if trends similar to those observed in twist grain boundary scenarios could also be observed here.

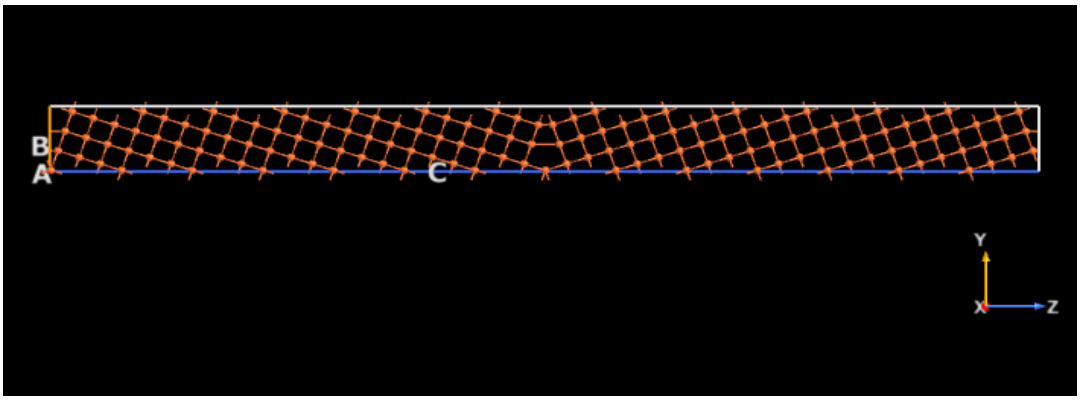

Figure 23 Fe model with A Σ5 [001]/[$\bar{2}\bar{1}$0] symmetric tilt grain boundary

Results and Discussion

This chapter offers a detailed analysis and interpretation of the simulation results centered on understanding the resistivity of Fe and Fe-C systems. Initially, the focus is directed towards assessing how electron transmission across different crystallographic directions of Fe is impacted in the presence of hydrogen and how this, in turn, influences resistivity. The scope of the analysis broadens from pure crystal orientations to configurations with defects, including vacancies and grain boundaries. Such a structured exploration ensures that readers gain a comprehensive understanding of the resistivity of Fe under a myriad of conditions. The concluding section of the chapter delves into a cohesive discussion, shedding light on several factors that impact resistivity such as density of states, electron transmission, and electron density distribution.

1.11 Electronic Transmission and Hydrogen

Methodology section demonstrated, with the help of equations 5 and 6, that resistance and resistivity depend on the electron transmission in the system. Therefore, if H addition impacts the transmission coefficient, the effects will certainly translate into the resistivity of the system as well. The following sections investigate the impacts of H on electronic transmission and structure.

1.11.1 General Trends in Electron Transmission in Fe with Hydrogen

Resistivity in metals arises when electrons undergo scattering which is due to an imperfect lattice [75]. Imperfections in the lattice can be attributed to two factors: lattice vibrations (phonons) around equilibrium positions of atoms, and impurities [76]. The probability of an electron scattering in unit time is the sum of the probability of scattering from both factors and they are independent of each other [75], [76]. In this study, H can be considered as an impurity in the pure Fe system. Therefore, it should provide a scattering effect and consequently affect the transmission

of electrons from the left (source) to the right (drain) electrode. This effect is quantitatively assessed through the transmission coefficient, as delineated in equation 6. The transmission spectrum serves to quantify the impact of these scattering events on electron transport, mapping how electrons are hindered or facilitated in their journey across the device. Figure 24 illustrates the variations in the transmission coefficient within the Fe system, with and without H. Here, k_A and k_B denote the sets of possible electron states at the left and right electrodes, respectively. These states, characterized by their wavevectors, encapsulate the momentum and, indirectly, the energy of the electrons within the crystalline lattice of the material. Thus, the transmission spectrum provides a visual representation of the probability that electrons can successfully transition from a state in k_A to a state in k_B, highlighting the pathway of electron transport across the device. It can be observed that the transmission spectrum of the pure Fe system has darker and more defined colors, representing higher transmission coefficients and, by extension, more efficient electron transport. There is a noticeable alteration in color definition of the spectrum, as H is added to the system, with lighter and lesser defined colors, representing lower values of the transmission spectrum. Thus, the presence of H as an impurity impedes electron flow and contributes to a less distinct transmission spectrum.

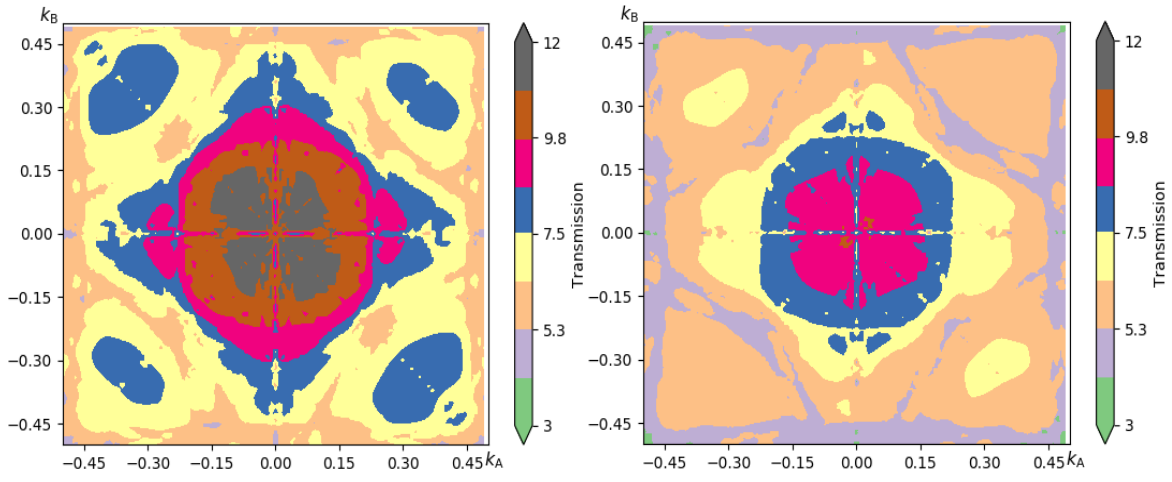

(a) (b)

Figure 24 Transmission spectrum of Fe-C system: (a) 0% H, (b) 6 atomic % H

1.11.2 Electronic Structure Alterations Caused by Hydrogen

Since transmission coefficient is dictated by the ease with which electrons navigate through the lattice, it is imperative to observe the electronic structure of the Fe system with and without H. In order to scatter the electrons and affect their transmission, H must have altered the system at the electronic level.

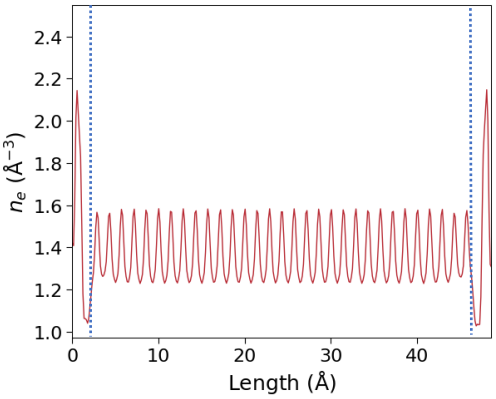

Figure 25 Electron density of Fe system (without H) – Vertical dashed lines represent electrodes

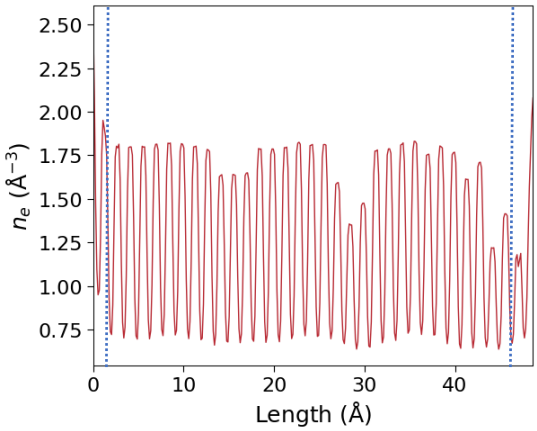

Figure 26 Electron density of Fe system (with H)

Figure 25 and Figure 26 show the electron density (ED) plotted along the longitudinal direction (transmission direction) of the two-probe system without and with H respectively. Higher density regions are indicative of areas where the probability of finding an electron is relatively higher. In the model without H, the ED is uniformly distributed as shown in Figure 25. Only the extremes have higher density. This observation aligns with the understanding of the electron transport

phenomena in the system - the electrodes, being the source and drain of electron waves, naturally harbor a higher electron density. On the other hand, the central region has a uniform dispersion of electrons. Upon the addition of H, non-uniform ED peaks are observed in the system, as shown in Figure 26. Therefore, H is causing disruption in the electronic structure of the Fe system. This observation can be further corroborated through different kind of analyses. The calculation of Electron Localization Function (ELF) is one of them [77]. ELF depicts the spatial distribution of electrons. Lower values at a certain point indicate that electrons are not localized in that region, and higher values are symbolic of localization. Figure 27 shows ELF in the Fe system with and without H. In the uniform electron distribution scenario, the absence of hydrogen allows for an equitable dispersion of electrons throughout the system. Contrastingly, in the presence of hydrogen, there is a discernible shift in electron localization, giving rise to a non-uniform ELF along the length of MD-region.

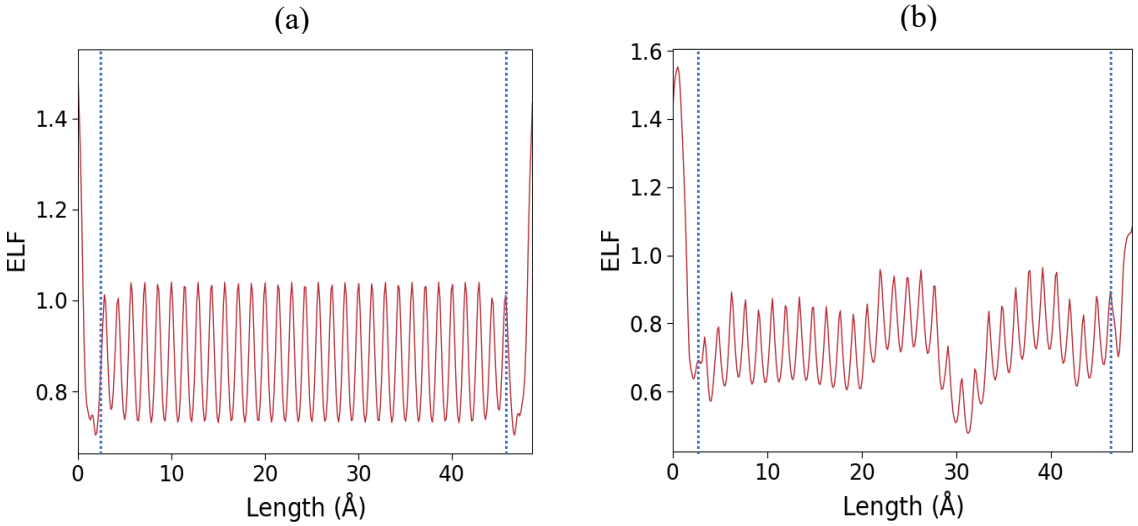

Figure 27 Electron localization function of Fe system: (a) without H (b) with H

The localization of electrons can be further visualized on the plane/layer of atoms where H is added. Figure 29 and Figure 28 show electron localization in the same plane from the model without H-atoms and the model with H-atoms. The plane 23 Å (measuring with left electrode

included) is chosen because two H atoms are located there in the model with H-atoms. Figure 29 shows that when H is not present at the location, electron cloud is uniformly distributed around the nuclei and the regions around all nuclei are depicted to be equally in the higher range of ELF values. This shows that there is an equal and high possibility of finding electrons around the nuclei. Whereas when H atoms are added, these uniform regions of higher ELF values are broken up into

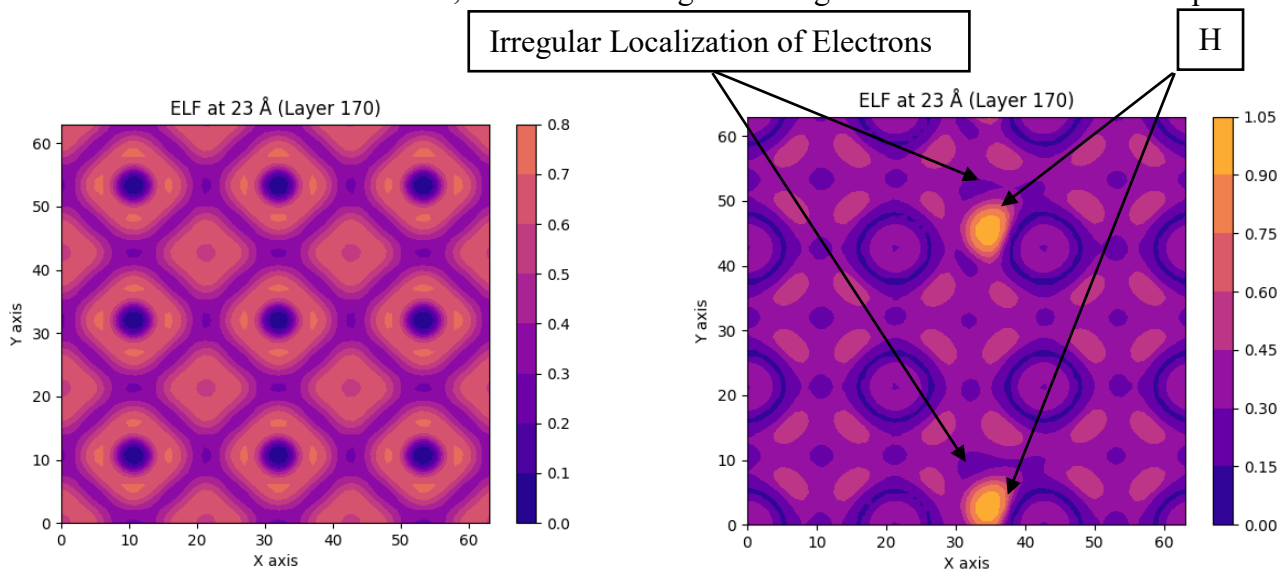

(a) **(b)**

Figure 29 Electron localization heatmap at the same plane from a model without H (a) and with H (b)

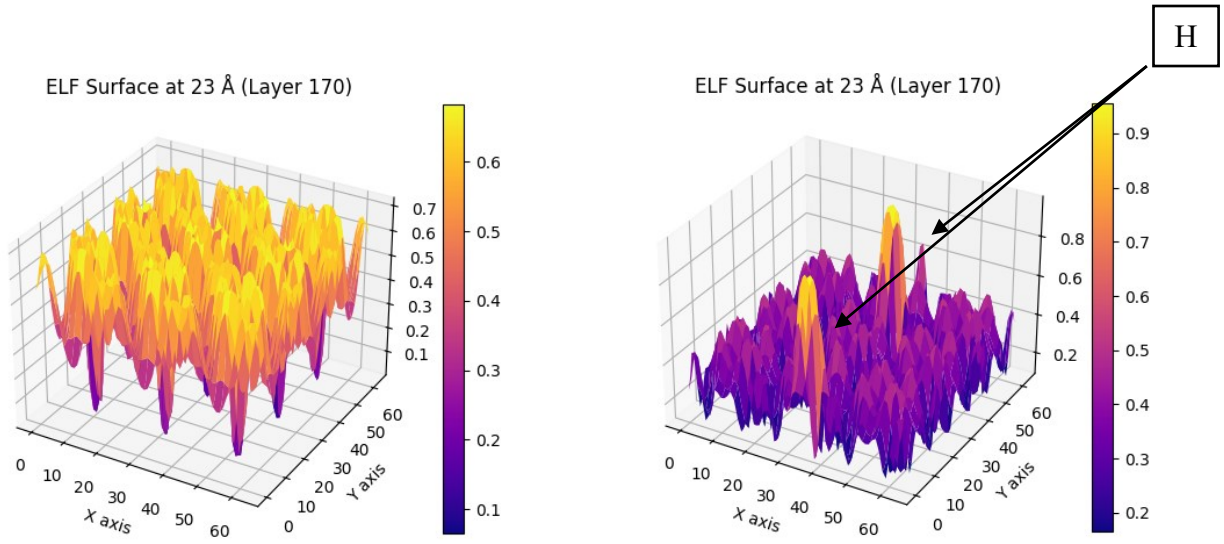

(a) **(b)**

Figure 28 Electron localization surface map at the same plane from a model without H (a) and with H (b)

small irregular pockets which means that electrons are not uniformly distributed in that plane anymore. Especially on observing the location where H atoms are present, the electron clouds of their adjacent Fe atoms are broken into irregular regions. Figure 28 adds to these findings by showing a surface map for ELF at this plane with and without H. In the absence of H, it is observable that the whole surface has equally distributed peaks and valleys. Whereas, when H is added, the surface is irregular and there are two distinct peaks representing H atoms, showing that there is a high and irregular localization of electrons around H atoms which can be attributed to their electronegative behavior.

If electrons are being non-uniformly distributed due to the presence of H, that must cause an imbalance in the elementary charge distribution which is the net charge on individual atoms in the system. In the absence of H, the Fe system has uniform charge distribution between individual Fe atoms, as shown in Figure 30. More negative values (darker colors) correspond to areas of higher electron density (concentration of electrons), and more positive values (lighter colors) correspond to a lower electron density (scarcity of electrons). Electrodes being the source and sink understandably exhibit darker colors whereas the majority of Fe atoms (in the central region)

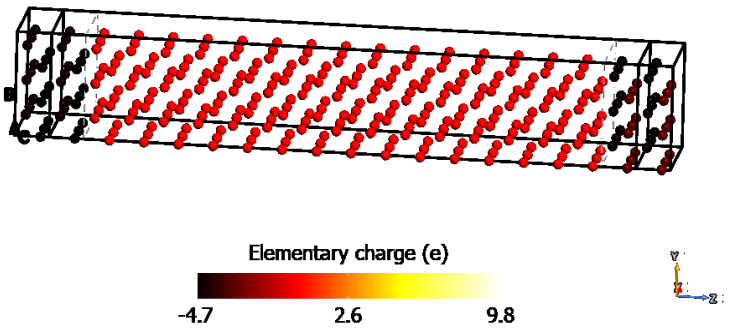

Figure 30 Elementary charge distribution in Fe system (without H)

exhibited red-colored regions (near zero charge). However, upon introducing H atoms, as shown in Figure 31 (H atoms are shown in bigger size for visual reference), a shift is observed. Many Fe atoms shift from a dark red colored region to an orange color, transitioning towards the positive side of the spectrum, indicating that overall, they have lower electron density as compared to the pure Fe model. Some Fe atoms in the model exhibit even lighter colors, suggesting an even lower electron density. This distribution indicates that the introduction of H introduces an imbalance in

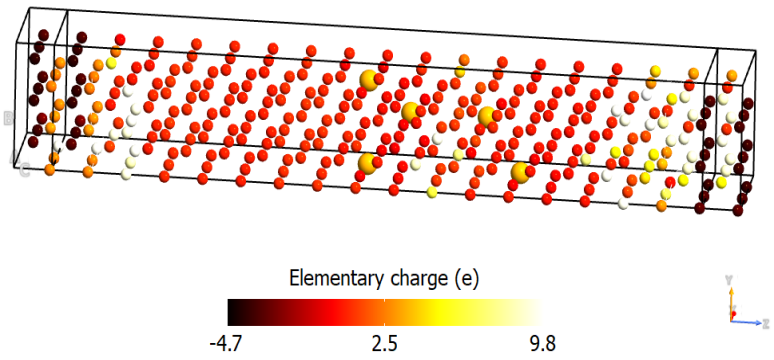

Figure 31 Elementary charge distribution in Fe system (with H – represented by big atoms for visual reference)

the electronic charge distribution in the system, which provides another evidence of non-uniform electron density in the Fe-H system as shown in this section. This non-uniformity leads to some regions with increased electron density and some regions with decreased electron density which interrupts favorable pathways for the electron wave to travel from left electrode to the right electrode hence leading to lower value of the transmission coefficient, calculated through equation 6, and demonstrated in the transmission spectrum depicted in Figure 24. The following part in this study focuses on observing the effect of H atoms on the resistivity of Fe-based systems. Since methodology section interconnects transmission coefficient, conductance and subsequently resistivity with the help of equations 5, 6 and 7, it can be hypothesized that the effects of H on

transmission and electronic structure, as shown in this section, are expected to translate into the behavior of resistivity. The following section explores this aspect.

1.11.3 Resistivity Analysis in the Fe and Fe-C systems With and Without Hydrogen

This section explores the changes in resistivity of Fe and Fe-C system at different H concentrations. As depicted in Figure 32, the slope of the curve between resistance and MD region length increases with a rise in hydrogen concentration from 0-6 atomic % in the Fe system. This trend suggests an increase in resistivity. Since the presence of H disrupts electronic structure, as discussed in Section 1.11.2, the increase in H-concentration leads to a higher level of disruption and hence higher resistivity, as shown in Figure 32. The Fe-C system manifests a similar pattern of an increase in resistivity as demonstrated in Figure 33. The resistivity of both Fe and Fe-C systems with respect to increasing H-concentration is further depicted in Figure 34 and Figure 35, respectively. A notable observation is the linear relationship between resistivity and H-concentration, which signifies a proportional increase in resistivity with increasing H-concentration.

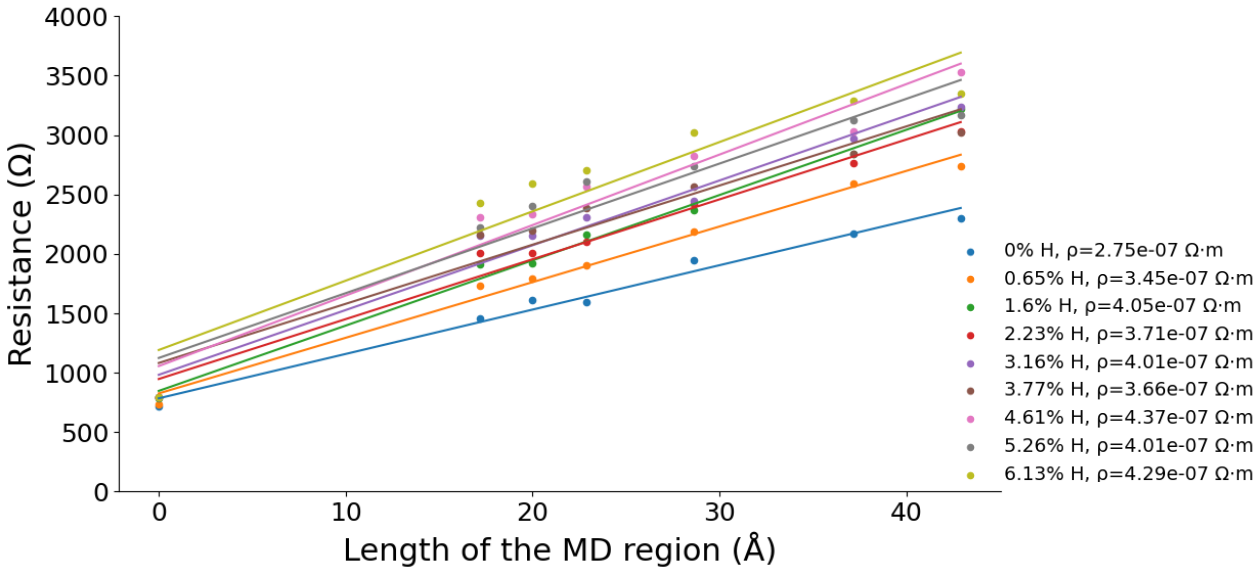

Figure 32 Resistance plots for Fe system at 0-6 atomic % H concentration

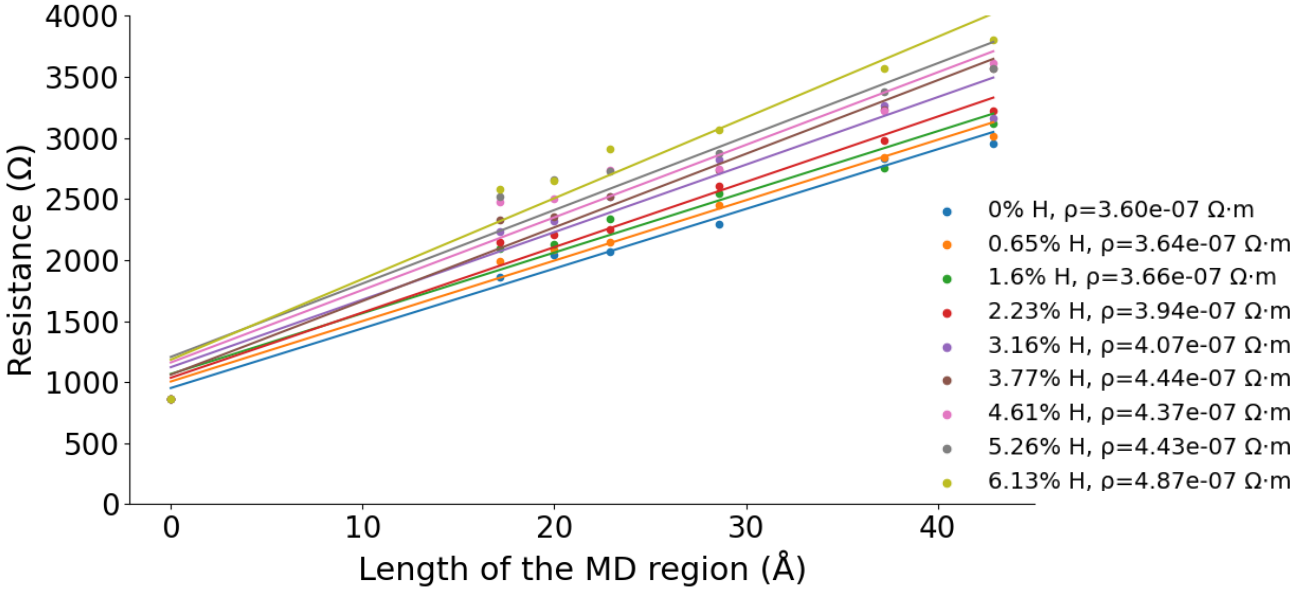

Figure 33 Resistance plots for Fe-C System at 0-6 atomic % H concentration

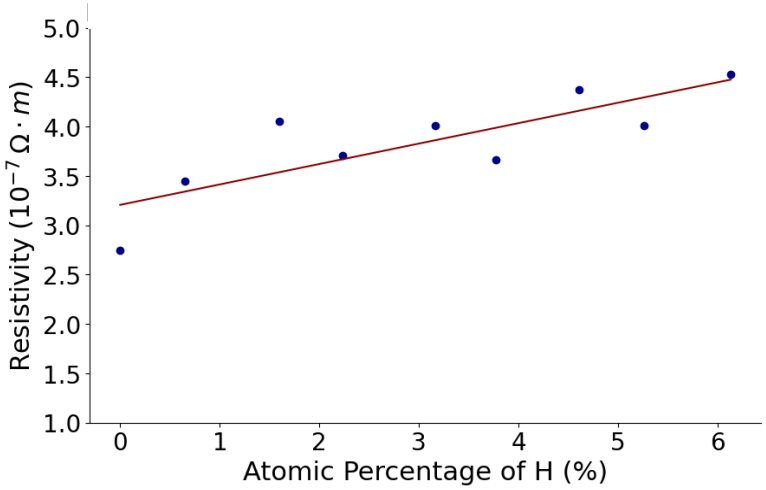

Figure 34 Variation in resistivity with hydrogen concentration in Fe system

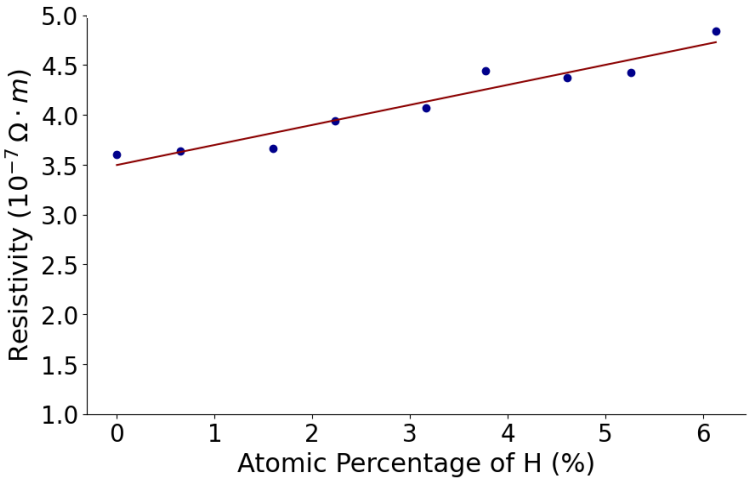

Figure 35 Variation in resistivity with hydrogen concentration in Fe-C system

The electrical conductivity and resistivity of a material are fundamentally associated with the quantity of free electrons present within it [75]. Consequently, understanding the impact of H incorporation on the free electron count of material becomes crucial. This necessitates an investigation into whether the addition of H alters the number of free electrons and, if so, the degree of this change. A pivotal method for examining this effect involves analyzing the Density of States (DOS) at Fermi level, which quantifies the available free states for electron occupancy. The availability of a greater number of states at Fermi level directly correlates with an increase in the presence of free electrons within the system. In metallic systems, only the electrons located near the Fermi level are reported to actively participate in the conduction process [75], [76]. Therefore, DOS at Fermi level needs to be monitored. All the studies that explore the change in DOS of Fe-based systems upon the introduction of H did so in order to connect the change in number of electrons with mechanical properties and grain boundary mobility [10], [51], [56]. For instance, Teus et al. [52] show that H addition contributes slightly to the DOS at the Fermi level,

as shown in Figure 36. This slight elevation in DOS is then linked to an improved grain boundary mobility. In this study the impact of impurities on DOS at system-wide scale is briefly explored, as the number of free electrons present might affect the resistivity. As demonstrated in Figure 37, the integration of C and H into the Fe system rarely influences the DOS at the Fermi level, set at 0 eVs.

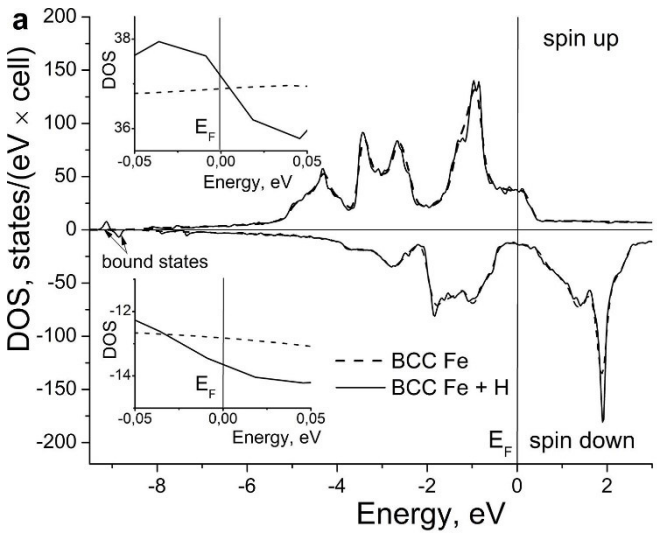

Figure 36 DOS in BCC Fe and Fe-H system [49]

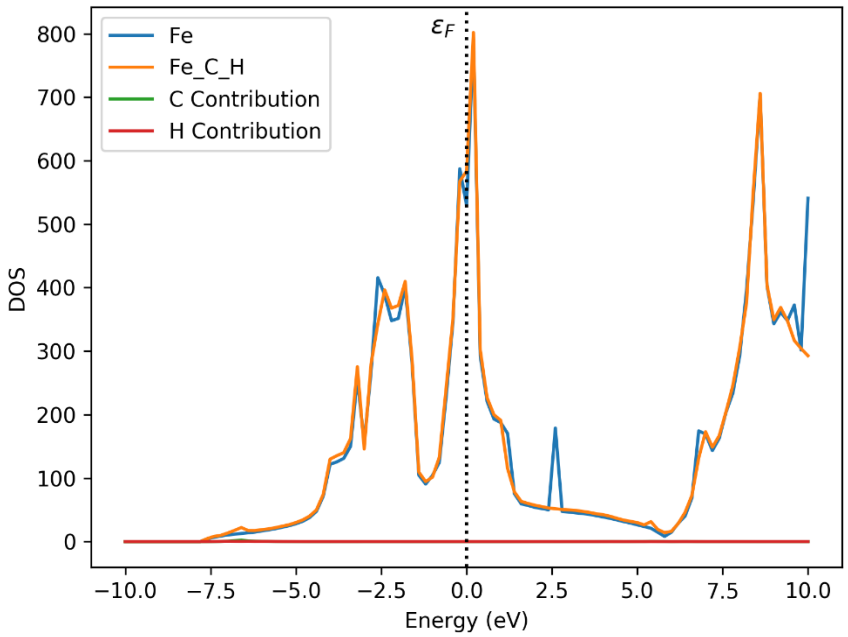

Figure 37 DOS at and around fermi level in Fe and Fe-C-H model

Besides the system-wide DOS, localized changes in DOS were also observed for Fe atoms in the vicinity of sites where H atoms are added. Figure 38 and Figure 39 respectively display the DOS of an individual Fe atom in a pure Fe model and the DOS of an individual Fe atom in proximity to a H atom in the Fe-H model. From these figures, it is discernible that the presence of H barely increases the DOS of the adjacent Fe atom at the Fermi level from 1.9 to 2.1. In the context of this research, the primary concern is the influence of DOS on the system-wide electrical resistivity, where localized changes in the number of free electrons, particularly of such a small magnitude, are deemed less significant. Consequently, the observed increase in resistivity is attributed to the disruption in electron distribution caused by the introduction of H into the system, as detailed in Sections 1.11.1 and 1.11.2, rather than to changes in the free electron count.

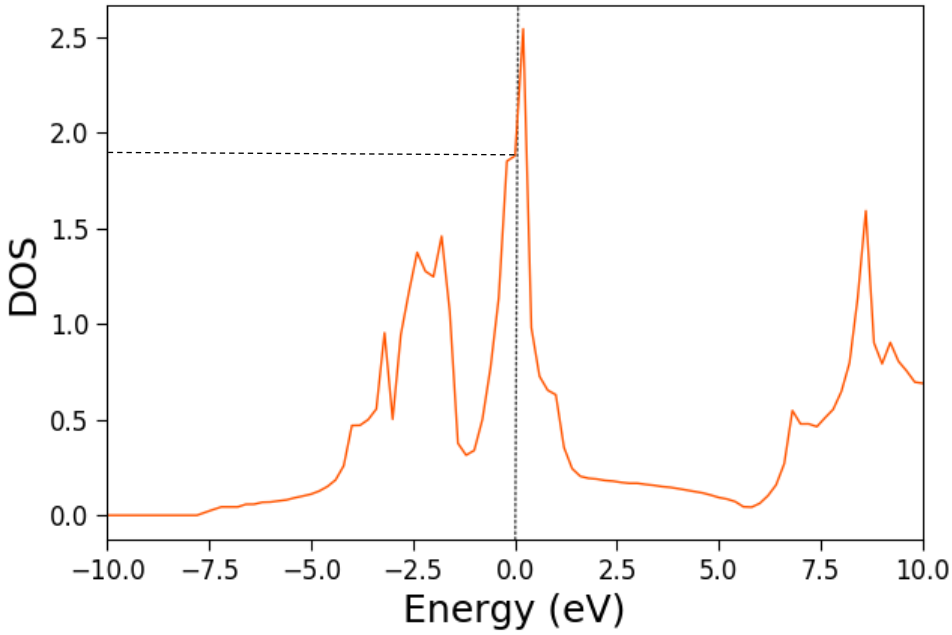

Figure 38 DOS of an individual Fe atom in a pure Fe model

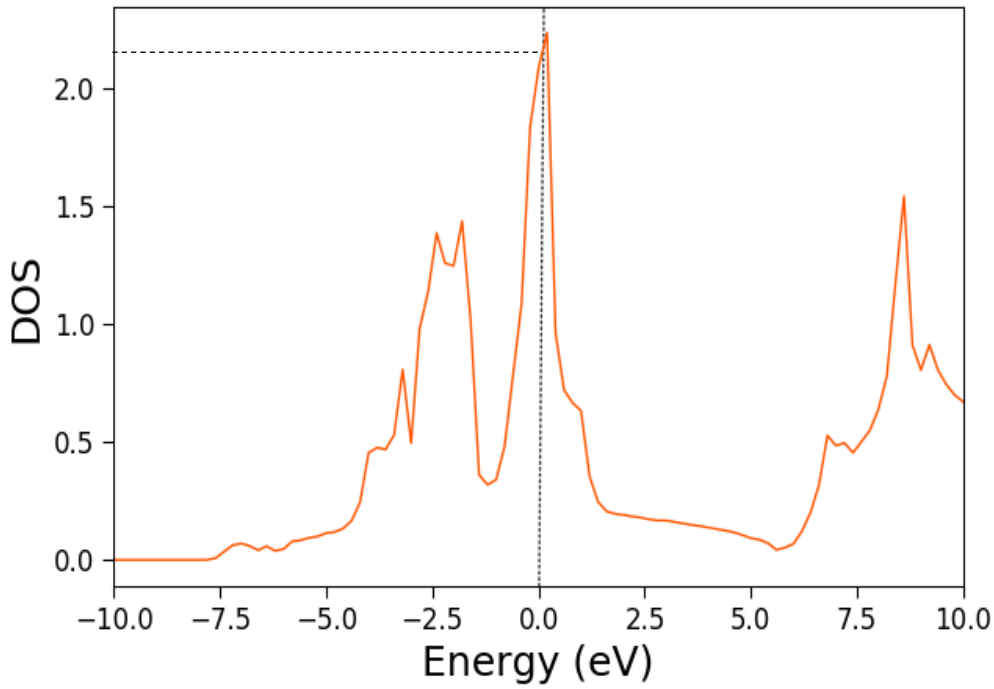

Figure 39 DOS of an individual Fe atom in proximity to a hydrogen atom in the Fe-H model

As mentioned in the methodology section, the positions of H and C atoms in the Fe and Fe-C models designed for this study are chosen on a random basis. An effort is made to position and disperse these impurities in the middle of the central region of the models. However, a hypothesis can be made that different configurations, consisting of different positions of H and C atoms, with same percentage of these impurities, should affect the transmission of electrons differently. This hypothesis that the transmission of the system also depends on the arrangement of H and C atoms in the MD region is briefly explored. In order to do so, for Fe-C as well as the Fe-H systems, the following three cases have been investigated: (i) 1 random H/C atom, (ii) 2 consecutive H/C atoms (one atom behind the other), and (iii) 2 random H/C atoms at the interstitial positions as shown in Figure 40. This figure only displays the models with C atoms however, similar configurations were used for the Fe system with H atoms.

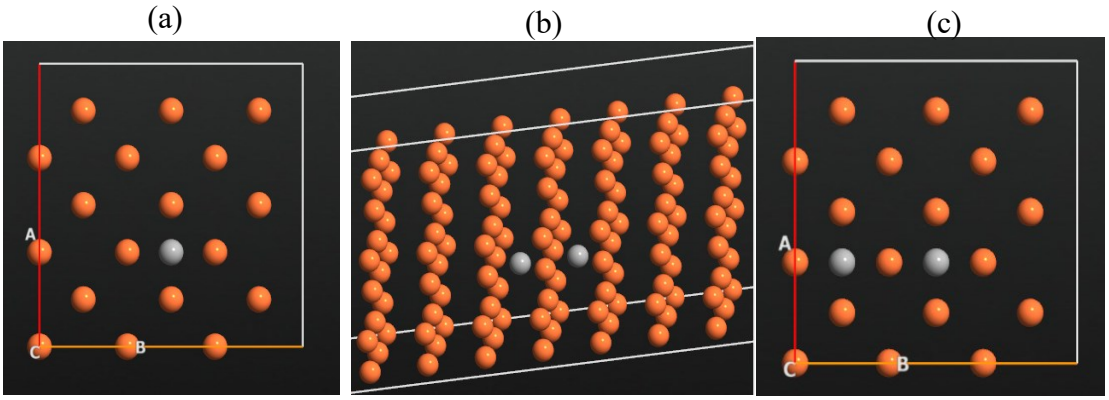

Figure 40 Different arrangements of C atoms in the Fe system to investigate a change in transmission due to the position of C atoms: (a) 1 random C atom – view in AB plane, (b) 2 consecutive C atoms- Isometric view in direction C, (c) 2 random C atoms – view in AB plane.

The results in Table 2 and Table 3 show that the transmission is reduced more in case (iii) as compared to cases (i) and (ii), and hence resistivity in that case is higher. These results portray that if impurity atoms are placed adjacently (one behind the other), they affect electron transmission less as compared to when they are placed in random non-adjacent positions. Furthermore, as compared in Figure 41, the transmission in the case of Fe with only H atoms in the three aforementioned cases is higher compared to the Fe system with C atoms. That is because the C atom is bigger thus, it affects the transmission more as compared to the H atom. Therefore, the resistivity for the Fe-C system is distinctly higher than the Fe system, as illustrated in Figure 42. This differential implies that the Fe-C system exhibits a greater resistivity value compared to the Fe system when subjected to varying H-concentrations and also when H is not present in the system.

Table 2 Transmission in Fe-C system

Configuration	Transmission Coefficient	Resistivity (10^{-7}) (Ω.m)
1 C atom	8.8	3.1
2 consecutive C atoms	8.7	3.4
2 random C atoms	8.3	3.6

Table 3 Transmission in Fe-H system

Configuration	Transmission Coefficient	Resistivity (10^{-7}) (Ω.m)
1 H atom	9.7	2.9
2 consecutive H atoms	9.3	3.1
2 random H atoms	8.8	3.4

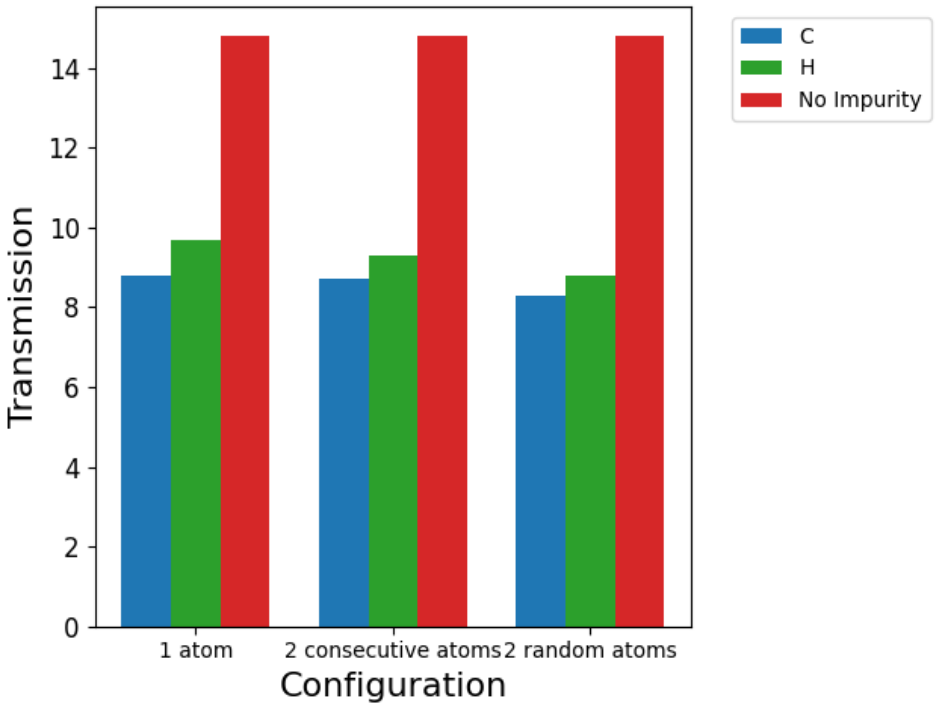

Figure 41 Transmission of Fe system with different configurations of C and H

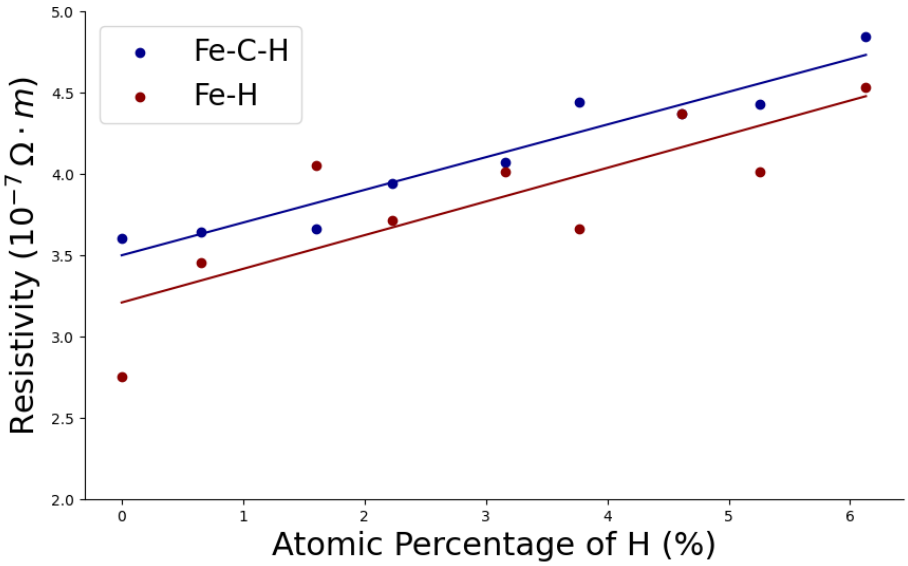

Figure 42 Comparison of resistivity of Fe And Fe-C systems with varying hydrogen concentration

The observed trends in resistivity changes associated with H concentration, as discussed thus far, pertain to the Fe and Fe-C systems, specifically designed with their longitudinal (electron transmission) direction aligned along the [001] crystallographic axis. An additional consideration is the potential anisotropy of resistivity variations with H concentration, suggesting that different trends might manifest across other crystallographic directions. The subsequent section delves into this aspect. As outlined in methodology, this investigation will focus solely on the Fe-C system, given that the distinctions between Fe and Fe-C systems have already been clarified.

1.11.4 Resistivity Analysis by Crystallographic directions

In this section, the resistivity is analyzed through calculations performed when the single crystal conductor is rotated to have the longitudinal direction (electron transmission direction) parallel to two other crystallographic directions, [111] and $[1\bar{1}0]$, with variations in hydrogen concentration from 0 to 6 atomic %. This detailed exploration in different crystallographic directions contributes to a broader understanding of resistivity.

1.11.4.1 Single Crystal Conductor in Direction [111]

In this case, the same methodology was employed as presented in Section 1.11.3, with a key difference that the longitudinal direction of the model and electron transport direction are set to [111]. As demonstrated in Figure 43, the slope of the curve between resistance and MD region length increases with a rise in hydrogen concentration from 0-6 atomic % in the Fe system. This suggests an increase in the resistivity of the Fe-C system in [111] direction as depicted in Figure 44, a similar trend to direction [001], as reported in Section 1.11.3.

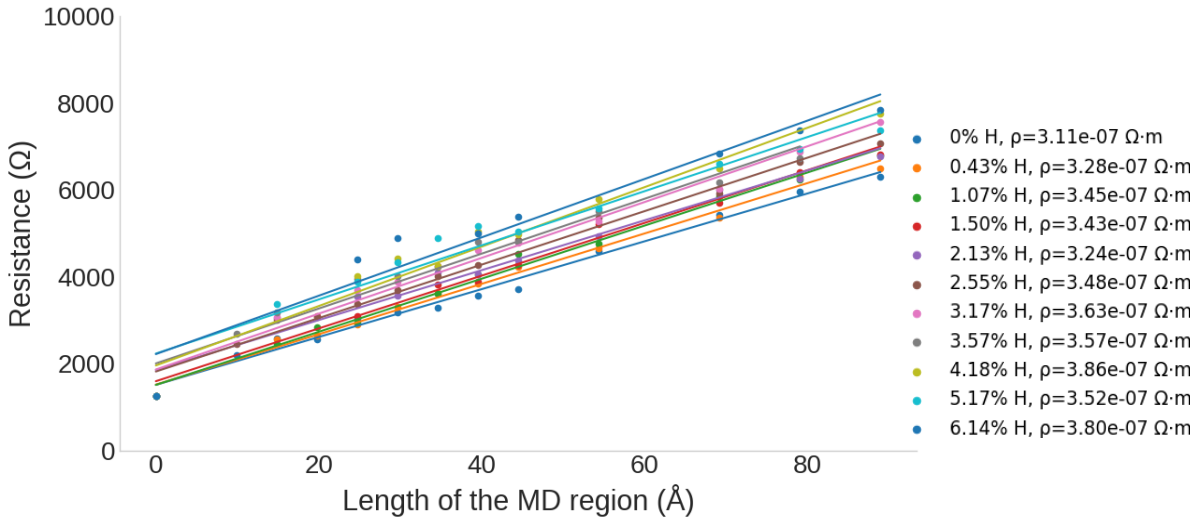

Figure 43 Resistance Plots for Fe-C system at 0-6 atomic % H concentration - Transmission Direction [111]

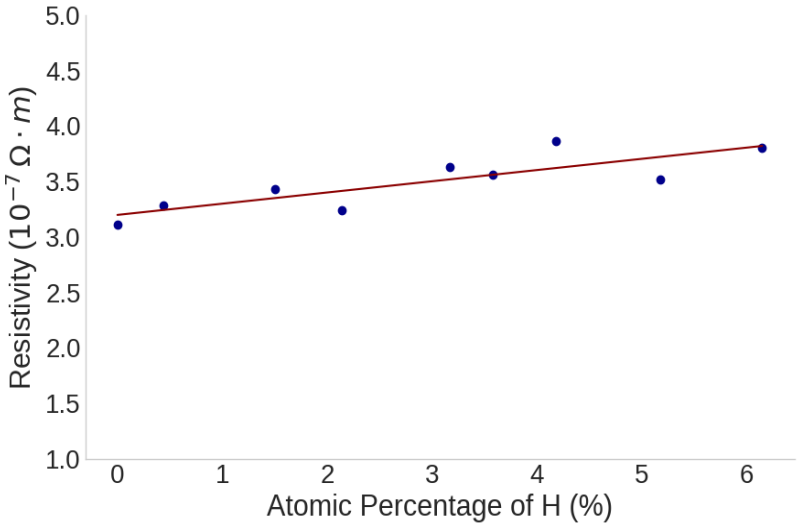

Figure 44 Variation in resistivity with H-concentration in Fe-C system - Direction [111]

1.11.4.2 Single Crystal Conductor in Direction $[1\bar{1}0]$

For the last case, identical computational procedures were carried out as previously outlined, but the longitudinal direction of the model is shifted to $[1\bar{1}0]$. Similar to the other two directions, an upward slope is noticed in the resistance versus length plot for the Fe-C system, as depicted in Figure 45 and Figure 46. Figure 46 shows that the resistivity increases slightly as the hydrogen concentration increases from 0 to 6 atomic % in all three crystallographic directions.

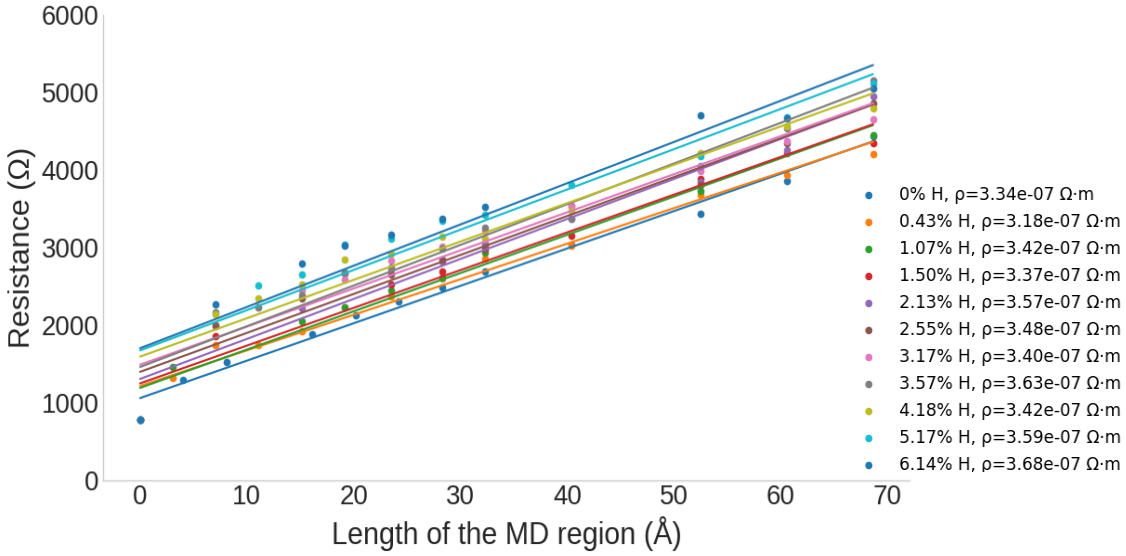

Figure 45 Resistance plots for Fe-C system at 0-6 atomic% H concentration - Transmission Direction $[1\bar{1}0]$

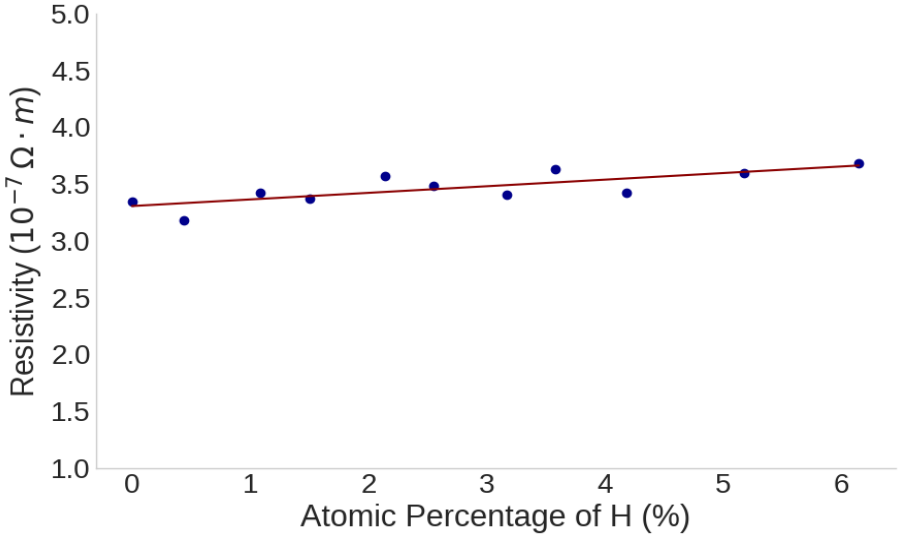

Figure 46 Variation in resistivity with H-concentration in Fe-C system - Direction $[1\bar{1}0]$

1.11.4.3 Comparing Resistivity Variations in Crystallographic Directions [001], [111], and $[1\bar{1}0]$

The purpose of comparing resistivity behavior in three different crystallographic directions was to discern whether the rate of change in resistivity is anisotropic, and to understand how crystal structure influences electrical resistivity in the absence and presence of interstitial H. Figure 47 shows the resistivity behavior for all three directions plotted together. It can be observed that [001] direction has the highest value of resistivity without H present in the system followed by $[1\bar{1}0]$ and then [111]. A possible explanation for this behavior could be the interplanar distance measured by equation 9 [78]:

$$d = \frac{a}{\sqrt{h^2+k^2+l^2}} \quad 9$$

Where a is the lattice constant which is 2.866 Å in this study, and h, k, l are the miller indices of the plane. The [001] direction has the largest interplanar distance (2.866 Å), followed by $[1\bar{1}0]$ (~2.03 Å), and then [111] (~1.65 Å). The higher resistivity values in [001] and $[1\bar{1}0]$ direction without H could be attributed to the longer path electrons must traverse between planes, leading to more significant momentum loss [12] and increased resistivity.

As depicted in Figure 47, the direction [001] has the steepest increase in resistivity with H-concentration followed by direction [111] and direction $[1\bar{1}0]$ both having comparable rates of increase in resistivity. This shows that varying H-concentration affects the resistivity of the model with [001] direction the most. One plausible explanation is that in the BCC Fe structure, the planes in [001] direction are less densely packed compared to the planes in [111] and $[1\bar{1}0]$ directions [79], as visually depicted in Figure 48, allowing interstitial hydrogen to more readily interrupt electron transport between electrodes, thereby having a more pronounced effect on resistivity. This is evidenced by the steeper rate of increase in resistivity observed in the [001] direction with

varying hydrogen concentrations. The objective of this analysis was to determine whether trends in resistivity would vary across different crystallographic directions. Although the examination confirmed a consistent pattern of increased resistivity with rising hydrogen concentration across all directions, the rate of this increase proved to be direction-dependent. However, it is crucial to note that the overall magnitudes of resistivity could be in close proximity between certain directions as observed across [111] and $[1\bar{1}0]$ directions.

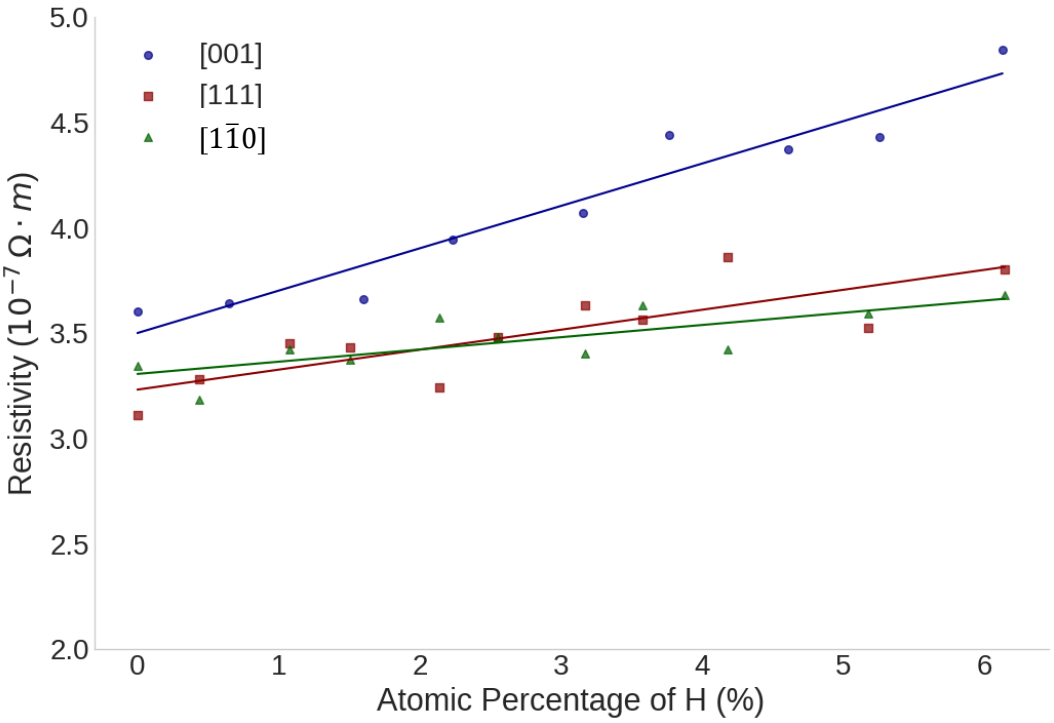

Figure 47 Variation in resistivity with H-concentration in all three crystallographic directions

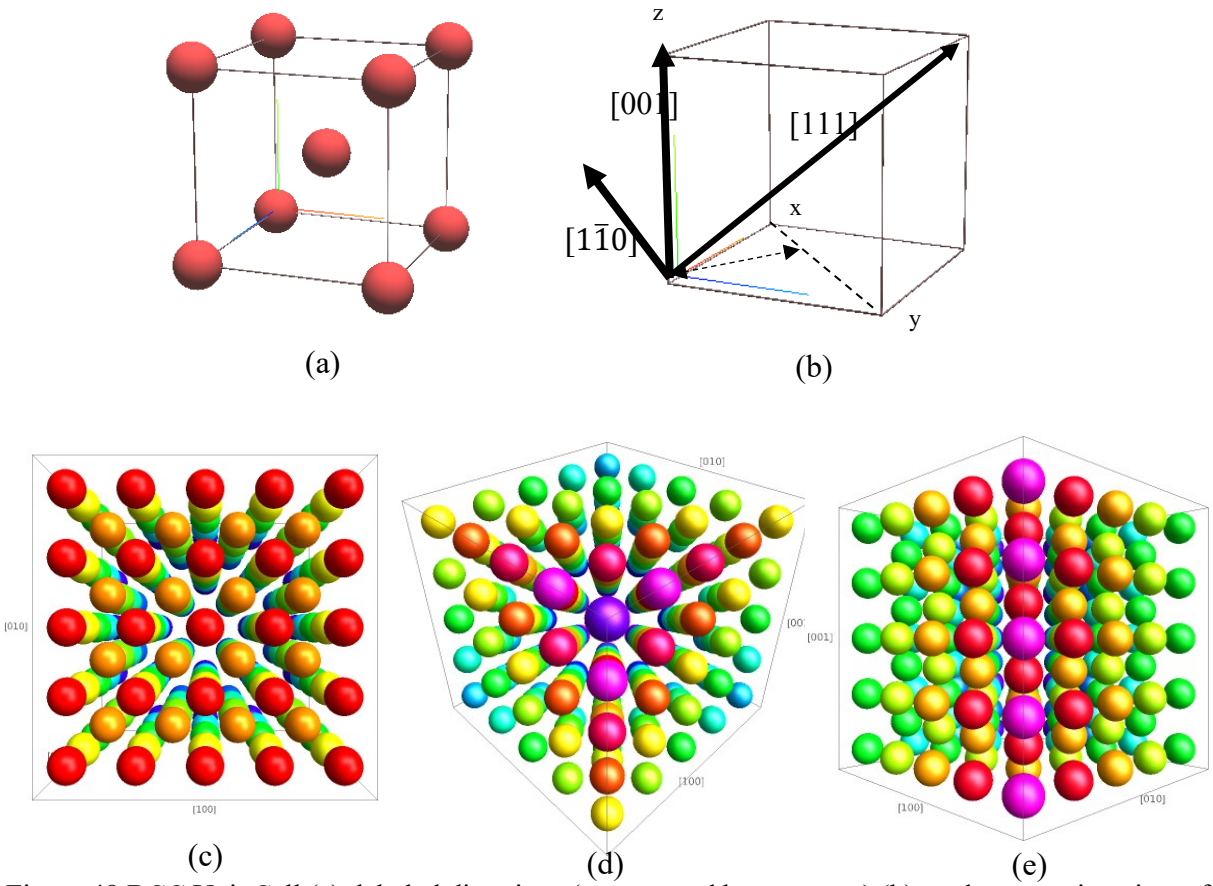

Figure 48 BCC Unit Cell (a), labeled directions (represented by an arrow) (b), and perspective view of the crystal when observed from directions: (c) [001] (d) [111] (e) [1$\bar{1}$0]

1.12 The Impact of Vacancies and Vacancy-Hydrogen Complexes on Fe Resistivity

The models with vacancy and VH-complexes in Fe system, detailed in methodology, are put through the same procedure entailed in Section 1.11. Having explored the impact of hydrogen addition to interstitial sites, the focus will now shift to examining the effects of defects, such as vacancies, and the ensuing influence of hydrogen presence within these defects. Figure 49 to Figure 51 represent the charge distribution, electron density and electron localization within the Fe model in the presence of a VH2 complex. As expected, the addition of the VH2 complex results in a non-uniform distribution of ELF, charge, and electron density, as compared to uniform distribution in pure Fe model shown in Section 1.11.2.

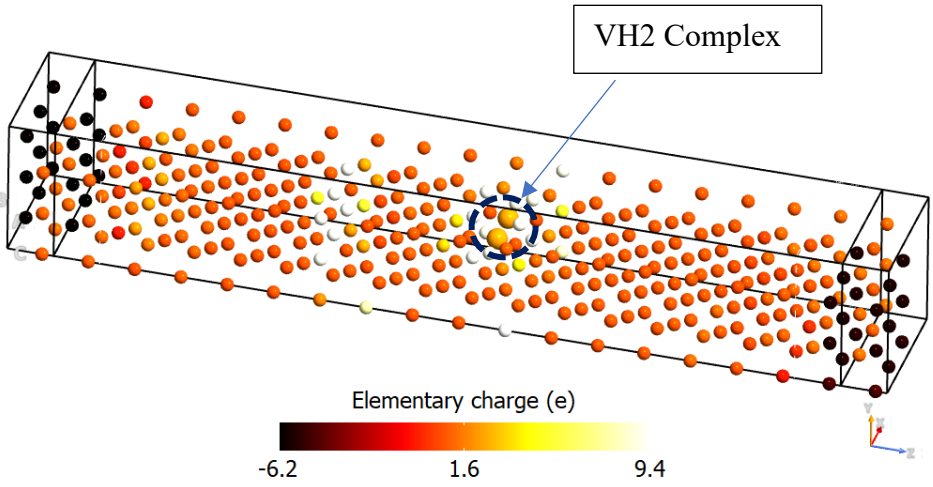

Figure 49 Charge distribution in Fe model with VH2 complex (H atoms are represented by bigger size for visual reference)

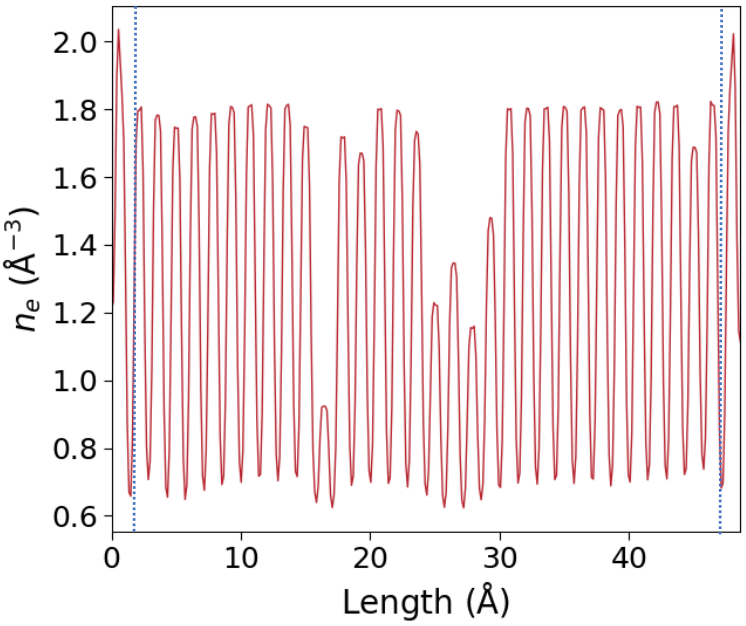

Figure 50 Electron density in the Fe model with VH2 complex

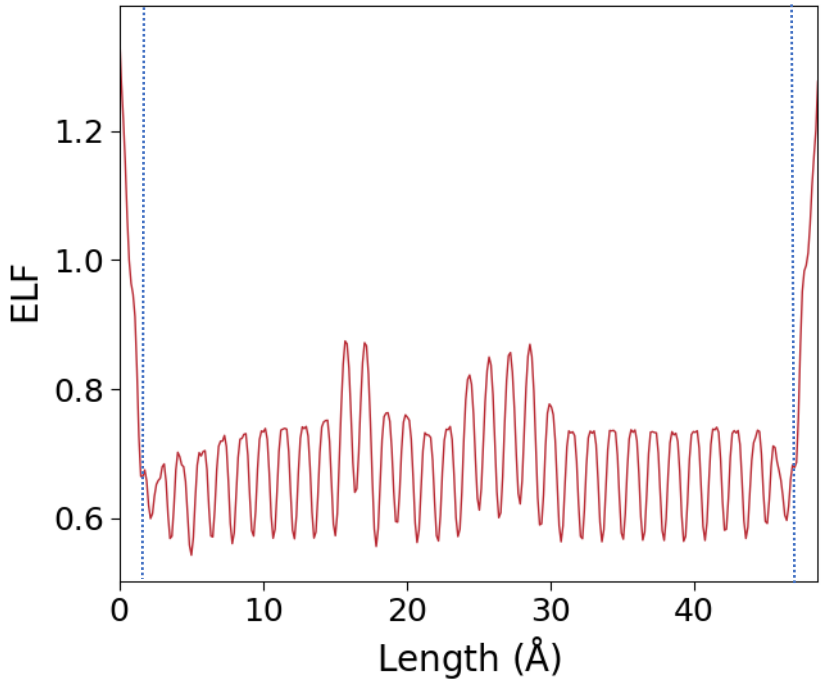

Figure 51 ELF in the Fe Model with VH2 complex

Electron localization can be further visualized on the plane/layer of atoms where VH2 complex is added in the model. Figure 52 shows the plane containing a VH2 complex. The regions around H atoms in the VH2 complex have a high localization of electrons and those regions show H atoms disrupting the electron clouds of the surrounding Fe atoms as well, which can be attributed to the electronegative nature of H. Similarly, Figure 53 shows the plane containing a VH3 complex in an Fe Model. It can be observed that a VH3 complex causes more localization and disruption in the spatial distribution of electrons as compared to the VH2 complex. Figure 54 shows the plane with a vacancy and it can be observed that the plane with just a vacancy has the least disruption in the spatial distribution of electrons as compared to the planes with VH2 and VH3 complex. From these observations, it can be predicted that the model with a vacancy should have the least resistivity and the model with a VH3 complex should have the highest resistivity.

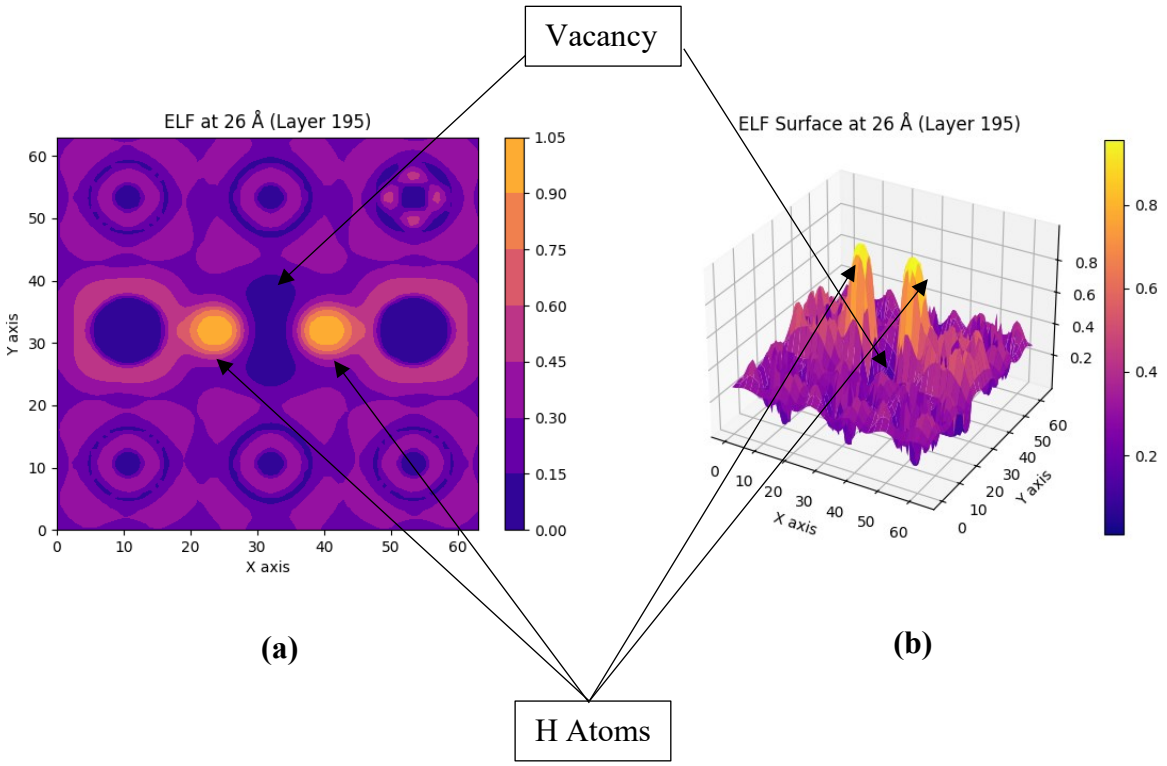

Figure 52 Electron localization heat map (a) and surface map (b) of the plane containing VH2 complex in Fe model

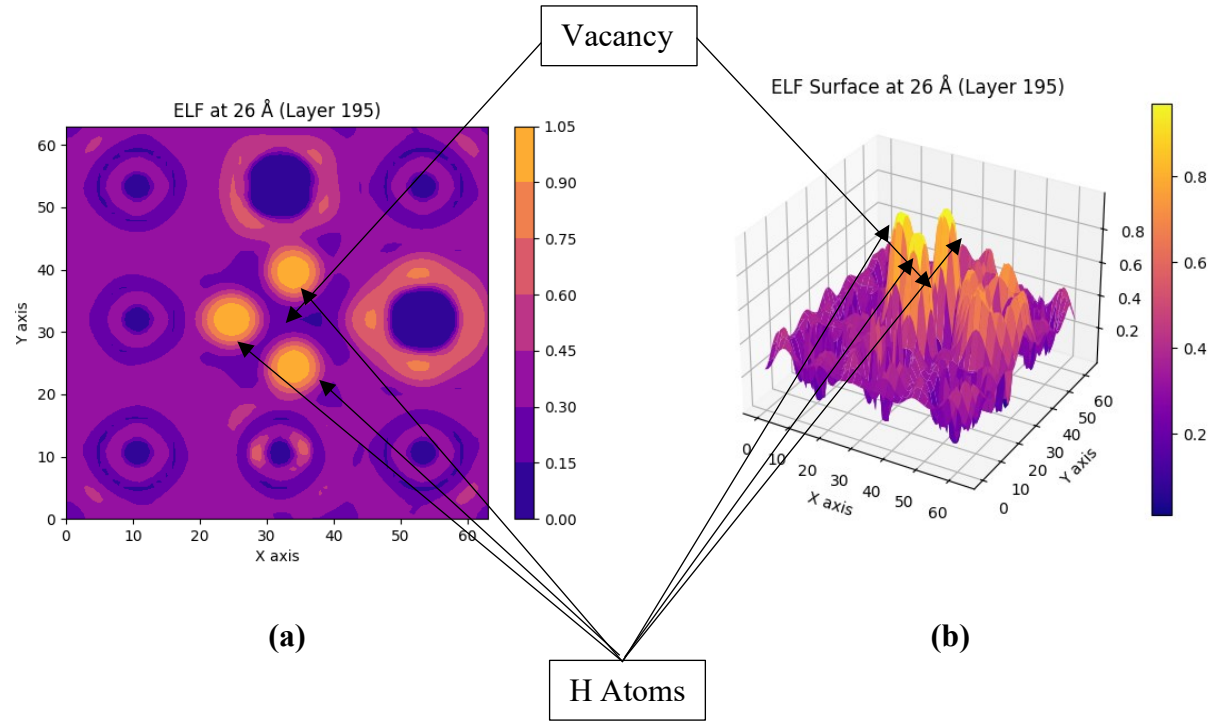

Figure 53 Electron localization heat map (a) and surface map (b) of the plane containing VH3 complex in Fe model

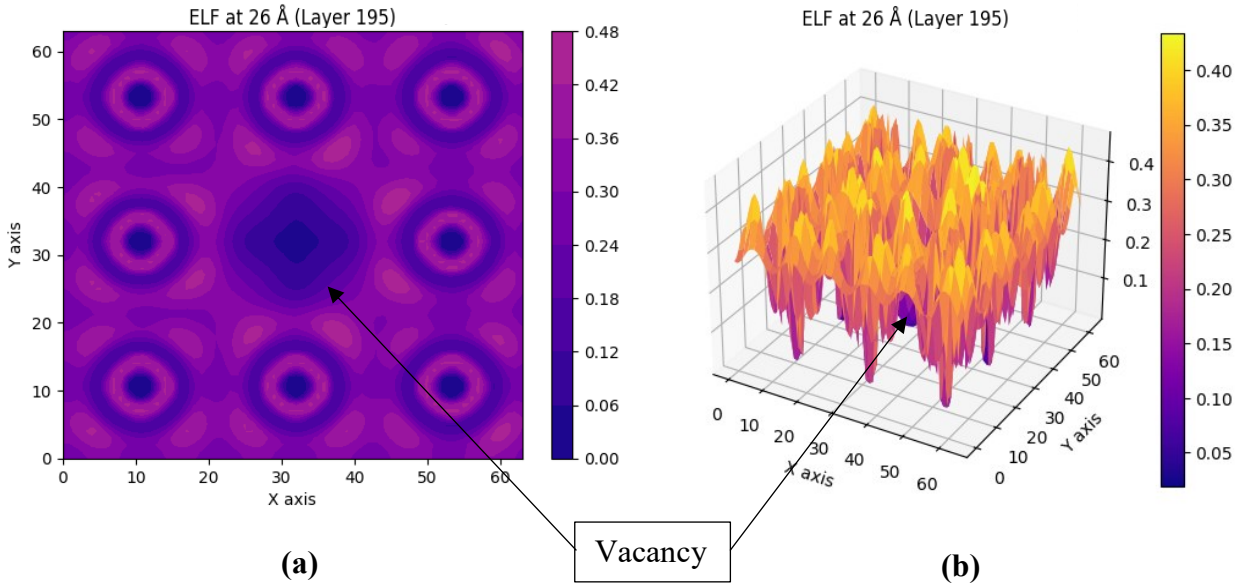

Figure 54 Electron localization heat map (a) and surface map (b) of the plane containing a vacancy in Fe model

As the vacancy-hydrogen interaction increased from a vacancy to VH2 and then to VH3 complex, an increase in resistivity was observed, as demonstrated in Figure 55 and Figure 56. This indicates that not only does the presence of vacancies affect the resistivity of the system, but this effect also intensifies as the VH complexes become larger, as predicted, highlighting the significant role played by lattice imperfections and impurities in dictating the electrical resistivity of the material.

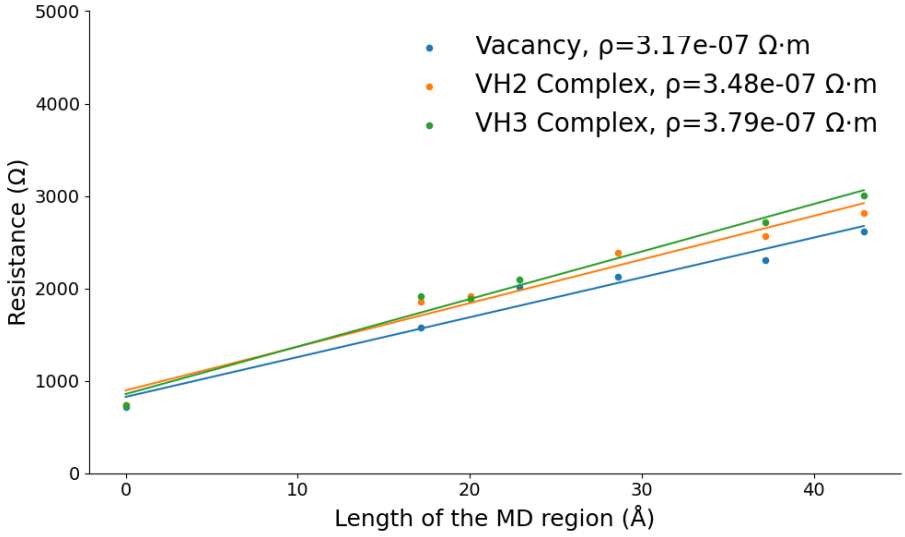

Figure 55 Resistance calculation at different MD-region lengths for resistivity calculation of VH configurations

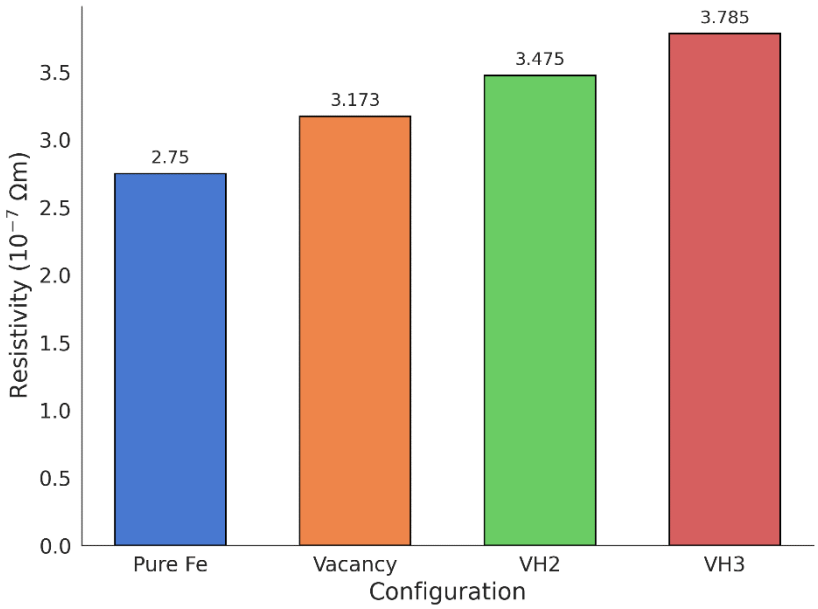

Figure 56 Resistivity of Fe-Model with different VH configurations

1.13 Effect of Grain Boundaries on Fe Resistivity in the Presence of Hydrogen

The effect of grain boundaries on the electrical resistivity of Fe is studied as a next step in studying the effects of defects on the electrical properties of Fe. The grain boundary models utilized for analysis have been detailed in the methodology section. As detailed before, three cases are explored: a model with grain boundary, a model with H atoms concentrated at the grain boundary, and a model with a grain boundary and H atoms dispersed on interstitial sites.

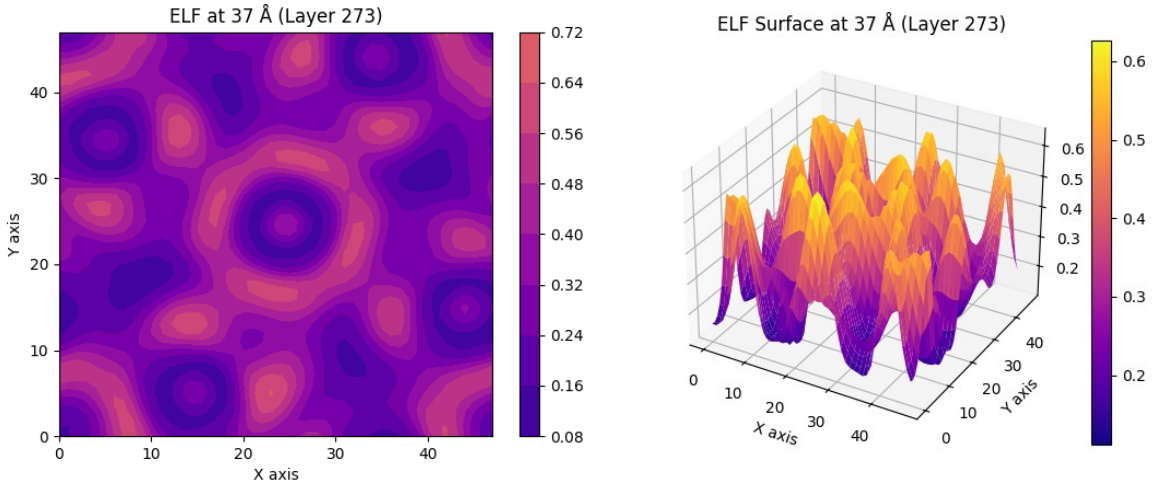

(a) **(b)**

Figure 57 Electron localization heat map (a) and surface map (b) of the plane containing a grain boundary in Fe model

Figure 57 and Figure 58 depict electron localization at 37 Å (measuring including left electrode) where grain boundary is located. The figures depict the plane of the grain boundary without H and with H concentrated at the boundary respectively. It is evident that the model without H atoms located at the grain boundary has relatively more uniform spatial electron distribution which means that there is less localization of electrons. On the other hand, the model with H atoms located at the grain boundary has abrupt and sharp localized and nonlocalized regions showing a higher degree of non-uniformity. From these results, it can be predicted that the model with H atoms concentrated at the grain boundary would have a higher resistivity (due to higher degree of localization and nonuniformity) than the model with just the grain boundary.

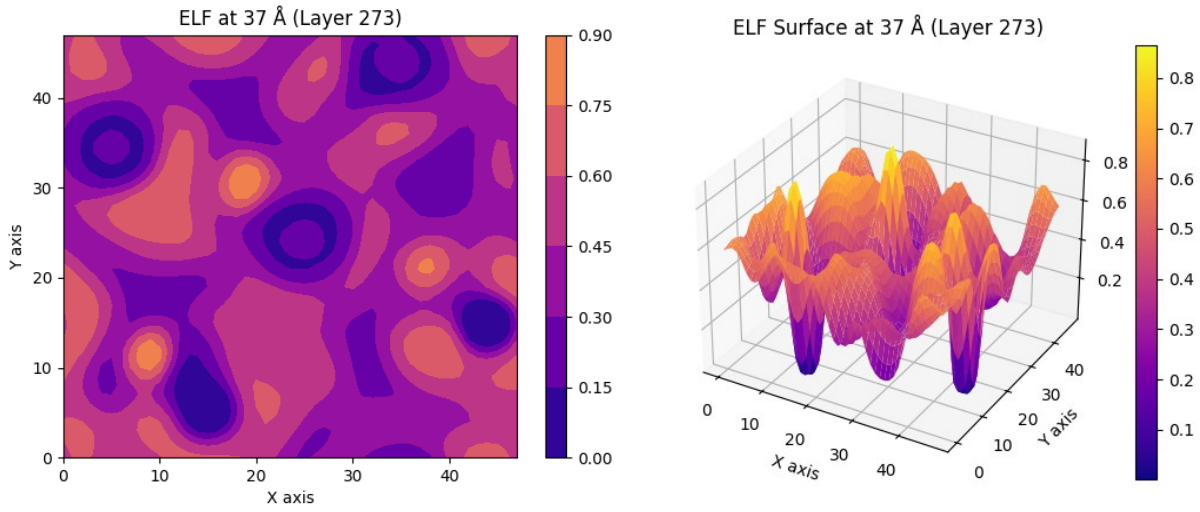

(a) **(b)**

Figure 58 Electron localization heat map (a) and surface map (b) of the plane with H- atoms concentrated at the grain boundary in Fe model

The last scenario with a grain boundary and H atoms dispersed on interstitial sites cannot be depicted on a single layer because the defects and impurities are located at different planes. Nonetheless, electron localization is non-uniform in this case as shown by a quantitative plot of ELF along the longitudinal direction of the model in Figure 60, which indicates that there will be a rise in the resistivity as compared to the pure Fe model. Whether this increase would be higher

than the first two grain boundary cases, has to be directly demonstrated through resistivity calculation, for it cannot be predicted. Figure 59 shows the ELF plot along the model length for the other two cases.

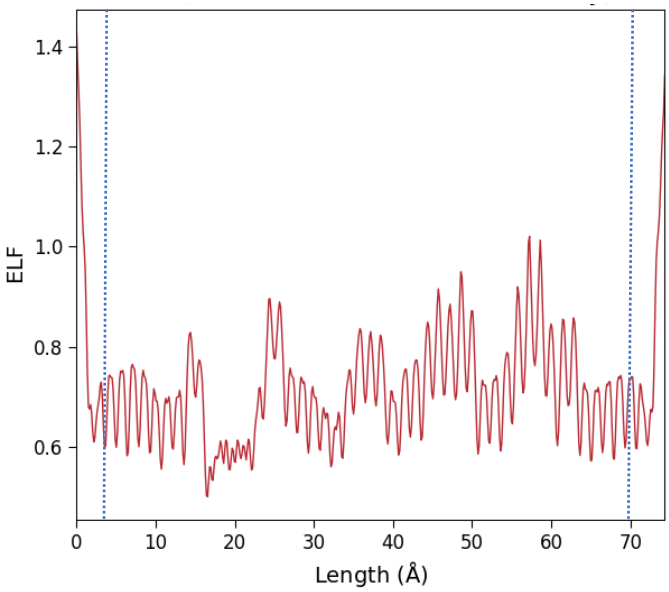

Figure 60 ELF for model with grain boundary and interstitial H

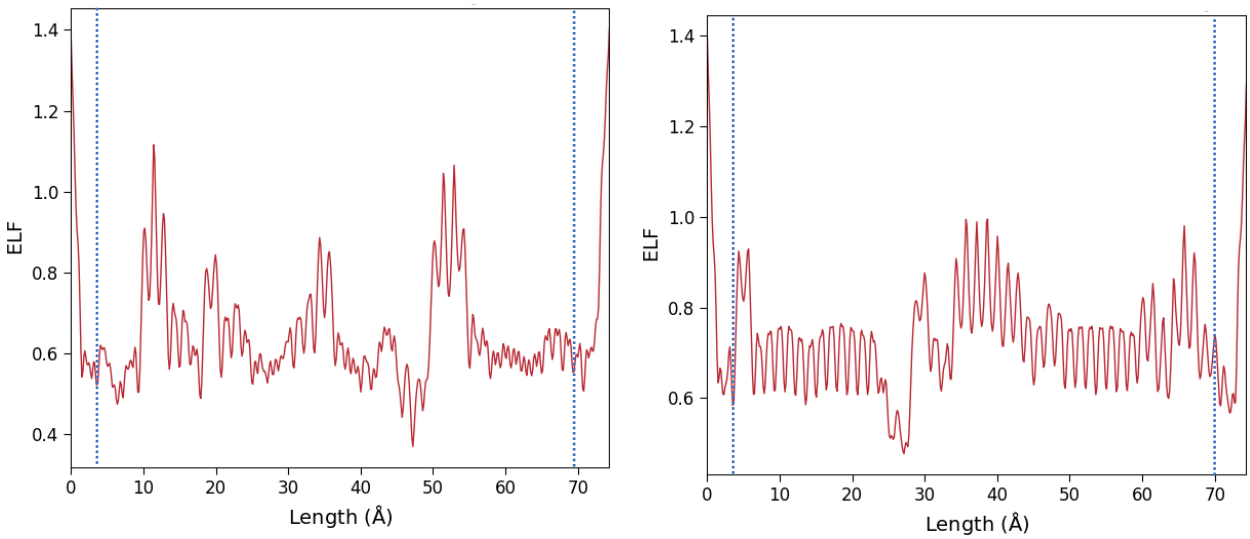

(a) **(b)**

Figure 59 ELF for model with grain boundary without H-atoms (a) and with H-atoms located at the grain boundary (b)

Overall, the results show that grain boundaries increase resistivity, which has been reported in the literature [63]. The resistivity results, as shown in Figure 61 and Figure 62, indicate that adding H

atoms increases the resistivity furthermore as predicted. The increase is substantial especially when H atoms are spread out on interstitial sites as compared to when they are concentrated at the grain boundary. It is critical to note that the resistivity for all these scenarios exceeds that of the pure Fe model, underscoring that defects such as grain boundaries and interstitial H contribute to increased resistivity. Figure 62 confirms this expectation. However, it is imperative to assess whether the trends observed in these three scenarios with a twist grain boundary would be similar with other grain boundary types. To address this, the analysis was repeated with a tilt grain boundary, as detailed in methodology. The values observed for the three scenarios for the tilt grain boundary model are marginally lower when compared to those in the twist grain boundary model, but the trends remain the same, as demonstrated in Figure 63. Therefore, it can be inferred that different types of grain boundary created in the model could lead to different resistivity values, but the pattern of increase in resistivity, with hydrogen located at the grain boundary and interstitial sites, would be similar among them.

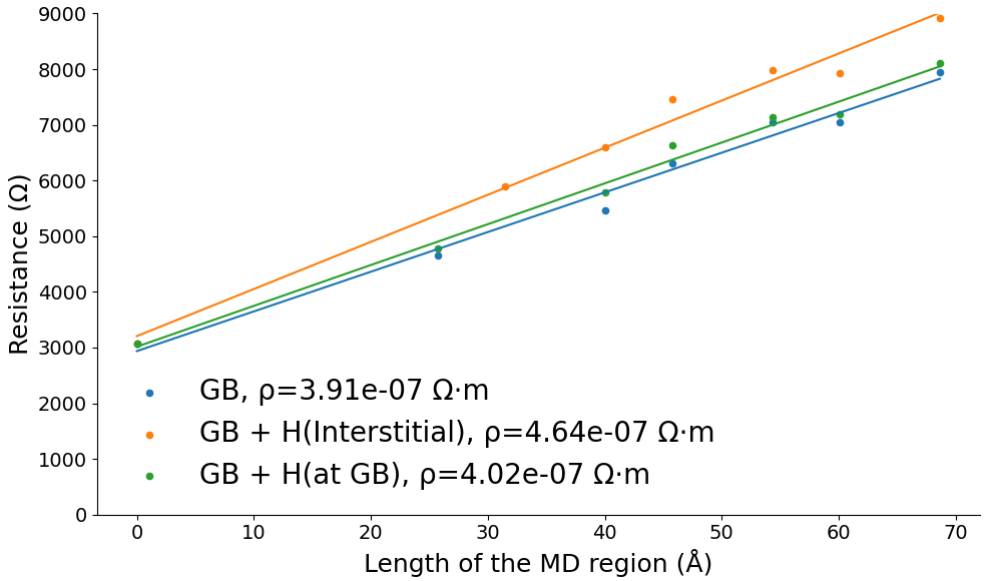

Figure 61 Resistance calculation at different lengths of MD-region for resistivity calculation in three cases of Σ5 [100]/[$\bar{1}$00] twist grain boundary

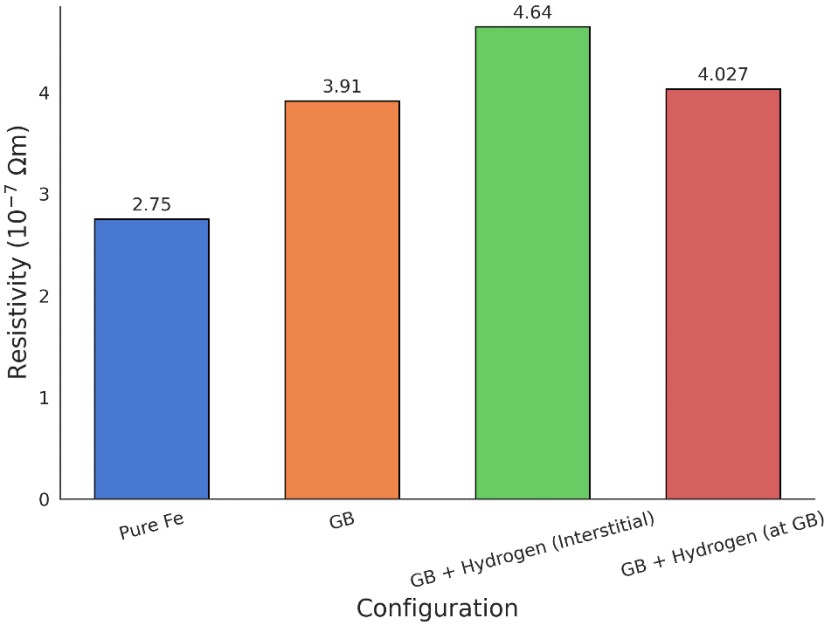

Figure 62 Resistivity for three grain boundary cases (Σ5 [100]/[$\bar{1}$00] twist grain boundary)

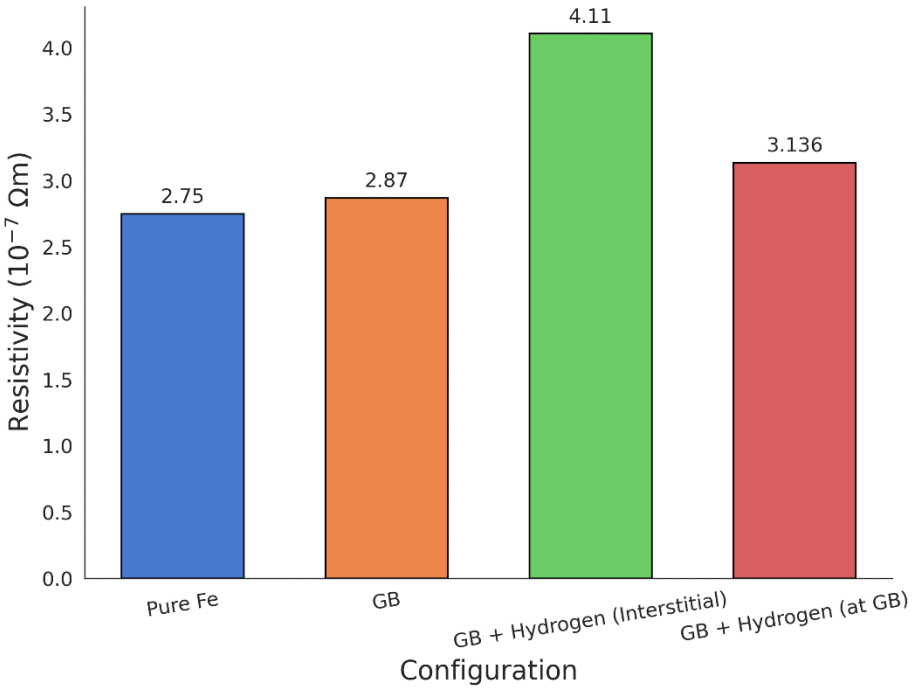

Figure 63 Resistivity for three grain boundary cases (Σ5 [001]/[$\bar{2}\bar{1}$0] symmetric tilt grain boundary)

Conclusion, Original Contributions, and Future Work

The motivation behind this research was rooted in the need to study the effects of hydrogen on the electrical properties of Fe and Fe-C systems. Such studies could pave the way for non-destructive detection of hydrogen-induced changes in Fe and Fe-C systems, which are used in various critical industrial applications and are susceptible to HE – a phenomenon leading to increased crack growth rate, reduced ductility, and potentially leading to catastrophic material failure. The key insights from this study are as follows:

- The addition of hydrogen has been shown to increase the electrical resistivity across Fe and Fe-C systems. This phenomenon is attributed to disruptions in electron flow, evidenced by alterations in the transmission spectrum, electron density, charge distribution, and Electron Localization Function (ELF) upon the introduction of hydrogen atoms in Fe-based systems, leading to a non-uniform spatial distribution of electrons.
- The spatial arrangement of hydrogen atoms within the material matrix influences electron transmission and resistivity. Determining the spatial arrangements of hydrogen atoms that cause a detectable change in these properties offers a step-forward towards non-destructive detection of hydrogen-induced changes.
- Localized DOS alterations near hydrogen incorporation sites were noted, but system-wide changes in the DOS at the Fermi level were minimal. The findings contribute towards the broader understanding that hydrogen impacts the resistivity of Fe and Fe-C system by causing a disruption in electron distribution rather than by altering the free electron count.
- The research has highlighted a direction-dependent (anisotropy) impact of hydrogen on resistivity. Specifically, the [001] direction exhibited the highest initial resistivity and the most significant increase with hydrogen concentration followed by direction [111] and

$[1\bar{1}0]$. This finding underscores the influence of crystallographic orientation on electron transport. This effect could be attributed to differences in interplanar distances and planar packing density.

- The introduction of vacancy-hydrogen (VH) complexes into the Fe matrix results in a non-uniform distribution of electron localization, charge, and electron density, with the complexity of the VH sub-structure correlating with the degree of disruption observed. This indicates that lattice imperfections and the presence of hydrogen within these defects significantly affect electrical resistivity of the material.
- The presence of grain boundaries, especially when associated with hydrogen atoms, either concentrated at the boundary or dispersed on interstitial sites, has been found to increase resistivity. The increase is substantial especially when H atoms are spread out on interstitial sites as compared to when they are concentrated at the grain boundary. This enhancement is consistent across different grain boundary types, although marginally varied, indicating the significance of hydrogen distribution around grain boundaries.

1.13.1.1 Original Contributions

The research provided in-depth insights into how interstitial hydrogen influences the resistivity—a key physical property—of Fe and Fe-C systems. A novel finding of this thesis is the detailed characterization of how interstitial hydrogen introduces non-uniformity in charge distribution, electron localization, and electron density. This non-uniformity disrupts electron transmission, significantly increasing resistivity through enhanced electron scattering events, a critical insight for understanding material behavior at the atomic level. Importantly, the thesis lays the groundwork for linking these detailed observations of non-uniformity and its effects on resistivity to the broader goal of developing non-destructive techniques for detecting hydrogen-induced

changes in Fe alloys. This research correlates specific changes in the physical properties (such as resistivity) and electron localization due to the presence of hydrogen. This encourages a future direction where DFT can be utilized to study how hydrogen affects the electronic structure of grain boundaries in steel, which could shed light on the changes in bond strength and elastic moduli that accompany hydrogen embrittlement. This approach could help interconnect disruptions in electron distribution, and changes in physical and mechanical properties with each other laying a foundation towards the development of a non-destructive techniques for mitigating HE.

These contributions significantly advance the understanding of the complex interactions between hydrogen and Fe and Fe-C systems. They serve as a foundation for future efforts aimed at enhancing the detection, analysis, and mitigation of HE, thereby improving the reliability and durability of these critical materials.

1.13.1.2 Future Work

Building upon the findings of this thesis, there are several exciting avenues for future research:

- Investigate different possibilities for the distribution and location of impurity atoms in the model and finding optimal locations/configurations. Moreover, multiple calculations for the same model, configuration, and hydrogen concentration can be performed several times to determine error margins, and error bars can be displayed for each resistance values on the resistivity plots.
- Extension to other metals and alloys: The MD-Landauer method could be extended to investigate HE in other metals and alloys, further broadening the understanding of this phenomenon in a variety of material systems.

- The influence of temperature and pressure on resistivity and HE could be a subject of future research. This would provide a more comprehensive view of the role these variables play in practical applications.
- Additional elements can be introduced to the Fe and Fe-C system to simulate steel-like structures, and the interaction of these elements with hydrogen can be studied. Furthermore, resistivity analysis can also be extended to systems created with Face-Centered Cubic (FCC) unit cells, which have different atomic arrangements than the BCC structure studied in this work. The distinct atomic arrangement in FCC unit cells may result in varied resistivity behavior in the presence of interstitial hydrogen.
- DFT can be utilized to study how hydrogen affects the electronic structure of grain boundaries in steel and Fe. This approach could shed light on hydrogen-induced embrittlement and the changes in bond strength and elastic moduli that accompany it.
- Apart from electrical resistivity, other physical properties such as magnetic properties and thermal conductivity could also be explored in the context of HE.

Following these research directions provides a deeper understanding of HE in Fe and steel, and potentially in a broader range of materials. This knowledge can lead to the development of more effective HE mitigation strategies and advanced material designs.

References

[1] W. D. Callister and D. G. Rethwisch, 'Materials science and engineering: An introduction', 10th ed., Wiley, 2018, pp. 200–324.

[2] H. K. D. H. Bhadeshia and R. W. K. Honeycombe, 'Steels: Microstructure and properties', 3rd ed., Elsevier, 2006, pp. 320–344.

[3] D. E. Jiang and E. A. Carter, 'Diffusion of interstitial hydrogen into and through bcc Fe from first principles', *Physical Review B - Condensed Matter and Materials Physics*, vol. 70, no. 6, p. 064102, 2004.

[4] H. K. Birnbaum and P. Sofronis, 'Hydrogen-enhanced localized plasticity—a mechanism for hydrogen-related fracture', *Materials Science and Engineering: A*, vol. 176, no. 1–2, pp. 191–202, 1994.

[5] S. Lynch, 'Hydrogen embrittlement phenomena and mechanisms', *Corrosion Reviews*, vol. 30, no. 3–4, pp. 105–123, 2012.

[6] W. Kohn and L. J. Sham, 'Self-consistent equations including exchange and correlation effects', *Physical Review*, vol. 140, no. 4A, p. A1133, 1965.

[7] P. Hohenberg and W. Kohn, 'Inhomogeneous electron gas', *Physical Review*, vol. 136, no. 3B, p. B864, 1964.

[8] R. A. Oriani, 'The diffusion and trapping of hydrogen in steel', *Acta Metallurgica*, vol. 18, no. 1, pp. 147–157, 1970.

[9] I. M. Robertson, P. Sofronis, A. Nagao, M. L. Martin, S. Wang, W. D. Gross, and K. E. Nygren, 'Hydrogen embrittlement understood', *Metallurgical and Materials Transactions A 2015 46:6*, vol. 46, no. 6, pp. 2323–2341, 2015.

[10] S. M. Teus and V. G. Gavriljuk, 'Molecular dynamics study of the hydrogen and carbon effect on mobility of grain boundaries in α-Iron', *Metallophysics and Advanced Technologies*, vol. 41, no. 9, pp. 1187–1203, 2019.

[11] S. Datta, 'The non-equilibrium Green's function (NEGF) formalism: An elementary introduction', *International Electron Devices Meeting*, pp. 703–706, 2002.

[12] T. Markussen, M. Palsgaard, D. Stradi, T. Gunst, M. Brandbyge, and K. Stokbro, 'Electron-phonon scattering from Green's function transport combined with molecular dynamics: Applications to mobility predictions', *Physical Review B*, vol. 95, no. 24, p. 245210, 2017.

[13] N. Sule and I. Knezevic, 'Phonon-limited electron mobility in graphene calculated using tight-binding Bloch waves', *Journal of Applied Physics*, vol. 112, no. 5, p. 53702, 2012.

[14] A. S. Kholtobina, R. Pippan, L. Romaner, D. Scheiber, W. Ecker, and V. I. Razumovskiy, 'Hydrogen trapping in bcc Iron', *Materials*, vol. 13, no. 10, 2020.

[15] C. Wang, L. Cheng, X. Sun, X. Zhang, J. Liu, and K. Wu, 'First-principle study on the effects of hydrogen in combination with alloy solutes on local mechanical properties of steels', *International Journal of Hydrogen Energy*, vol. 47, no. 52, pp. 22243–22260, 2022.

[16] H. Zhou, C. Xu, Q. Wang, H. Pan, and J. Chen, 'Characterization of hydrogen embrittlement in 2.25Cr-1Mo-0.25V steel by eddy current method', *Research in Nondestructive Evaluation*, vol. 29, no. 4, pp. 212–220, 2017.

[17] K. Koenig, A. N. Lasseigne, J. W. Cisler, B. Mishra, R. H. King, and D. L. Olson, 'Non-contact, nondestructive hydrogen and microstructural assessment of steel welds', *International Journal of Pressure Vessels and Piping*, vol. 87, no. 11, pp. 605–610, 2010.

[18] I. H. Katzarov, D. L. Pashov, and A. T. Paxton, 'Hydrogen embrittlement I. Analysis of hydrogen-enhanced localized plasticity: Effect of hydrogen on the velocity of screw dislocations in α -Fe', *Physical Review Materials*, vol. 1, no. 3, p. 033602, 2017.

[19] L. Vandewalle, M. J. Konstantinović, T. Depover, and K. Verbeken, 'The potential of the internal friction technique to evaluate the role of vacancies and dislocations in the hydrogen embrittlement of steels', *steel research international*, vol. 92, no. 6, p. 2100037, 2021.

[20] S. Liang, M. Huang, L. Zhao, Y. Zhu, and Z. Li, 'Effect of multiple hydrogen embrittlement mechanisms on crack propagation behavior of FCC metals: Competition vs. synergy', *International Journal of Plasticity*, vol. 143, p. 103023, 2021.

[21] D. Di Stefano, M. Mrovec, and C. Elsässer, 'First-principles investigation of hydrogen trapping and diffusion at grain boundaries in nickel', *Acta Materialia*, vol. 98, pp. 306–312, 2015.

[22] P. Kumar, P. Garg, K. N. Solanki, and I. Adlakha, 'Effect of hydrogen on the ideal shear strength in metals and its implications on plasticity: A first-principles study', *International Journal of Hydrogen Energy*, vol. 46, no. 50, pp. 25726–25737, 2021.

[23] J. Bellemare, D. Ménard, and F. Sirois, 'Detection of hydrogen embrittlement in plated high-strength steels with eddy currents: Is the sensitivity sufficient?', *Journal of Nondestructive Evaluation*, vol. 39, no. 2, pp. 1–15, 2020.

[24] P. Drude, ‘Zur elektronentheorie der metalle’, *Annalen der Physik*, vol. 306, no. 3, pp. 566–613, 1900.

[25] C. Kittel, ‘Introduction to solid state physics’, 8th ed., New York: Wiley, 2005, pp. 500–598.

[26] J. M. Ziman, ‘Principles of the theory of solids’, 2nd ed., Cambridge, UK: Cambridge University Press, 1972, pp. 223–312.

[27] N. W. Ashcroft and N. D. Mermin, ‘Solid state physics’, 1st ed., Holt, Rinehart and Winston, 1976, pp. 734–800.

[28] R. E. Peierls, ‘Quantum theory of solids.’, 1st ed., Oxford, UK: Oxford University Press, 2001, pp. 156–193.

[29] M. Tinkham, ‘Introduction to superconductivity’, 2nd ed., New York: Courier Dover Publications, 2004, pp. 230–380.

[30] P. W. Anderson, ‘Concepts in solids: Lectures on the theory of solids’, 1st ed., Singapore: World Scientific, 1997, pp. 133–156.

[31] J. Singleton, ‘Band theory and electronic properties of solids’, 1st ed., Oxford, UK: Oxford University Press, 2001, pp. 157–158.

[32] S. Datta, ‘Electronic transport in mesoscopic systems’, 1st ed., Cambridge, UK: Cambridge University Press, 1995, pp. 125–167.

[33] D. S. Sholl and J. A. Steckel, ‘Density functional theory: A practical introduction’, 1st ed., Hoboken, NJ, USA: Wiley, 2015, pp. 201–210.

[34] N. Zettili, ‘Quantum mechanics: Concepts and applications’, 2nd ed., Chichester, U.K.: Wiley, 2009, pp. 211–363.

[35] R. G. Parr and Weitao. Yang, ‘Density-functional theory of atoms and molecules’, Revised ed., Oxford, UK: Oxford University Press, 1989, pp. 320–333.

[36] J. J. Sakurai and J. Napolitano, ‘Modern Quantum Mechanics’, 2nd ed., Cambridge, UK: Cambridge University Press, 2017, pp. 313–456.

[37] R. M. Martin, ‘Electronic structure: Basic theory and practical methods’, 1st ed., Cambridge, UK: Cambridge University Press, 2004, pp. 267–341.

[38] B. Aradi, B. Hourahine, and T. Frauenheim, ‘DFTB+, a sparse matrix-based implementation of the DFTB method’, *Journal of Physical Chemistry A*, vol. 111, no. 26, pp. 5678–5684, 2007.

[39] M. Elstner, D. Porezag, G. Jungnickel, J. Elsner, M. Haugk, and T. Frauenheim, ‘Self-consistent-charge density-functional tight-binding method for simulations of complex materials properties’, *Physical Review B*, vol. 58, no. 11, p. 7260, 1998.

[40] M. Pourfath, ‘The non-equilibrium green’s function method for nanoscale device simulation’, 1st ed., in Computational Microelectronics. , Vienna, Austria: Springer , 2014, pp. 121–234.

[41] S. Smidstrup *et al.*, ‘QuantumATK: an integrated platform of electronic and atomic-scale modelling tools’, *Journal of Physics: Condensed Matter*, vol. 32, no. 1, p. 015901, 2019.

[42] F. Giustino, ‘Electron-phonon interactions from first principles’, *Reviews of Modern Physics*, vol. 89, no. 1, p. 015003, 2017.

[43] L. Chico, L. X. Benedict, S. G. Louie, and M. L. Cohen, ‘Quantum conductance of carbon nanotubes with defects’, *Physical Review B*, vol. 54, no. 4, p. 2600, 1996.

[44] K. H. Bevan, ‘First principles non-equilibrium green’s function modeling of vacuum and oxide barrier’, Ph.D. dissertation, Purdue University, West Lafayette, IN, USA, 2008.

[45] J. Taylor, H. Guo, and J. Wang, ‘Ab initio modeling of quantum transport properties of molecular electronic devices’, *Physical Review B*, vol. 63, 2000.

[46] Y. Ke, F. Zahid, V. Timoshevskii, K. Xia, D. Gall, and H. Guo, ‘Resistivity of thin Cu films with surface roughness’, *Physical Review B - Condensed Matter and Materials Physics*, vol. 79, no. 15, p. 155406, 2009.

[47] F. Zahid, Y. Ke, D. Gall, and H. Guo, ‘Resistivity of thin Cu films coated with Ta, Ti, Ru, Al, and Pd barrier layers from first principles’, *Physical Review B - Condensed Matter and Materials Physics*, vol. 81, no. 4, p. 045406, 2010.

[48] V. G. Gavriljuk, V. M. Shyvaniuk, and S. M. Teus, ‘Hydrogen in engineering metallic materials’, 1st ed., Springer Nature, 2022, pp. 15–111.

[49] S. M. Teus and V. G. Gavriljuk, ‘On a correlation between hydrogen effects on atomic interactions and mobility of grain boundaries in the alpha-iron. Stage II: Mobility of grain boundaries in the H-charged α-iron’, *Materials Letters*, vol. 259, p. 126859, 2020.

[50] V. G. Gavriljuk, V. N. Shyvaniuk, and S. M. Teus, ‘Mobility of dislocations in the iron-based C-, N-, H-solid solutions measured using internal friction: Effect of electron structure’, *Journal of Alloys and Compounds*, vol. 886, p. 161260, 2021.

[51] V. G. Gavriljuk, ‘Influence of interstitial carbon, nitrogen, and hydrogen on the plasticity and brittleness of steel’, *Steel in Translation 2015*, vol. 45, no. 10, pp. 747–753, 2016.

[52] S. M. Teus and V. G. Gavriljuk, ‘On a correlation between the hydrogen effects on atomic interactions and mobility of grain boundaries in the alpha-iron. Stage I: A change in the electron structure of the alpha-iron due to hydrogen’, *Materials Letters*, vol. 258, p. 126801, 2020.

[53] S. M. Teus, V. F. Mazanko, J. M. Olive, and V. G. Gavriljuk, 'Grain boundary migration of substitutional and interstitial atoms in α-iron', *Acta Materialia*, vol. 69, pp. 105–113, 2014.

[54] S. M. Teus and V. G. Gavriljuk, 'Grain-boundary diffusion of hydrogen atoms in the α-Iron', *Metallofizika Noveishie Tekhnologii*, vol. 36, no. 10, pp. 1399–1410, 2014.

[55] V. G. Gavriljuk, S. M. Teus, B. D. Shanina, and A. A. Konchits, 'On the nature of similarity in embrittlement of metals by hydrogen and surfactants', *Material Science & Engineering International Journal*, vol. 1, no. 3, pp. 70-79, 2017.

[56] V. G. Gavriljuk and G V Kurdyumov, 'Carbon, Nitrogen and Hydrogen in Iron-Based Solid Solutions: Similarities and Differences in their Effect on Structure and Properties', *Metallofiz. Noveishie Tekhnol*, vol. 38, no. 1, pp. 67–98, 2016.

[57] D. J. Van Ooijen and J. D. Fast, 'Electrical resistance of hydrogen-charged iron wires', *Acta Metallurgica*, vol. 11, no. 3, pp. 211–216, 1963.

[58] D. A. Mirzaev, A. A. Mirzoev, K. Y. Okishev, and A. V. Verkhovykh, 'Hydrogen–vacancy interaction in bcc iron: ab initio calculations and thermodynamics', *Molecular Physics*, vol. 112, no. 13, pp. 1745–1754, 2013.

[59] K. Ohsawa, K. Eguchi, H. Watanabe, M. Yamaguchi, and M. Yagi, 'Configuration and binding energy of multiple hydrogen atoms trapped in monovacancy in bcc transition metals', *Physical Review B*, vol. 85, no. 9, p. 094102, 2012.

[60] A. Ramasubramaniam, M. Itakura, and E. A. Carter, 'Interatomic potentials for hydrogen in α -iron based on density functional theory', *Physical Review B*, vol. 79, no. 17, p. 174101, May 2009.

[61] Y. Tateyama and T. Ohno, 'Stability and clusterization of hydrogen-vacancy complexes in-Fe: An ab initio study', *Phys. Rev. B*, vol. 67, no. 17, p. 174105, 2003.

[62] F. Besenbacher, S. M. Myers, P. Nordlander, and J. K. Nørskov, 'Multiple hydrogen occupancy of vacancies in Fe', *Journal of Applied Physics*, vol. 61, no. 5, p. 1788, 1998.

[63] H. Bishara, S. Lee, T. Brink, M. Ghidelli, and G. Dehm, 'Understanding grain boundary electrical resistivity in Cu: The effect of boundary structure', *ACS Nano*, vol. 15, no. 10, pp. 16607–16615, 2021.

[64] M. Zidane, E. M. Salmani, A. Majumdar, H. Ez-Zahraouy, A. Benyoussef, and R. Ahuja, 'Electrical and thermal transport properties of Fe–Ni based ternary alloys in the earth's inner core: An ab initio study', *Physics of the Earth and Planetary Interiors*, vol. 301, p. 106465, 2020.

[65] H. Gomi and K. Hirose, 'Electrical resistivity and thermal conductivity of hcp Fe–Ni alloys under high pressure: Implications for thermal convection in the Earth's core', *Physics of the Earth and Planetary Interiors*, vol. 247, pp. 2–10, 2015.

[66] M. Pozzo, C. Davies, D. Gubbins, and D. Alfè, 'Transport properties for liquid silicon-oxygen-iron mixtures at Earth's core conditions', *Physical Review B*, vol. 87, no. 1, p. 014110, 2013.

[67] D. Stradi, U. Martinez, A. Blom, M. Brandbyge, and K. Stokbro, 'General atomistic approach for modeling metal-semiconductor interfaces using density functional theory and nonequilibrium Green's function', *Physical Review B*, vol. 93, no. 15, p. 155302, 2016.

[68] 'Iron, Fe material properties', MatWeb. [Online]. Available: https://www.matweb.com/search/DataSheet.aspx?MatGUID=654ca9c358264b5392d43315d8535b7d

[69] ‘AISI 4340 steel, normalized, material properties’, MatWeb. [Online]. Available: https://www.matweb.com/search/DataSheet.aspx?MatGUID=fd2df45bffa54018b54989bc14092d9f&ckck=1

[70] ‘AISI 1018 steel, cold drawn’, MatWeb. [Online]. Available: https://www.matweb.com/search/DataSheet.aspx?MatGUID=3a9cc570fbb24d119f08db22a53e2421&ckck=1

[71] K. Fukuda, A. Tojo, and R. Matsumoto, ‘Evaluating solubility and diffusion coefficient of hydrogen in martensitic steel using computational mechanics’, *Zairyo/Journal of the Society of Materials Science, Japan*, vol. 69, no. 2, pp. 134–140, 2020.

[72] M. Smialowski, ‘Hydrogen in steel: Effect of hydrogen on iron and steel during production, fabrication, and use’, 1st ed., Pergamon Press, 1962, pp. 273–387.

[73] G. Gottstein, ‘Physical foundations of materials science’, Springer Berlin Heidelberg, 2004, pp. 413–502.

[74] S. M. Kim and W. J. L. Buyers, ‘Vacancy formation energy in iron by positron annihilation’, *Journal of Physics F: Metal Physics*, vol. 8, no. 5, p. L103, May 1978.

[75] R. Soto, ‘Kinetic Theory and Transport Phenomena’, 1st ed., Oxford University Press, 2016, pp. 169–198.

[76] P. L. Rossiter, ‘The electrical resistivity of metals and alloys’, Revised ed., Cambridge, UK: Cambridge University Press, 1987, pp. 324–412.

[77] A. Savin, R. Nesper, S. Wengert, and T. F. Fässler, ‘ELF: The electron localization function’, *Angewandte Chemie International Edition*, vol. 36, no. 17, pp. 1808–1832, 1997.

[78] S. S. Sidhu, ‘The structure of cubic crystals as revealed by X-rays’, *American Journal of Physics*, vol. 16, no. 4, pp. 199–205, 1948.

[79] P. Błoński and A. Kiejna, ‘Structural, electronic, and magnetic properties of bcc iron surfaces’, *Surface Science*, vol. 601, no. 1, pp. 123–133, 2007.

[80] W. Zhang, ‘Evaluation of susceptibility to hydrogen embrittlement—A rising step load testing method’, *Materials Sciences and Applications*, vol. 07, no. 08, pp. 389–395, 2016.

Appendix

This section goes into the details of resistivity calculation and the step-by-step procedure highlighting the significance of resistance at an MD-region length (L) = 0:

- The value of conductance is obtained from simulations at one length of the MD-region, and the value of resistance is the reciprocal of the conductance.
- This process is repeated for different MD-region lengths. Resistance values are obtained at different lengths.
- Resistance (y-axis) and Length (x-axis) are plotted on a graph, as shown in Figure 10.
- A linear curve fitting is performed on the values to get an equation (y=mx+c) where m is the slope and c is the y intercept. If this is translated to our case where R is the y-axis and L is the x-axis we get: $R=mL+R_0$.
- Here R_0 is the resistance when there are no atoms in the MD region. This is the resistance introduced by interface/junction between different parts or phases of the device (in this case: Left electrode to MD-region and then MD-region to right electrode).
- Slope (m) is the resistivity per unit cross-section area.
- Therefore, the linear equation applied to this specific case becomes:

$$R = R_0 + R_{Bulk} = R_0 + \rho \frac{L}{A}$$

  - R = total resistance at a certain length
  - R_{Bulk} = Resistance due to intrinsic properties of the MD-region, and depends on the length of the material.
  - R_0 = Resistance encountered at the interfaces between the material under study and the electrodes. It is independent of the length of the material because it arises

from the properties of the contact interface between MD-region and electrodes themselves.

- At any length, when a value of resistance is calculated, that value obtained also contains the effects of R_0, since electrode contacts are always there in the device. Thus, the values obtained at a certain length from the simulations are R not $R_{bulk.}$
- The goal here is to obtain the resistivity. Including the L= 0 point (or accounting for contact resistance in the curve fitting) is crucial for accurately determining the intrinsic resistivity of the material. If the study were to exclude the contact resistance, the calculated resistivity would be inaccurate, as it would assume that all measured resistance is due to the bulk material, ignoring the contribution from the contacts. Therefore, the equation provides a complete picture while calculating the resistivity by accounting for contact resistance: $(R-R_0) *A/L = \rho$
- This method provides a more complete picture of the material's electrical properties, separating the effects of the contacts from those of the material itself.

The approach involves conducting simulations across various lengths, starting from 0 Å up to a predetermined length X, to observe how the calculated resistivity changes with the length of the material. This methodology is grounded in the principle that resistivity (ρ) should theoretically remain constant for a homogeneous material, irrespective of its length. However, variations can occur due to the presence of contact resistance and potential simulation inaccuracies arising from limitations of the solvers and DFT and MD. The question is what should be the value of X in the 0 to X Å range since the larger the X, the more computational power and time it requires to compute. We do not want to make the model unnecessarily large and inconvenient to compute. On the other hand, smaller values of X can lead to inaccurate slope and resistivity values due to

inherent limitations of solvers and simulation methods. Therefore, an optimal value of X is determined based on the convergence method summarized below.

In Figure 11, simulations are initiated at lengths ranging from 0 Å, explicitly including the contact resistance, and extended up to various upper limits (e.g., 20, 23, 29, 37, 43, 51, 57, 66, 71, 80 Å). For each range (0 to X Å), the slope of the resistance vs. length plot is calculated, providing the resistivity value and that value represents each dot on the resistivity graph such as in Figure 34. Initially, variations in the calculated resistivity values are observed, which could be attributed to simulation errors, inherent inaccuracies in the model, or the physical phenomena being modeled. As the length range is extended and resistivity recalculated, it is observed that beyond a certain point (e.g., 43 Å), the resistivity values start to converge. The methodology for determining the optimal length range for resistivity calculations ensures the inclusion of crucial physical phenomena (like contact resistance) and leverages the concept of convergence to identify a range that provides accurate and reliable resistivity values.

The convergence around 43 Å suggests that extending the length beyond X (in the 0 to X range) provides little to no additional accuracy in the resistivity calculation, and it would add computational load for the subsequent calculations (since this study has many calculations like these, the computational load would be tremendous). This point is chosen as the optimal length range because it includes the necessary calculations for contact resistance (at very short lengths) while minimizing the impact of simulation inaccuracies and the diminishing returns of extending the length further.

It could be argued that the analysis should initiate from 43 Å onwards. Initiating the analysis from a length of 43 Å to 80 Å, for example, necessitates extrapolating these values backward to determine a y-intercept, which represents the contact resistance. Relying on extrapolation for this

critical value introduces a risk of significant inaccuracies. Such inaccuracies are particularly pronounced if the data from 43 to 80 Å contains inherent simulation limitations or anomalies, which can skew the extrapolated y-intercept away from its accurate value. As shown in the Figure A and B below, the simulated y-intercept and the extrapolated y-intercept values are considerably different. The cornerstone of this study is the calculation of resistance values, including the y-intercept/contact resistance, through direct simulations rather than relying on estimations or extrapolations. By including the range from 0 to 43 Å, the study ensures that all data points, especially the y-intercept, are derived from calculated results. This approach eliminates the need to make assumptions about the y-intercept and the overall trend line's direction based solely on data from 43 Å onwards. Consequently, it provides a more accurate and reliable foundation for determining the material's resistivity, ensuring that the study's findings are grounded in direct calculation rather than inferred characteristics. Moreover, Figure C shows the plot with all the simulated values in 0 to 80 Å range. It depicts that there is no advantage going up to such a high range since the resistivity values obtained in 0 to X Å range after X=43 Å are considerably close to one another and it adds unnecessary and time-consuming computational load.

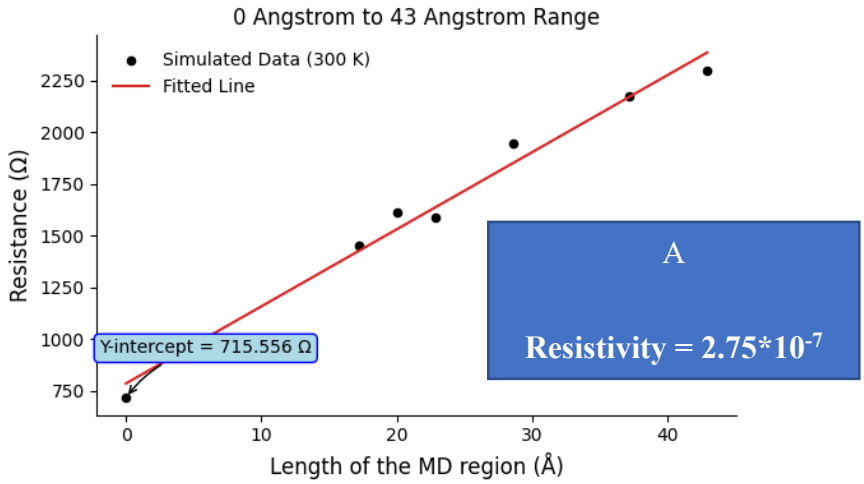
0 Angstrom to 43 Angstrom Range
Simulated Data (300 K)
Fitted Line
Resistance (Ω)
Length of the MD region (Å)
Y-intercept = 715.556 Ω
A
Resistivity = 2.75*10-7

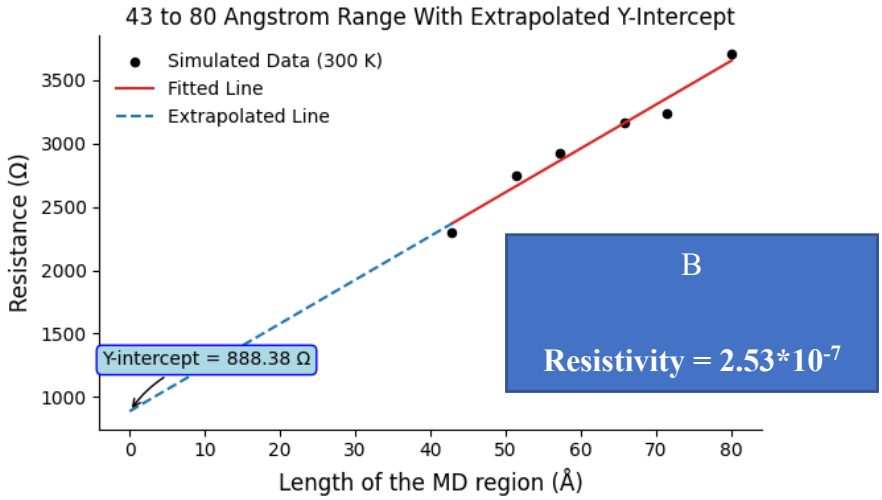
43 to 80 Angstrom Range With Extrapolated Y-Intercept
Simulated Data (300 K)
Fitted Line
Extrapolated Line
Resistance (Ω)
Length of the MD region (Å)
Y-intercept = 888.38 Ω
B
Resistivity = 2.53*10-7

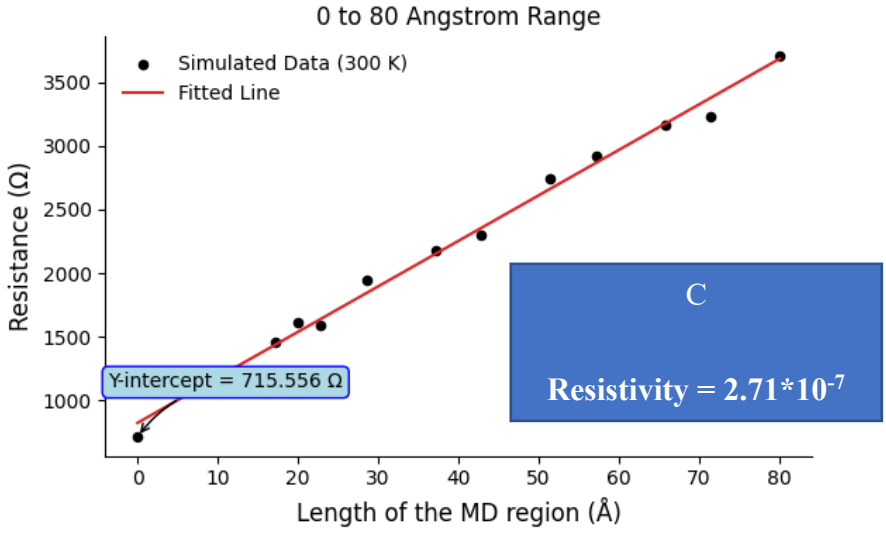
0 to 80 Angstrom Range
Simulated Data (300 K)
Fitted Line
Resistance (Ω)
Length of the MD region (Å)
Y-intercept = 715.556 Ω
C
Resistivity = 2.71*10-7